UNIVERSITY OF OKLAHOMA

GRADUATE COLLEGE

COMPREHENSIVE RESERVOIR CHARACTERIZATION OF THE WOODFORD SHALE IN PARTS OF GARFIELD AND KINGFISHER COUNTIES, OKLAHOMA

A THESIS

SUBMITTED TO THE GRADUATE FACULTY

in partial fulfillment of the requirements for the

Degree of

MASTER OF SCIENCE

By

JING ZHANG
Norman, Oklahoma
2016

COMPREHENSIVE RESERVOIR CHARACTERIZATION OF THE WOODFORD SHALE IN PARTS OF GARFIELD AND KINGFISHER COUNTIES, OKLAHOMA

A THESIS APPROVED FOR THE
CONOCOPHILLIPS SCHOOL OF GEOLOGY AND GEOPHYSICS

BY

_____
Dr. Roger Slatt, Chair

_____
Mr. Richard Andrews

_____
Dr. Matthew Pranter

Dedicate to my dear mom and dad who gave me countless love and support.

Acknowledgements

I would like to appreciate all the people who supported me and helped with my thesis, study and life at OU; this section only can express a corner of my appreciation to all of them.

First and foremost, I would like to thank my advisor Dr. Slatt; he gave me the chance to study in OU and during these past two years I made a lot of progress under his guidance and support. Without him, this thesis could not have been done. I deeply appreciate his care and help!

I would also like to express my special thanks to my committee members, Mr. Andrews and Dr. Pranter, for helping me with my study and research so that I can make fast progress. Mr. Andrews always cared about my study and gave me lots of feedback during the research progress. Dr. Pranter always gave me many ideas and techniques necessary in reservoir modeling.

I feel grateful that during the two years I was surrounded by many friends and colleagues; we learned from each other and took care of each other and shared life with each other. I really appreciate my friends in the IRC and geology department, and professors at OU. You all are important to me and make my life beautiful!

Table of Contents

List of Tables

List of Figures

Abstract

This research is a comprehensive characterization of the Woodford Shale within an area of six townships and ranges located at the boundary of Garfield and Kingfisher Counties in Oklahoma.

The methods of the Woodford Shale reservoir characterization include: sequence stratigraphy interpretation, well log interpretation, X-ray diffraction (XRD) and X-ray fluorescence (XRF) analysis on drill cuttings, Rock-Eval organic geochemistry analysis and microseismic interpretation.

The interpretation results of these methods provided detailed characteristics of the Woodford Shale. Seven third order parasequences were identified within the Woodford based on the well logs. The lower parasequences were more likely to be deposited where there was a paleo-topographic low, and there is an inverse relationship of thickness between the Woodford and Sylvan Shale. The mineral composition obtained from drill cuttings shows that the Woodford Shale has high clay content mainly composed of illite and kaolinite, moderate quartz content derived both from biogenic radiolaria and detrital quartz. The percentage of quartz highly affects the brittleness of the formation and ultimately affects the efficiency of hydraulic fracturing. From the thin section analyses, there are five types of Woodford Shale cuttings identified based on different mineral composition and internal structure. The chemostratigraphic analysis based on the horizontal well XRF profile defined 12 chemofacies. The 12 chemofacies were interpreted and related to sequence stratigraphy and sea level fluctuations. The XRF datasets are also correlated with XRD-derived mineral data and calculated brittleness. The organic geochemistry aspect indicated that

Woodford is an organic-rich shale with high TOC value and it is within the oil thermal maturation window due to the shallower burial depth than the Woodford in the Anadarko Basin.

The microseismic data interpretation of one horizontal well indicates that there is a relationship between the sequence stratigraphic framework and the microseismic event distribution. In the highstand system tract (brittle zone), the fractures are more prone to stay within the target formation and grow horizontally to enhance the fracturing efficiency. When the stimulation occurs within the transgressive system tract (ductile zone), the perforation energy will be absorbed by the formation and reduce the fracturing efficiency. From the image log and microseismic distribution patterns, the local stress field was interpreted. The maximum horizontal stress direction is N80E. To get better fracturing effect in the future, nearby well is should be drilled perpendicular to the maximum horizontal stress direction, or N10W.

Overall, the Woodford Shale in the study area is a high potential and high quality unconventional reservoir for exploration and development. The well placement and fracturing plan design need to consider the sequence stratigraphy and heterogeneity within the reservoir in order to enhance drilling efficiency and hydrocarbon production.

Chapter 1: Introduction

The Woodford Shale, an unconventional shale reservoir distributed in Oklahoma, Texas, New Mexico and Arkansas, is one of the main contributors of oil and gas resource in the United States (Comer, 1991; Comer, 1992). The Woodford Formation was introduced by Taff (1902) who defined the Woodford as the chert and black shale from the Arbuckle Mountain anticline.

The extensive exploration and development targeting the Woodford Shale in Oklahoma began in 2005; the initial production was focused on the southern Oklahoma, Arkoma Basin, and then moved to the Anadarko Basin. In recent years more and more activities have been located in the Ardmore Basin and Nemaha Uplift area (Figure 1.1).

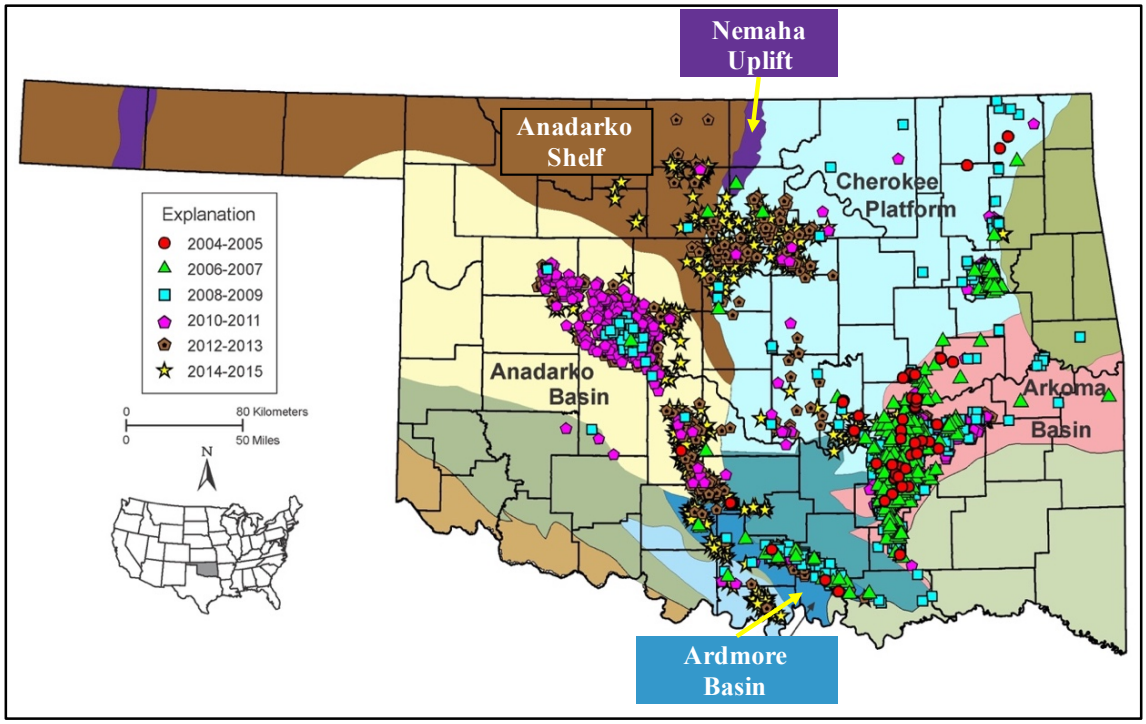

Figure 1.1: Drilling activity targeting the Woodford Shale in Oklahoma since 2004 (Modified from Oklahoma Geological Survey, 2016)

There have been many students at the OU's Institute of Reservoir Characterization and Oklahoma Geological Survey, aimed at gaining a better

understanding of the Woodford Shale as an unconventional resource shale. Sequence stratigraphy related studies include Amorocho (2012), Chain (2012), Kilian (2012), Molinares (2013), McCullough (2014) Bontempi (2015). Lithofacies and geological characterization of the Woodford Shale was done by Bernal (2013), Ali (2015) and Hasbrook (2015). Fracture and rock mechanics research were carried out by Portas (2009) and Badra (2011). Inorganic geochemistry characters were studied by Treanton (2014) and Turner (2016). Seismic interpretation and inversion research were conducted by Cardona (2014) and Infante (2015). Slatt and O'Brien (2011), Hasbrook (2015) illustrated the common pore types in the Woodford and Barnett shales and their contributions to the gas migration and storage.

Recent drilling targets of the Woodford Shale reservoir are gradually switching toward the Anadarko Shelf area, but little research has been done specially on the Woodford Shale in the northern part of Oklahoma. It is necessary to conduct comprehensive reservoir characterization research on the Woodford Shale in order to evaluate the resource potential of that area for future development activity.

1.1. Objectives and Motivation

The primary objective of this thesis study is to use comprehensive methods of unconventional reservoir characterization to estimate the reservoir potential of the Woodford Shale in the Garfield and Kingfisher counties in Oklahoma. The thesis study aims to incorporate the techniques that focus on different aspects of shale reservoirs such as organic geochemistry, inorganic geochemistry, sequence stratigraphy, brittleness evaluation and natural fracture network, and then to correlate the interpretation results for a better assessment of the Woodford Shale reservoir potential.

The motivation of this study is to have an understanding of the Woodford Shale on the west side of the Nemaha Uplift. Since there is a difference in the production data from the east side to the west side of the Nemaha Uplift: higher production from the Woodford on the east side of the Nemaha Uplift than the west side. This differences can be caused by reservoir heterogeneity, different source rock potential, different source of oil, and well design scenario. Analyzing the reservoir characteristics can provide clues to the possible cause of differential production from each side and provide beneficial information for the future development.

The Woodford Shale within the Anadarko Shelf area has shallower burial depth of around 6,000 ft subsea, which makes it easier for drilling and production than the Woodford Shale in the Anadarko Basin. Oil production from the Woodford Shale is dominated due to lower thermal maturity which occurs within the formation at shallower depth. Thus, high-quality reservoir characterization and modeling of the Woodford Shale can not only help reconstruct the paleo-depositional environment, but also provide an efficient indicator for exploration and development activity.

1.2. Study Area

The study area of this thesis is located in the Garfield and Kingfisher Counties in northern Oklahoma. It covers six townships and ranges from 21N 6W at the northwest corner to 19N5W at the southeast corner. The study area is located on the west side of Nemaha Ridge and close to the Nemaha fault zone (Figure 1.2).

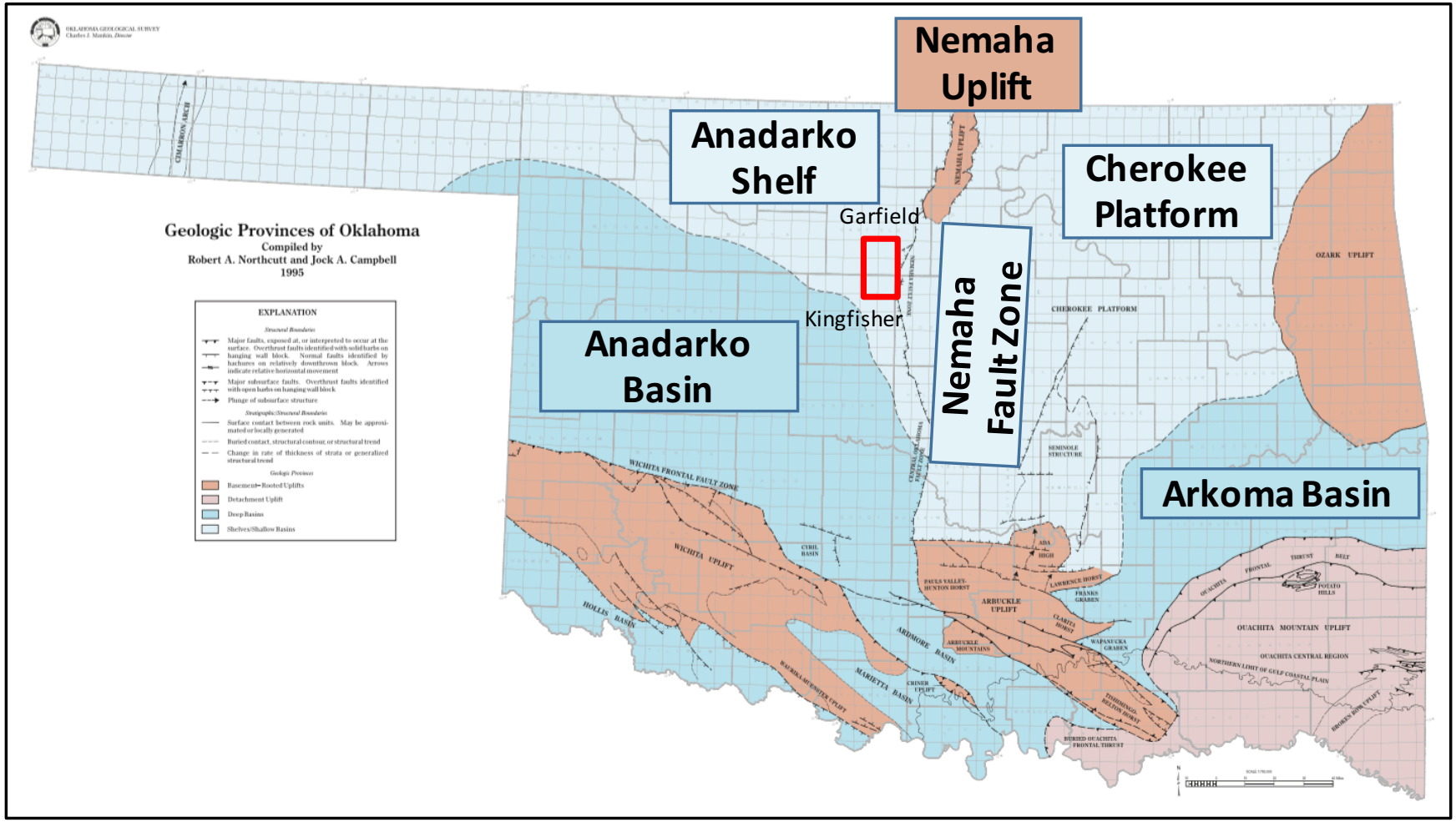

Figure 1.2: Geologic province map of Oklahoma. The study area is highlighted with red rectangle (Modified from Northcutt and Campbell, 1995).

1.3. Regional Geological Background

The Woodford Shale deposition began during the late Devonian, when there was a global marine transgression. The paleo-shoreline migrated onto the craton, then the Woodford Shale was deposited in the expanding epeiric sea until the early Mississippian (Comer, 1991) (Figure 1.3). During the Devonian depositional period, the state of Oklahoma was located at around 20°S and 10°S in early Mississippian time due to the southward migration of the paleo-equator (Blakey, 2012).

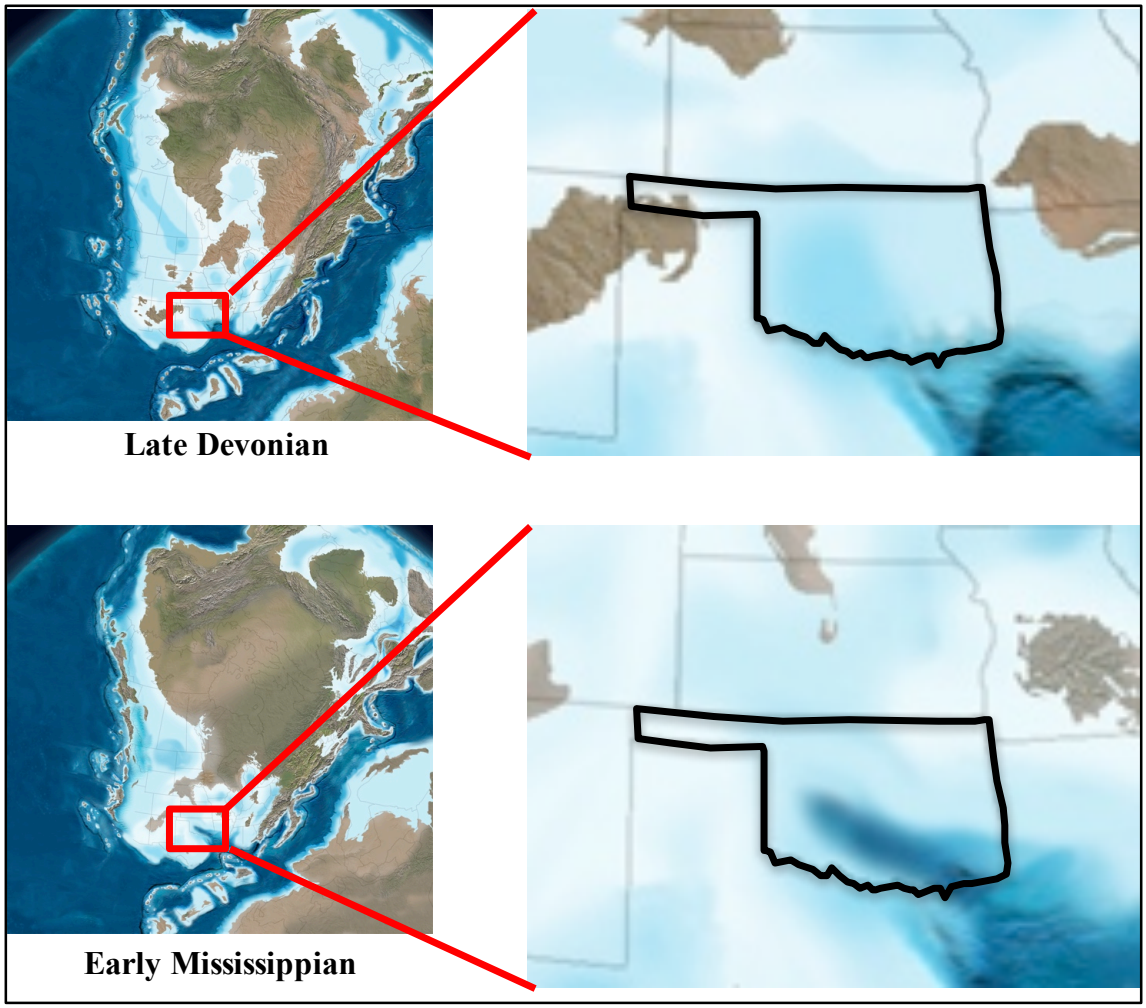

Figure 1.3: Paleogeography of North America in Late Devonian time and Early Mississippian age, and the location of current day Oklahoma on paleo-North America continent (Modified from Blakey, 2012).

The stratigraphic column is illustrated in figure 1.4. As shown in the column the Woodford Shale was deposited on an unconformable surface at the base of the formation, named “pre-Woodford unconformity”. This unconformity is interpreted as an erosional surface due to the pre-Woodford lowstand erosion sequence boundary and the transgressive surface of erosion at the beginning stage of rising sea level. It eroded parts of the underlying Hunton Group limestone in most areas of Oklahoma. A contrary thickness relationship between the Woodford Shale and its underlying formation exists due to the subaerial exposed weathering (Amsden, 1975, 1980; Al-Shaieb et al, 2000; McCullough, 2014). In the north-central and northeastern parts of Oklahoma, the entire Hunton Group has been entirely removed by erosion. Thus the Woodford directly overlies the Sylvan Shale in this area (Amsden, 1975). In some areas, especially the northern part of Oklahoma, there is a very thin sandy formation named the Misener Sandstone at the base of the Woodford Shale Formation. It is interpreted as a lag sand deposit at the beginning stage of sea level rise or late stage sea level fall and turnaround (Kuykendall and Fritz, 1993). The Misener Sandstone deposit is discontinuous due to the paleotopography thus has a channel-like distribution pattern (Kuykendall and Fritz, 1993).

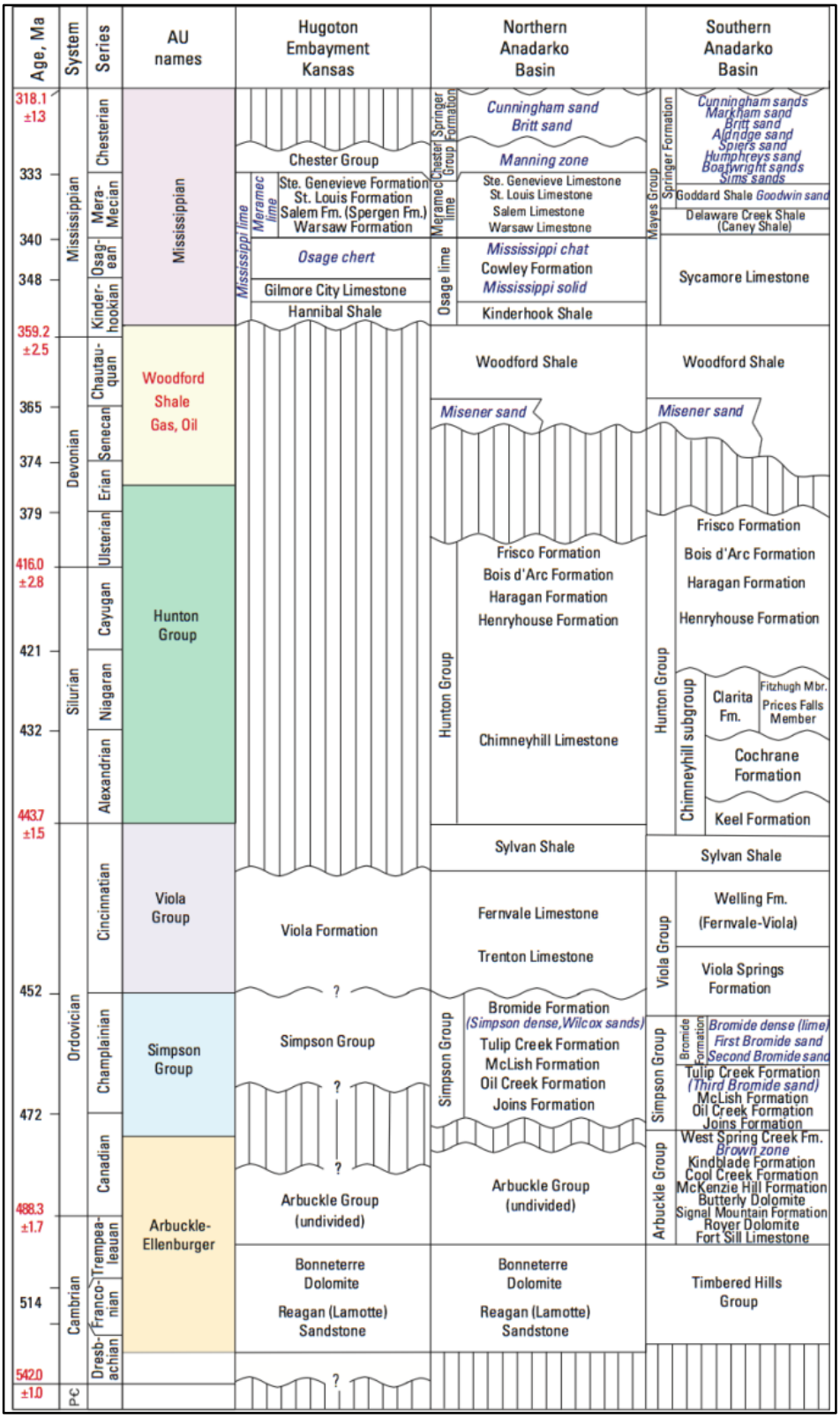

Figure 1.4: Stratigraphic column of the Woodford Shale in Anadarko Basin area

Within the Woodford Shale there is a second order sequence that starts with a transgression, which reaches a maximum flooding surface with high gamma ray reading from a high TOC (Total Organic Carbon) content. Above the maximum flooding surface there is a regressive deposit characterized by decrease in gamma ray.

The Woodford is often subdivided into three members (figure 1.5): upper, middle and lower Woodford (Althoff, 2012; Amorocho, 2012; Slatt, et al., 2012; Treanton, 2014). The lower Woodford, has a dominant clay rich facies with high TOC accumulated at the base of the Woodford as interpreted from seismic inversion (Infante, 2015). It is a black shale deposit close to the shore during transgression. The middle Woodford has the highest TOC content, very high radioactivity, and with higher clay content. The upper Woodford starts with a regional regression with higher chert content and phosphate nodules as an identifier of the upper Woodford (Hester et al., 1988).

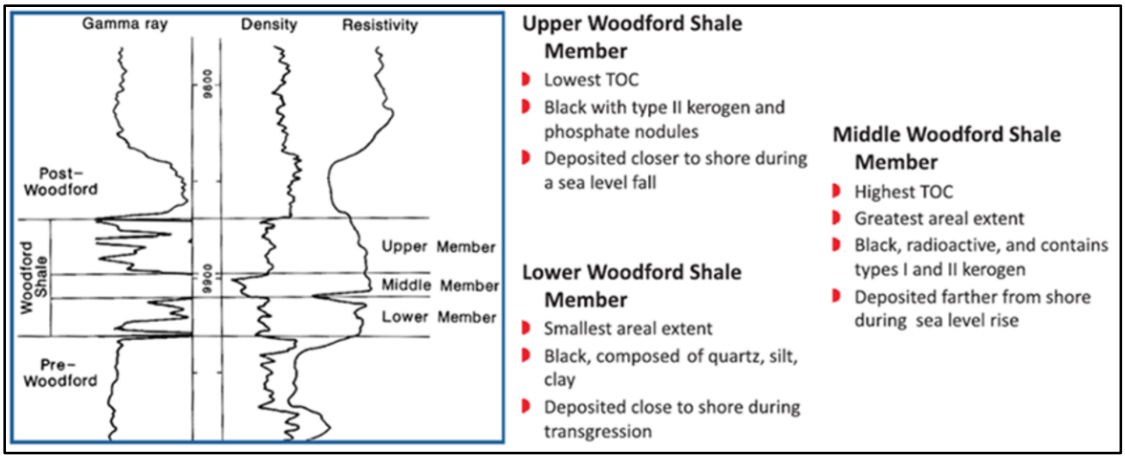

Figure 1.5: Three members of the Woodford Shale and characteristics of each member (Modified from Hester et al., 1988).

1.4. Local Geological Background

In the study area, most of the Hunton Group is eroded, particularly at the southwest corner. Thus, the Woodford Shale directly overlies the formation below such

as the Sylvan Shale Formation, Viola Formation or sometimes the Misener Sandstone is different due to the different areal erosion and paleotopography (Figure 1.6).

Since the study area is located in the northern part of Oklahoma and according to the figure 1.2, it was further from the center of the transgression trend in south central Oklahoma in early Mississippian time. This led to shallower water depth and more subaerial exposure then ultimately resulted in pre-Woodford erosion all the way down to the Viola Limestone formation.

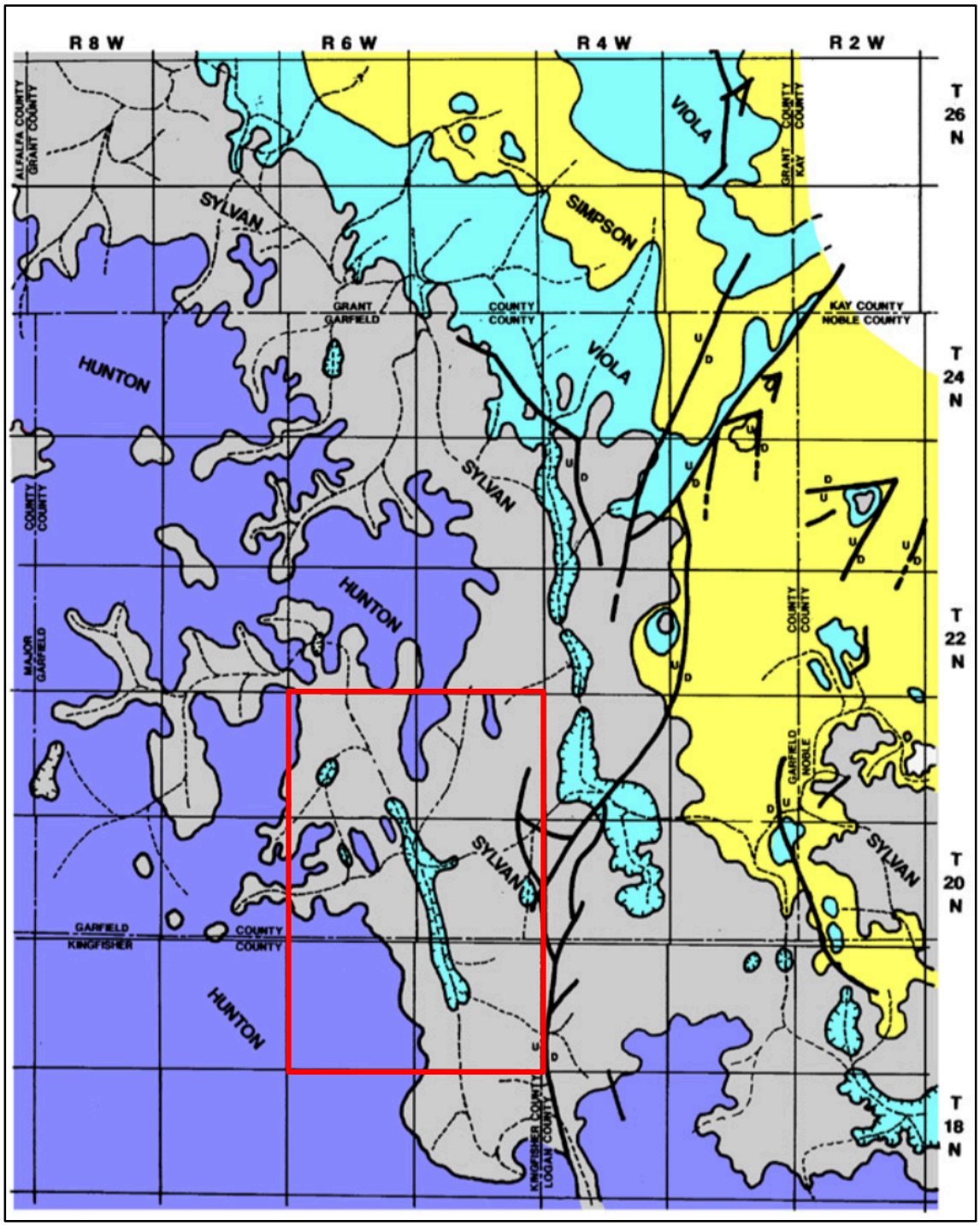

Figure 1.6: Pre-Woodford formation distribution in the Garfield and Kingfisher counties with the Nemaha faults. The study area is highlighted with red rectangle (Modified from Kuykendall and Fritz 2001).

Chapter 2: Data Set and Methods

2.1. Data Available

The data for this thesis research was generously provided by Longfellow Energy, LP. Here we want to show our deep appreciation to Longfellow's consistent support. For confidential purposes, all the wells are renamed.

The dataset includes 125 wells located within the study area, 38 wells are in Kingfisher County and 87 wells are in Garfield County. Thirteen wells are operated by Longfellow energy, and 9 of them are horizontal wells targeting the Woodford Shale. The rest of the wells are all vertical wells. Vertical wells not drilled by Longfellow have conventional well logs such as gamma ray log, resistivity log, density and neutron porosity and bulk density. Also some of the wells have sonic and PE (Photo Electric Effect) logs. Two wells have image logs. All the Longfellow wells have mud log data and cutting samples available. There is also one horizontal well with microseismic location data in 12 stimulation stages. Figure 2.1 shows the well distribution in the study area; Longfellow wells are highlighted with stars and the Nemaha Faults are in black bold solid line.

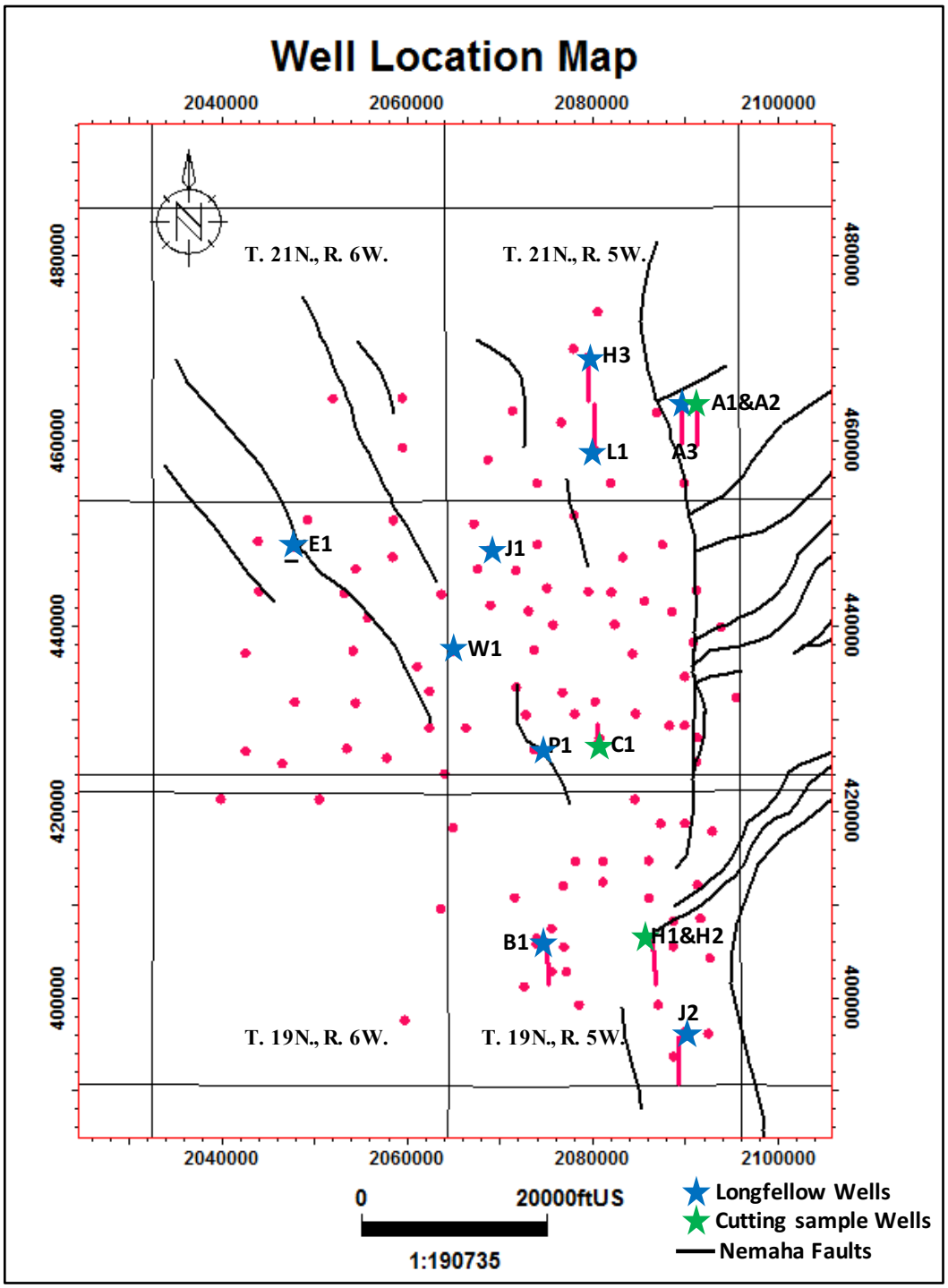

Figure 2.1: Well location in the study area, the red dots are well with regular well logs and stars represent the Longfellow wells.

Beyond the well log data, 21 cutting samples from different depths in one horizontal well (H2 well) were used to make the thin sections, Rock-Eval analysis, and XRD (X-Ray Diffraction) examinations. Thin section pictures, Rock-Eval reports, and

XRD results were provided by Longfellow Energy. We also made 11 more thin sections of cuttings from three different wells: A1, A2, C1 (Table 2.1) at selected depths within the Woodford Shale. Nine cutting samples were analyzed by XRD from selected depths in A1, A2, C1 wells; 16 Rock-Eval analyze were conducted on A1, A2, C1 and H2 wells. Since the cutting samples were provided, we also measured the XRF (X-Ray Fluorescence) data for H1, H2, A1, A2, C1 and E1 wells. Summary of the available sample data is shown in Table 2.1. Many of the data measured by ourselves are at the same depth, due to limited sample amount, not all the tests can be done for the same sample depth. The A1 well is a pilot hole with 30 feet sampling interval, thus there are only three bags of samples containing the Woodford Shale. The A2 well is a 30 feet sampling interval horizontal well and the Woodford top is at 7130 feet measured depth. The well starts to landing within the formation after hitting the formation top, thus the samples after the formation top have a smaller vertical interval due to the tilted well track and the chosen samples end when the well is horizontally landed in the formation. The C1 well is a sub-vertical well with 30 feet sampling interval, and there are four bags of cutting samples through the Woodford Shale. The H2 well is a horizontal well, since many depths already provided with the XRD and Rock-Eval data, the samples chosen additionally by the author are based on the XRF profile.

Well Name	H1	H2	A1	A2	C1	E1
XRD	0	22	3	3	3	0
XRF	23	147	14	70	15	126
Rock-Eval	0	24	3	6	4	0
Thin Section	0	21	3	4	4	0
Microseismic	0	1	0	0	0	0

Table 2.1: Available data summary for six wells. All samples are located within the Woodford Shale.

2.2. Methods of Study

The method of this research mainly follows the flowchart proposed by Slatt et al., (2012) for pore to regional scale integrated characterization of unconventional shales. The workflow is revised based on data availability for this research mainly focused on the subsurface method of characterizing the shale reservoir. The primary goal of the research is to integrate results from different methods to obtain a comprehensive characterization of the Woodford Shale in this area. The tools and concepts utilized include sequence stratigraphic interpretation, XRD mineral component analysis (cutting samples), thin section analysis (cutting samples), XRF element component analysis (cutting samples), Rock-Eval organic matter percentage and type and microseismic interpretation. The overall interpretation provides the evaluation of reservoir potential and future well placement suggestions.

Subsurface mapping is widely used for the shale reservoir to construct a sequence stratigraphic framework. For subsurface mapping, sequence stratigraphy interpretation from logs to cross sections then to the basin range reveals the details of depositional trends and sequences. (Slatt, 2013; Cardona, 2014; McCullough, 2014; and Infante, 2015) used to describe the sequence stratigraphy of the Woodford Shale in Oklahoma and map the Woodford Shale and its sequence set within the formation. For this thesis research, the typical upper, middle and lower sections division is replaced by parasequences just like Slatt (2013) and Cardona (2014) did. The correlations are mainly based on the gamma ray, resistivity, neutron porosity, density porosity and PE logs.

XRF (X-Ray Fluorescence) is an efficient tool to understand the element composition of a shale at a millimeter scale. The instrument used in this research is the Bruker Tracer IV-SD^{TM} series handheld X-ray fluorescence spectrometer (Figure 2.2). Turner et al., (2015) has used the XRF data to characterize the Woodford Shale and correlating stratigraphic surfaces using outcrop samples.

The cutting sample to be analyzed is enclosed in a plastic cup with plastic wrap. Each cup contains the equal amount of cutting sample with about 1cm thickness. Major and trace elements are scanned under different settings of voltage, current, and time. The major elements scanning setting is under 15 kV, 35 mA for 90 seconds with the vacuum on. The trace elements scanning setting is under 40 kV, 17.1 mA for 60 seconds without the vacuum condition. After scanning, the raw data is calibrated to ppm level and combines major and trace elements together as a complete element profile for each sample. To interpret the XRF data, chemofacies are defined using a cluster analysis method. Each chemofacies represents a different depositional environment. Element data are also correlated with mineral data derived from XRD measurement using linear regression for brittleness calculation.

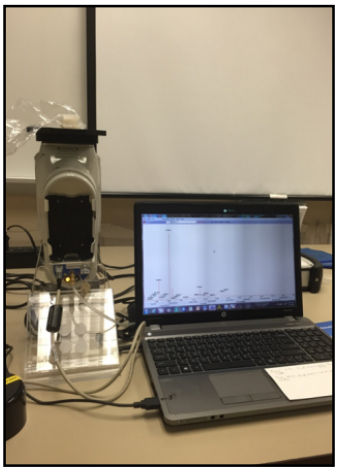

Figure 2.2: Hand Held Bruker Tracer IV-SD^{TM} scanning the cutting samples. The computer screen shows an instant spectrogram of the cutting sample.

The mineral analysis is conducted in two ways, XRD (X-Ray Diffraction) analysis and thin section observation. Powder XRD analysis provides the mineral composition of each sample; the cutting mineral composition is utilized to estimate the brittleness at the sampling depth. The measurements were made using a Rigaku PDXL Powder X-ray Diffractometer. The selected samples weighed 1 gram each. The samples were crushed, then ground and milled into extremely fine grain size (<5 microns). Then the samples were treated with ethylene glycol and heated to 500°C overnight. Dried samples were flattened and set up for scanning. The data is analyzed by using Materials Data (MDI) Jade 2010 software. Cuttings of thin sections were made from epoxy encapsulated cutting cubes (Figure 2.3). Thin sections were analyzed under the optical microscope.

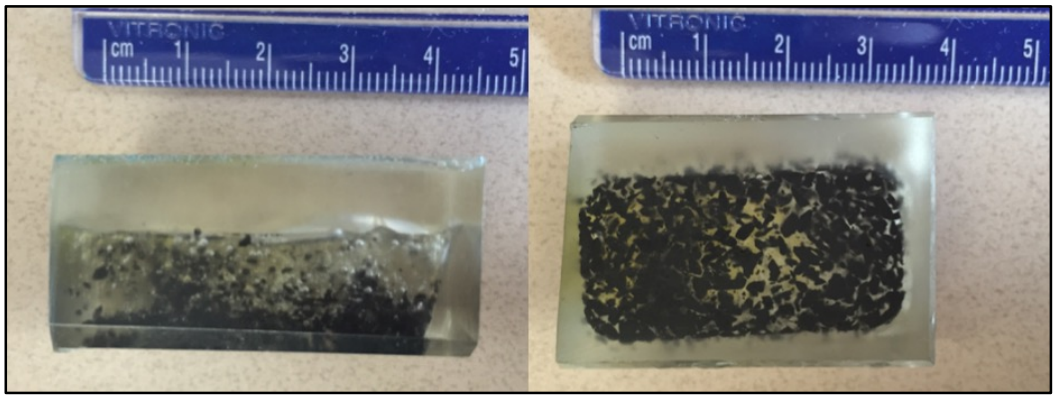

Figure 2.3: An epoxy cube of cutting sample ready for making the thin section. Side view on the left, top view on the right.

Organic geochemistry analysis was also conducted on 37 samples from four different wells, throughout the entire Woodford formation. The samples were analyzed by Geomark Research. Pyrograms were generated and analyzed to estimate the resource potential and relationship with the XRF data.

Since only the data of the final processed microseismic location was provided by Longfellow Energy, processing raw data to obtain the event location procedure was not

necessary. This thesis mainly focuses on studying the microseismic distribution pattern within the sequence stratigraphic framework and evaluating the fracturing job efficiency using sequence stratigraphy.

Reservoir modeling is the final procedure to evaluate the reservoir potential from the well scale to the reservoir scale. This thesis used the Petrel^{TM} software to model the TOC and chemofacies within the reservoir. A Sequence stratigraphic framework was constructed ahead of modeling to separate the reservoir into different zones that represent highstand and transgressive system tracts. Vertical and horizontal variograms of upscaled well properties such as chemofacies, elemental data and microseismic events were constructed for the sequential Gaussian simulation to model the desired property.

Chapter 3: Sequence Stratigraphy Interpretation

3.1. Regional Formation Mapping

The Woodford Shale sequence stratigraphy was briefly introduced in Chapter 1. The Woodford Shale in the study area was mainly deposited directly over the Sylvan Shale and Viola Limestone. Mapping the formations mainly relies on well logs correlation and interpretation. The well log characteristics of each formation are discussed below.

The Mississippian Limestone group is a thick limestone section interbedded with sand and shale (Clair, 1948; Beebe., 1959; Northcutt, et al., 1999). The average thickness of the Mississippian Lime in the study area is about 500 feet. The characteristics of this formation are low gamma ray (30 API) for pure limestone and 70 API for sandy or shaly limestone; high deep resistivity (100-200 OHMM) and PE log from 4 to 5. Density porosity and neutron porosity are as low as 3 to 6 porosity units and stacked together as typical reaction of limestone. The contact between the Woodford Shale and Mississippian Lime is easy to identify from the gamma ray log: a jump in gamma ray from less than 50 to more than 150 API, neutron porosity dramatically increases to 15-20 porosity units and resistivity drops to 40 OHMM. The top of the Woodford is considered a conformable contact where there is a 6 to 10 foot transition zone (Fritz and Gerken, 2001), otherwise as an unconformity (Bontempi, 2015).

The Woodford Shale is about 100 to 150 feet thick in the study area, the gamma ray reading is above 150 API and can be as high as 600 API. The resistivity log reading ranges from 50-150 with an average value of 90 OHMM. High resistivity is mainly

contributed by oil and organic matter in the formation (Kirkland, et al., 1992; Johnson and Cardott, 1992; McCullough, 2014). The PE log reading is about 3 for shale. The neutron and density porosity curve are separated and in most cases neutron porosity is 12 porosity units higher than the density porosity. The separation is smaller in some portions of the Woodford, which represents the quartz content increasing in the Woodford Shale (Andrews, 2014). For the Woodford Shale, the quartz percentage directly affects the formation brittleness. Porosity separation is an easier and effective method to conduct brittleness estimation. The cut off of the brittleness evaluation is demonstrated in Figure 3.1.

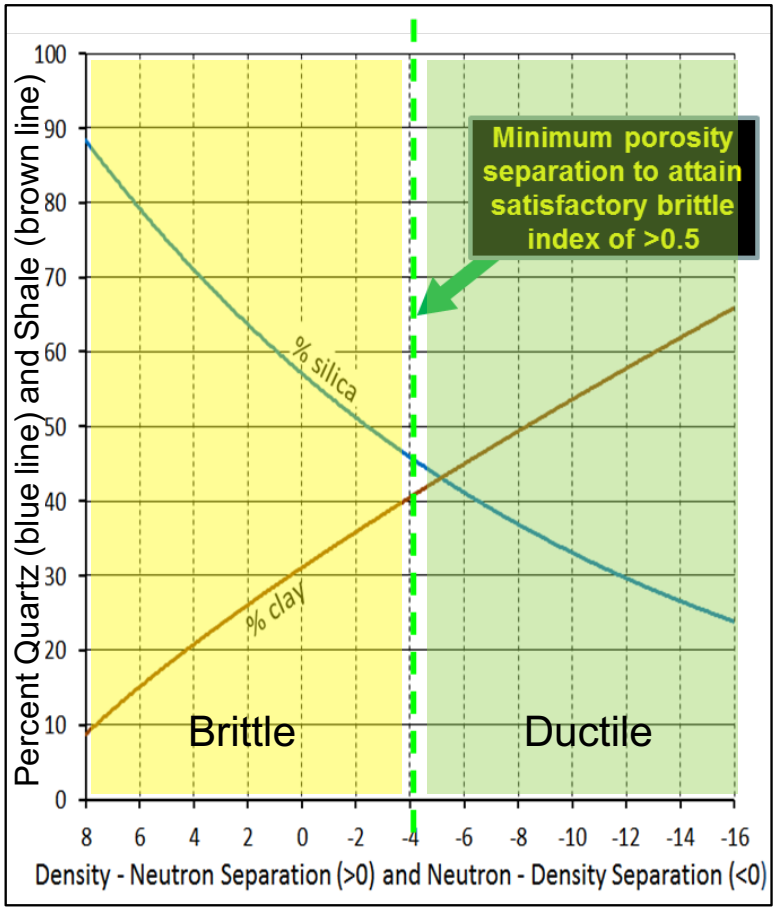

Figure 3.1: Density neutron porosity separation and silica clay percentage relationship of shale reservoir. When the density porosity and neutron porosity separation becomes larger than -4 porosity units, it will be considered as a brittle section (modified from Andrews, 2014).

The Misener Sandstone occurs locally beneath the Woodford Shale. It is difficult to distinguish from the Hunton Group and Viola Limestone with only the gamma ray log. The log character of the Misener sandstone are PE of 2, which is the typical reaction of sandstone. Deep resistivity values up to 200 OHMM and low gamma ray log reading of around 30 API. Crossover density porosity and neutron porosity is 3 to 6 porosity units. Misener sandstone is typically less than 20 feet thick in the study area. It was deposited as a channel sand at the beginning of transgression and distributed discontinuously in channel shape within the study area (Kuykendall and Fritz, 1993; 2001; Krumme, 2001; Newell et al., 2001).

The depositional process of the Misener sandstone is interpreted as a pre-transgressive lag of an incised valley shown in Figure 3.2. Before deposition the paleo topography had already developed a paleo-drainage fluvial system. At the beginning stage of sea level rise, the sand deposit was firstly settled as a channel fill. When the sea level continued to rise, fluvial systems were abandoned resulting in deposition of sediment that were fine-grained or clay-dominated. Texturally, this sequence has a fining-upward composition (Kuykendall and Fritz, 1993).

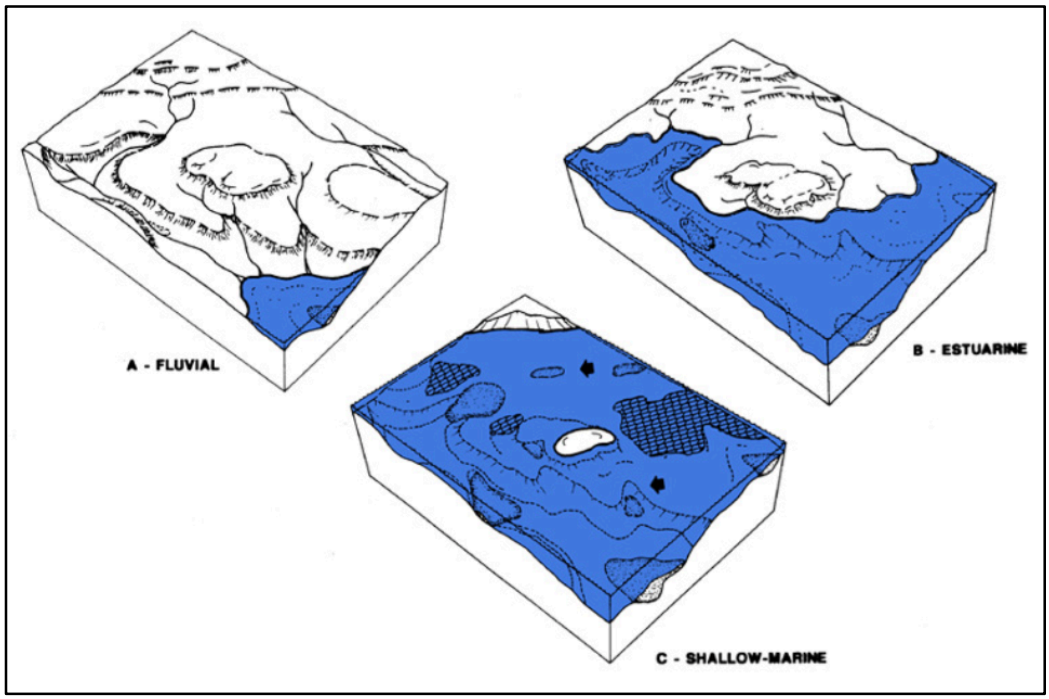

Figure 3.2: Misener deposition model. A: the pre-Misener channelized paleo-topography formed due to the sea level drop. B: As initial transgression progressed, the incised valley was filled with Misener Sandstone. C: Higher sea level formed the embayment for deposition of the Woodford Shale (Kuykendall and Fritz, 2001).

The Hunton Limestone only exists in the southwest corner of the study area. For a couple of the wells, the Hunton Limestone has a low gamma ray reading of about 20 API, high resistivity of about 200 OHMM and low neutron and density porosity (Amsden, 1975; Al-Shaieb et al., 2000). In the study area it is important to distinguish the limestone beneath the Woodford Shale as the Hunton group or Viola group due to the similar log response. If the well is located in the northeast part of the study area, there is little chance of it being the Hunton Group.

The Sylvan Shale formation is directly in contact with the Woodford Shale in most of the study area. The upper part typically has a lower gamma ray of 75 API, which gradually increases downward to 100 API. From the contact with the Woodford Shale, there is a drop in resistivity from 200 to 10 due to the organic lean character of the Sylvan Shale. The separation of neutron porosity and density porosity up to 28

porosity units means the Sylvan Shale has a high clay content (McCullough, 2014). Beneath the Sylvan Shale, the Viola group top is easy to identify by a low gamma ray (20 API), high resistivity (> 200 OHMM), and low density and neutron porosity.

Figure 3.3 shows a type log from the Athey S.H.1-27 well which is located in Sec.27, T. 20N., R. 5W. It contains most of the formations mentioned above.

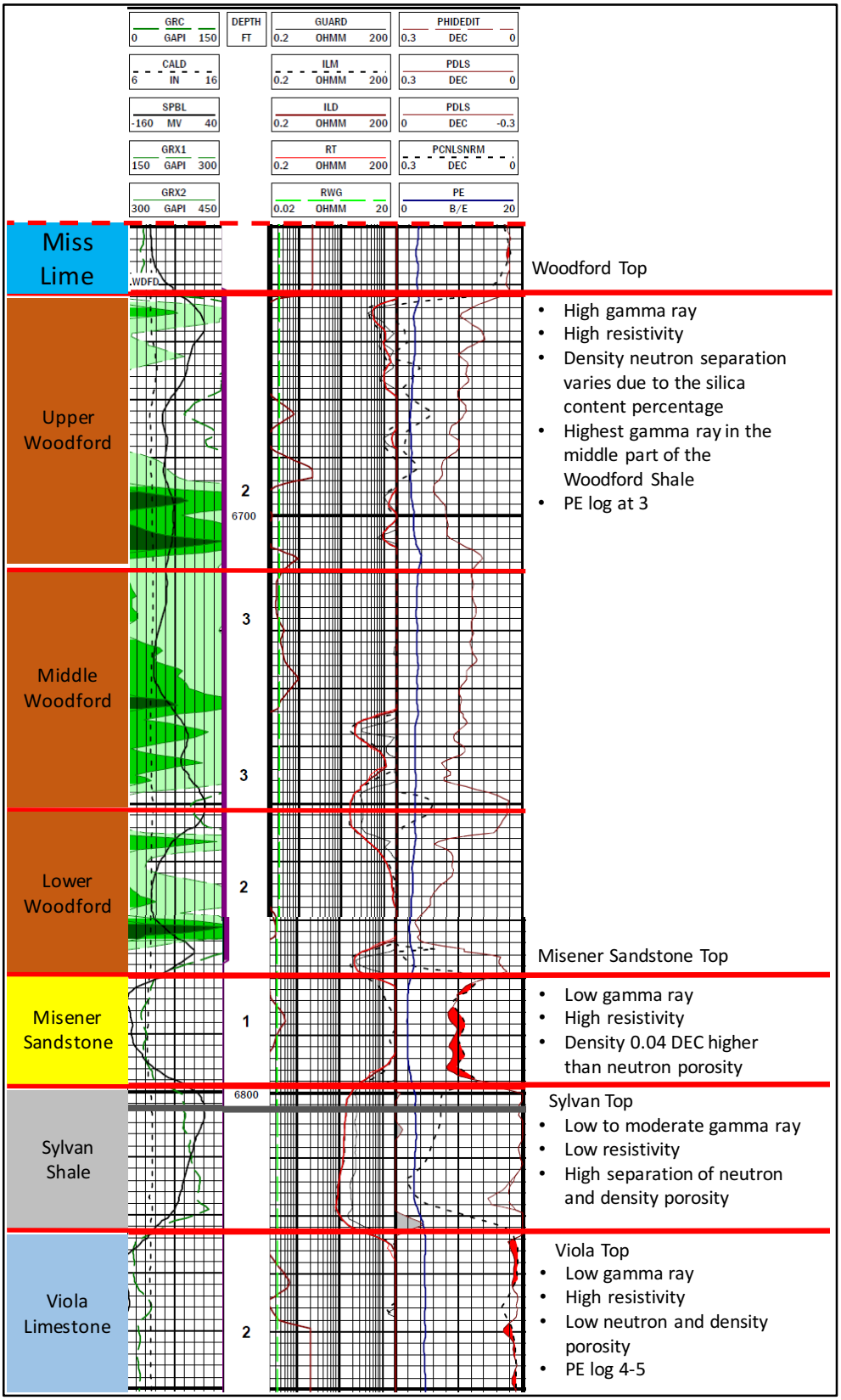

Figure 3.3: Type log characteristics of the Woodford Shale and neighboring formations.

After picking all the formation boundaries in Petrel™ from all the wells, the formation structure maps and isochore maps were made. Figure 3.4 shows the Woodford top and bottom structural maps. The Woodford Shale generally dips towards the southwest towards Anadarko Basin direction. There are two circular shape structures verified by seven well logs both from the top and base Woodford Shale structure maps. Since the circular structure area doesn't have the Hunton Group beneath the Woodford, there are not Hunton karst collapse features (Infante et al., 2016). From the cross section across these two sinkholes (Figure 3.11), there are several vertical faults which penetrate the cross section. Since seismic data is not available, accurate vertical displacement is hard to estimate only based on well logs. From the fault surface map there is a high possibility that the current day topographic low structures are induced by the vertical faults displacement.

Since the dip angle of the bedding is small, the isochore map is considered equal to an isopach map. The isochore map in this research was made by creating the isochore points from the well top picks and then making surfaces from the isochore points onto an isochore map. The lower surface structural map was made by adding the isochore map to the top surface structural map, which can effectively avoid surface crossover issues. Since the Hunton Group and Misener Sandstone formation are not spread throughout the study area. The Sylvan Shale Isochore map can be used for thickness comparison with the Woodford Shale (Figure 3.5).

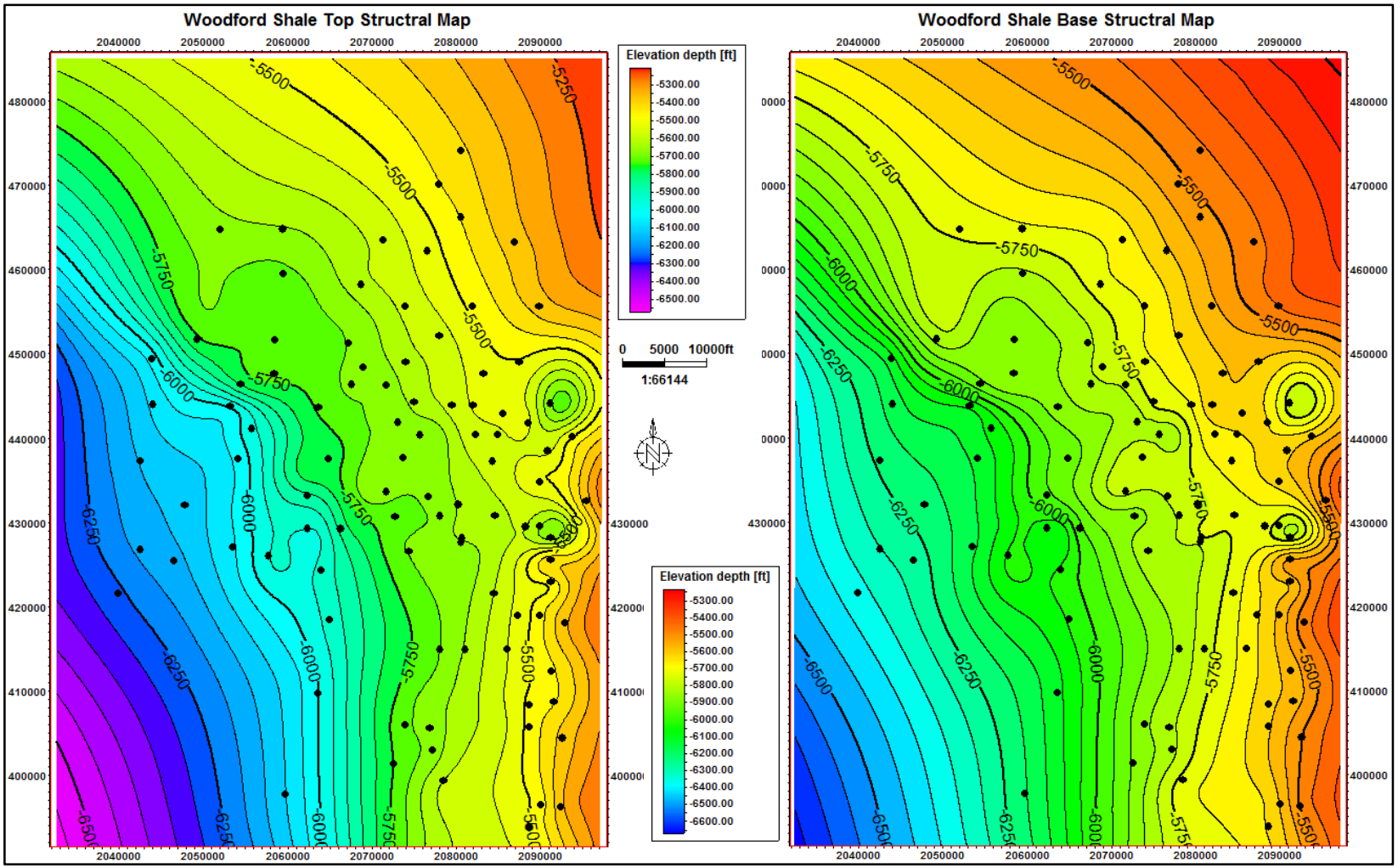

Figure 3.4: Woodford formation top and base structural maps. Both maps indicate that beds dip towards the southwest. Two circular structures occur on the north central part of the study area. The black spots are the well locations with Woodford formation top picks.

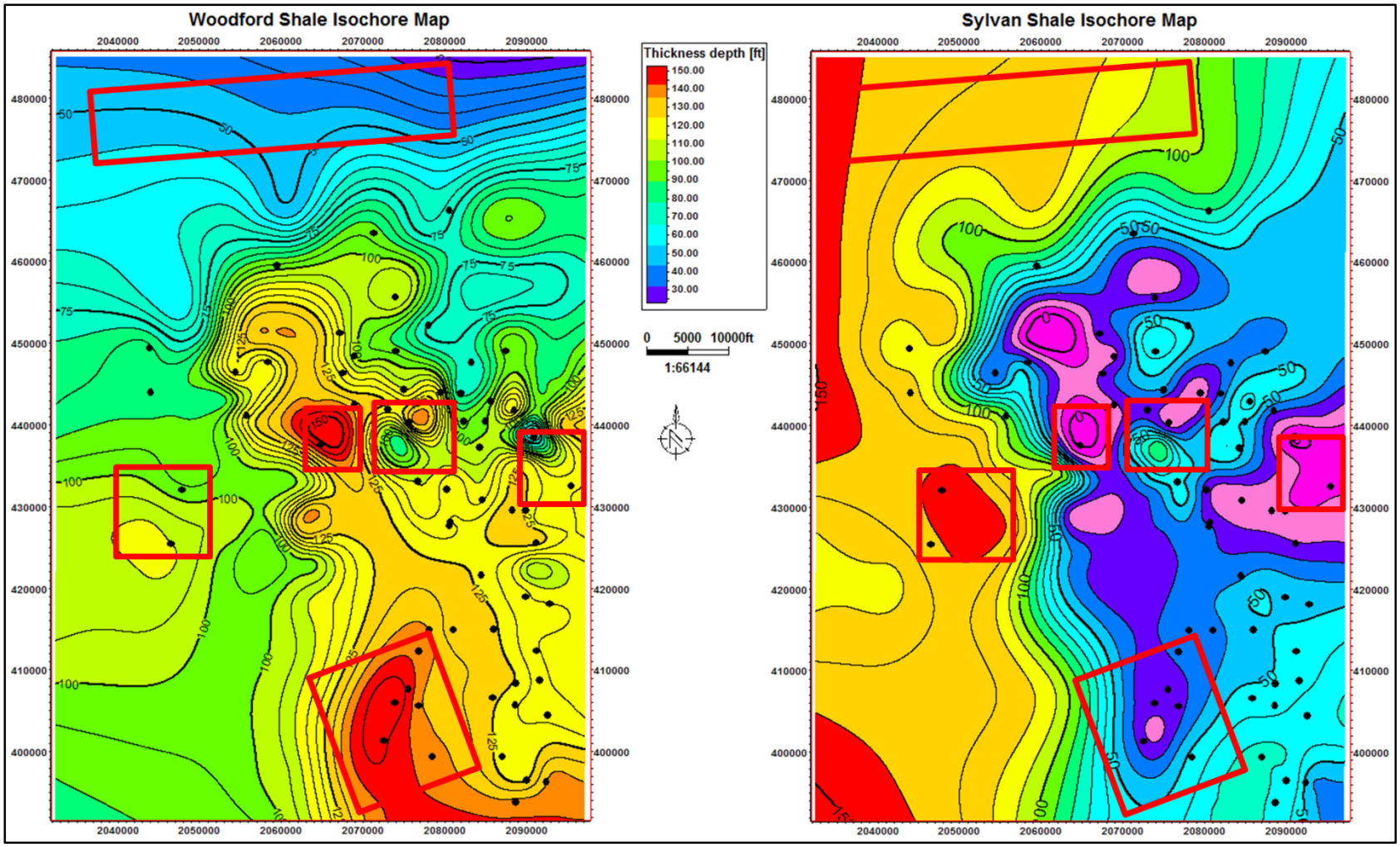

Figure 3.5: Isochore maps of The Woodford Shale (left) and Sylvan Shale (right) show the inverse thickness relationship between the two formations: where the Woodford is thick, the Sylvan is thin. The rectangules highlight the most obvious areas of thickness contrast. Black spots are the isochore points used for each map.

3.2. Interpretation of Intra-Woodford Parasequences

Within the Woodford Shale formation, there were fluctuations of periodic sea level reflected by the well logs, lithofacies and organic matter percentage. The sequence stratigraphic interpretation of this research is mainly based on the well logs. For shale reservoirs, when sea level is rising, there is an increase in fine grain sediment, biogenic quartz content, less large grain detrital input and carbonate content in the sediments. When the sea level drops, larger grain detrital input and carbonate gradually dominate and clay content decreases in the sediment. The change in this sediment component can be reflected on the well logs.

An upward increasing gamma ray, increasing density and neutron porosity separation indicates transgression. An upward decreasing gamma ray, decreasing density and neutron porosity separation indicates regression. A transgression-regression cycle forms a parasequence. For the Woodford, second order and third order parasequences are identifiable. Figure 3.6 shows the H1 well as a type log with sequence stratigraphic key surfaces identified. The entire Woodford Shale formation is subdivided into two second order parasequences, where there is the Frasnian/Famennian erosional surface in the upper middle Woodford marked by the red curved line (Comer, 1991; Over, 2002). Beyond the second order cycle, seven third order parasequences were identified based on the well logs. The 15 stratigraphic surfaces can be traced in most Woodford wells in the study area. Among the seven parasequences there is a main flooding surface for the entire Woodford Shale formation marked with a bold blue line. In Figure 3.6, the blue triangles represent regressive highstand systems tracts, and the

red triangles represent transgressive systems tracts. The parasequences are numbered from 1 to 7 from the bottom to the top.

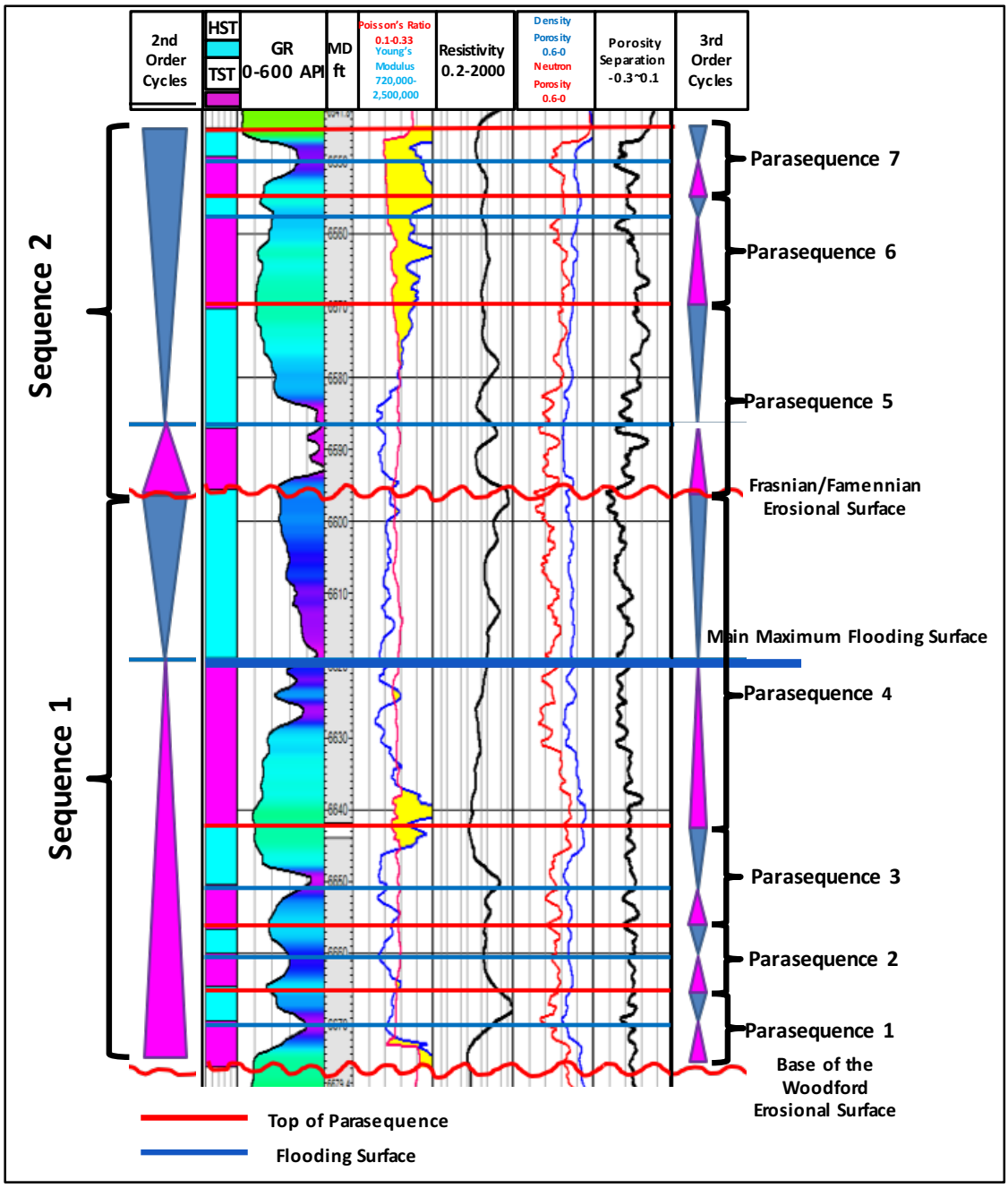

Figure 3.6: H1 well as the type log of Woodford internal parasequences identification. There are a total of seven parasequences identified from the well logs.

Four cross sections were made to correlate the sequence stratigraphic framework and characterize the Woodford internal depositional sequences, (Figure 3.7). A-A' is

oriented from west to east along the bed dip direction. B-B' is also oriented from west to east but southward of A-A'. C-C' is oriented from north to south, in the strike direction and depocenter from the isochore map. D-D' crosses two circular structures discussed earlier from north to south. White solid lines show the Nemaha Faults location within the study area

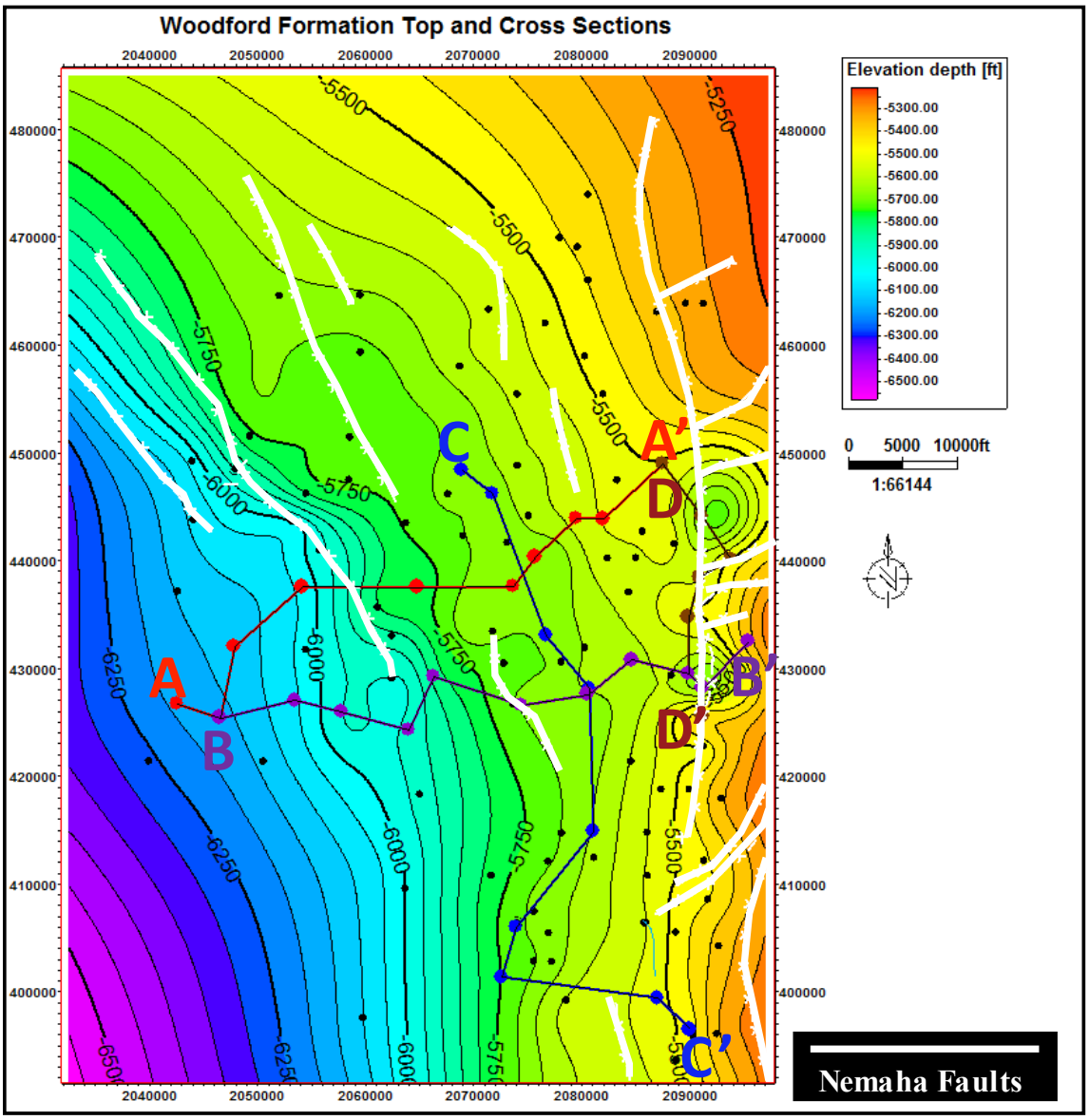

Figure 3.7: Four cross sections in the study area to correlate local sequence stratigraphic framework. The background map is the Woodford top structural map and white lines indicate the Nemaha Faults.

The main flooding surface in the lower middle part of the formation was used as the datum for the four cross sections (Fritz and Gerken, 2001). From the cross section A-A' (Figure 3.8), the Sylvan Shale generally gets thicker towards the west, the paleo structural low area, which means structurally higher areas were of shallower water and easier to be exposed and eroded. Thus the Sylvan Shale on the east side underwent more erosional activity than on the west side, resulting in the thickness variability. For the Woodford Shale, most of the upper parasequences can be correlated through the wells. The lower parasequences were not deposited over the paleo-structural highs. Due to the inverse thickness relationship between the Sylvan and Woodford, the complete Woodford Shale stratigraphic section mainly exists where the Sylvan Shale is thin. The thinning Sylvan Shale occurs under two circumstances. First, large scale structural high, as reflected by the structural map for the entire study area (Figure 3.4) where the northeast corner is a paleo structural high. This leads to more intense erosion of Sylvan Shale in that corner area and thins the Sylvan Shale formation before deposition of the Woodford. The second scenario is the small scale erosion activity such as channel incision, which can occur anywhere and causes local topographic lows for depositing the Woodford during early transgression. Both circumstances lead to complete parasequence deposition. From the fifth well from the left on cross section A-A', the Sylvan Shale was eroded by an incised valley and complete parasequences of the Woodford Shale were deposited. From the fault map overlay, there is a fault between the fourth and fifth well from the west, which doesn't have much impact on vertical displacement.

Cross section B-B' (Figure 3.9) shows the same Sylvan thickness trend as A-A', where the formation becomes thicker toward the structurally low area. Thin Hunton Group is mainly in the west. The Misener appears in the fifth well from the west, which represents the channelized sand deposit. The occurrence of Misener Sandstone is along the same strike direction with the thicker Woodford well on A-A', which confirms the topographic low area on A-A' is caused by channel-erosional activity. The complete Woodford parasequences can be found on the east. On the west where the pre-Woodford paleo-topography is high, which is also interpreted as fault elevated, there is no deposition of the lower parasequences.

Cross section C-C' (Figure 3.10) has more continuous correlation of the parasequences within the Woodford. There is one well on the north edge with channelized Misener Sandstone, the lower parasequences are missing for that well due to onlap on the pre-Woodford paleo topographic high.

The cross section D-D' (Figure 3.11) is of wells located close to the central part of each circular object. The central part of each circular structure is highlighted with a note. From Figure 3.7 the cross section D-D' is intersected with multiple Nemaha Faults especially where the two central circular structures are located; the structurally low feature is interpreted as vertical displacement of Nemaha Faults; the uplift of the Viola in the central part of the cross section is also interpreted as a horst induced by the Nemaha Faults.

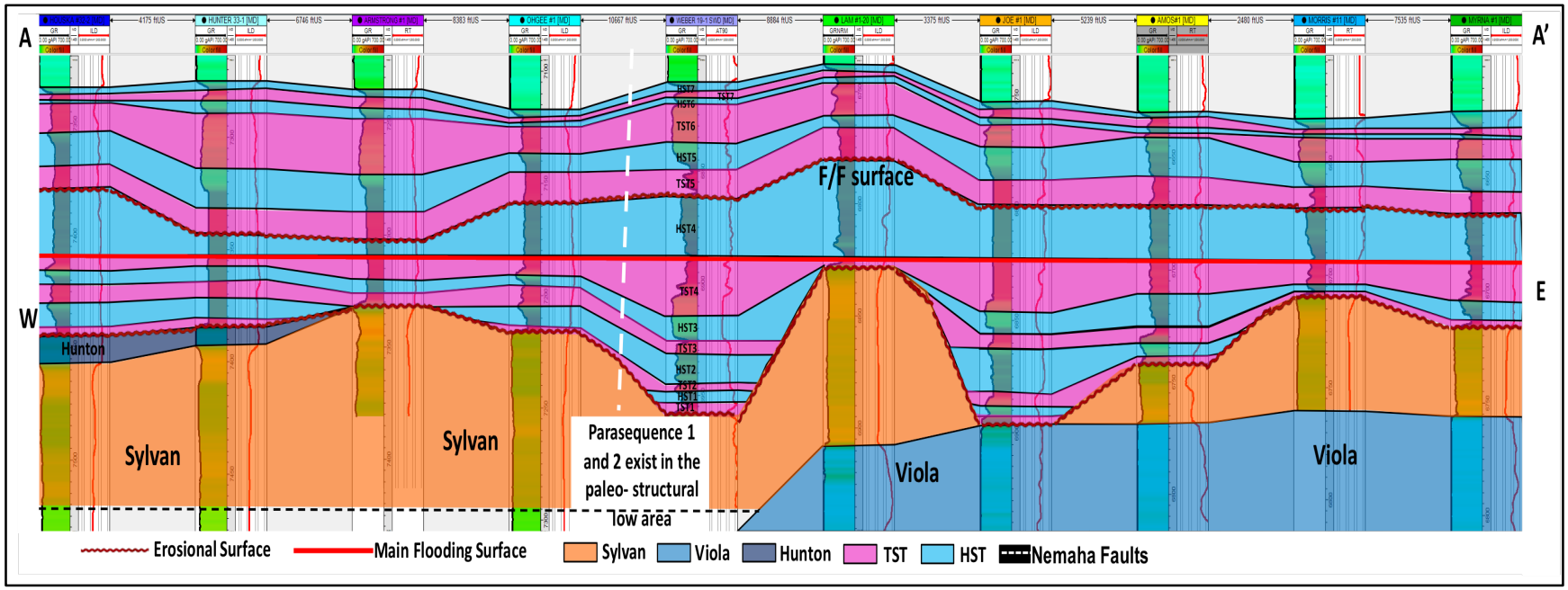

Figure 3.8: Cross section A-A' with parasequences correlation. Blue sections represent the highstand system tract, and pink section represents the transgressive system tract.

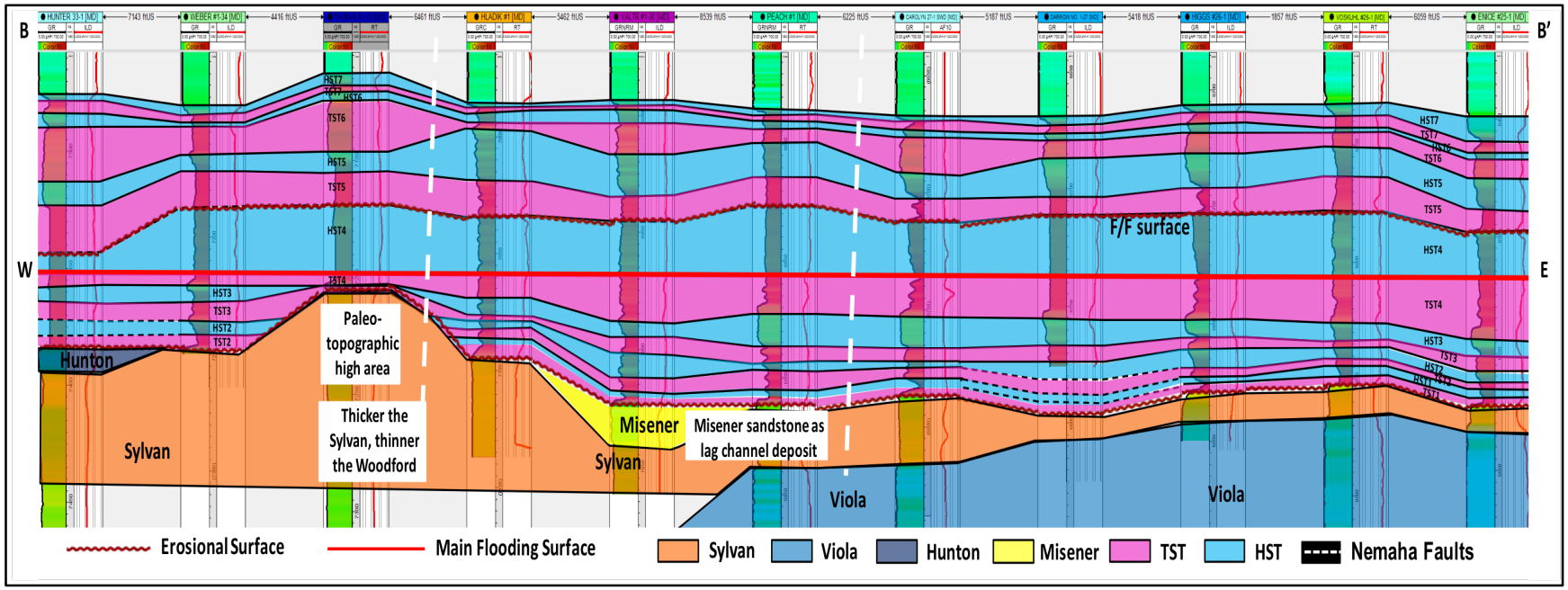

Figure 3.9: Cross section B-B' showing the Sylvan is thicker towards the west. Misener sandstone occurs is a lag deposit from early transgression. Lower parasequences are not deposited on the west side due to the paleo topographic high.

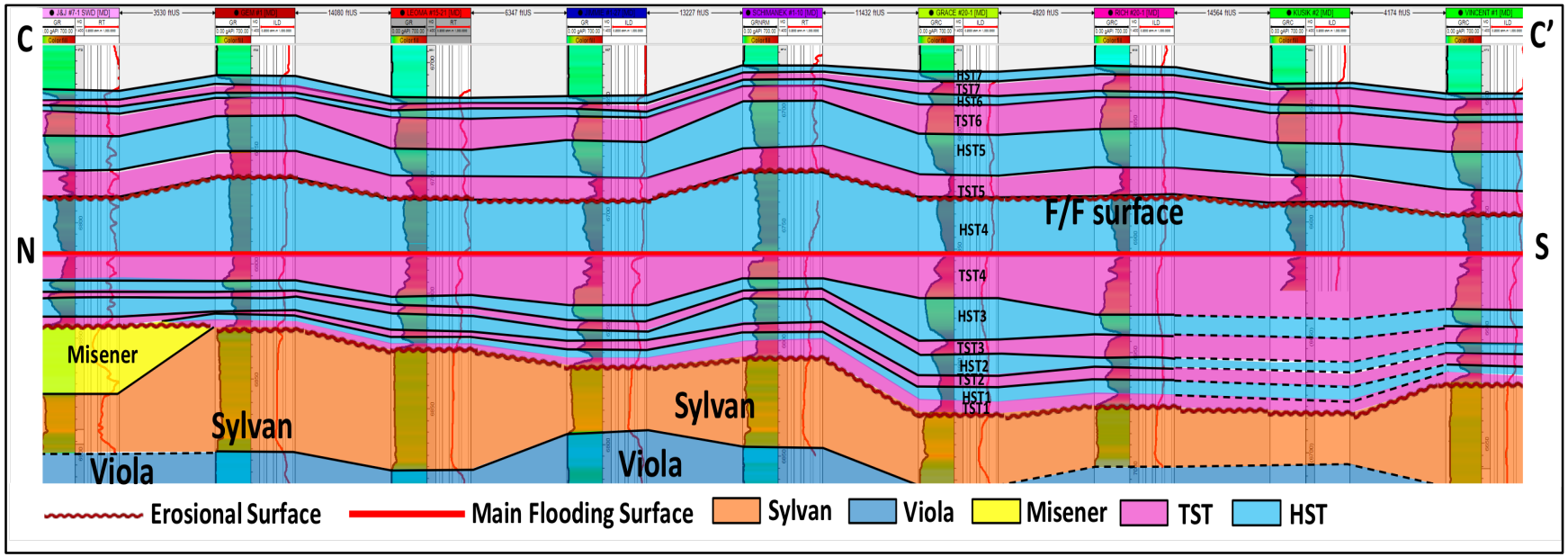

Figure 3.10: Cross section C-C' along the bed strike direction. The parasequences are more continuous and of equal thickness. The section thins towards the north and the lower parasequences were not deposited above the Misener sandstone.

.

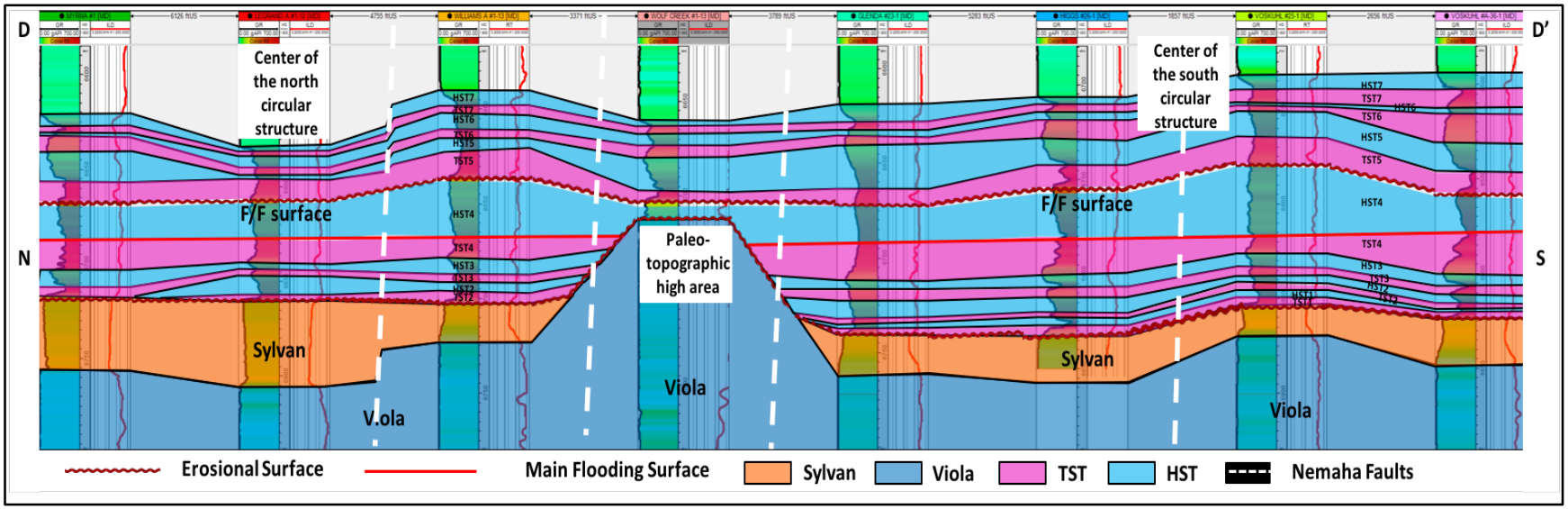

Figure 3.11: Cross section D-D' across two circular structures. The second left well and third right well are located at the central part of the object. The parasequences are almost complete for the two wells even though the thickness of the Woodford is thinner on the left circular structure area.

After correlation and key horizons identification, the thickness of the parasequences were mapped to better characterize the internal characteristics of the Woodford. In the following pages, parasequence isochore maps are shown from the bottom sequence to the top. Overall, all the parasequences have different thickness distributions. Mapping each parasequence separately is beneficial for exploration and charactering the reservoir. The gray area outlined by a black dashed line in each map is the area with either uncertain picks or no data.

Parasequences 1 and 2 (Figure 3.12) are missing from most of the northeast corner. Parasequence 1 is thicker on the west side and Parasequence 2 is thick in the lower central part, similar to the entire Woodford thickness trend, the Parasequence 3 (Figure 3.13) depocenter has moved to the west central part and the non-depositional zone has narrowed to the east. Parasequence 4 (Figure 3.13) increases in overall thickness with the non-deposition zone narrowed to a smaller area. For parasequence 5 (Figure 3.14), there is no areas of non-depositional. The average thickness is 30 feet but thicker on the southwest side and thinning on the northeast side. Parasequences 6 (Figure 3.14) is thinner again with a narrow zone on the northwest side, trending northwest to southeast. Parasequence 7 (Figure 3.15), the top of the sequence set, thins from the northeast corner towards the center. Note that some of the parasequences such as 1 and 2 are not as detailed as other parasequences due to the limitation of data points. There do exist some uncertainty for the isochore maps below.

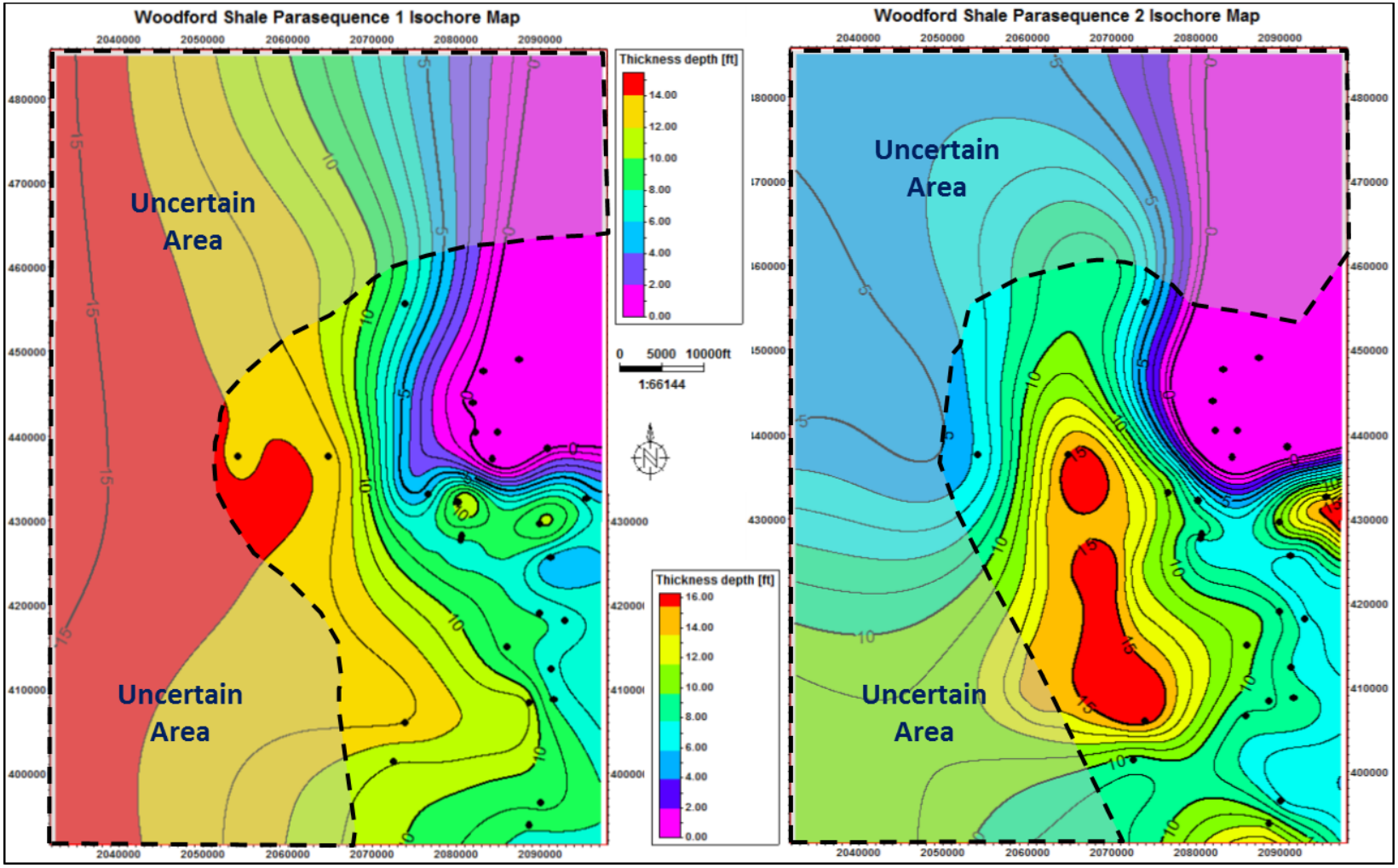

Figure 3.12: Parasequences 1 and 2, the two parasequences were not deposited on the northeast corner and thickens to the west and central part. The black spots are the isochore data points used to generate maps. Gray transparent areas with dashed boundary are the uncertain map area with no data point.

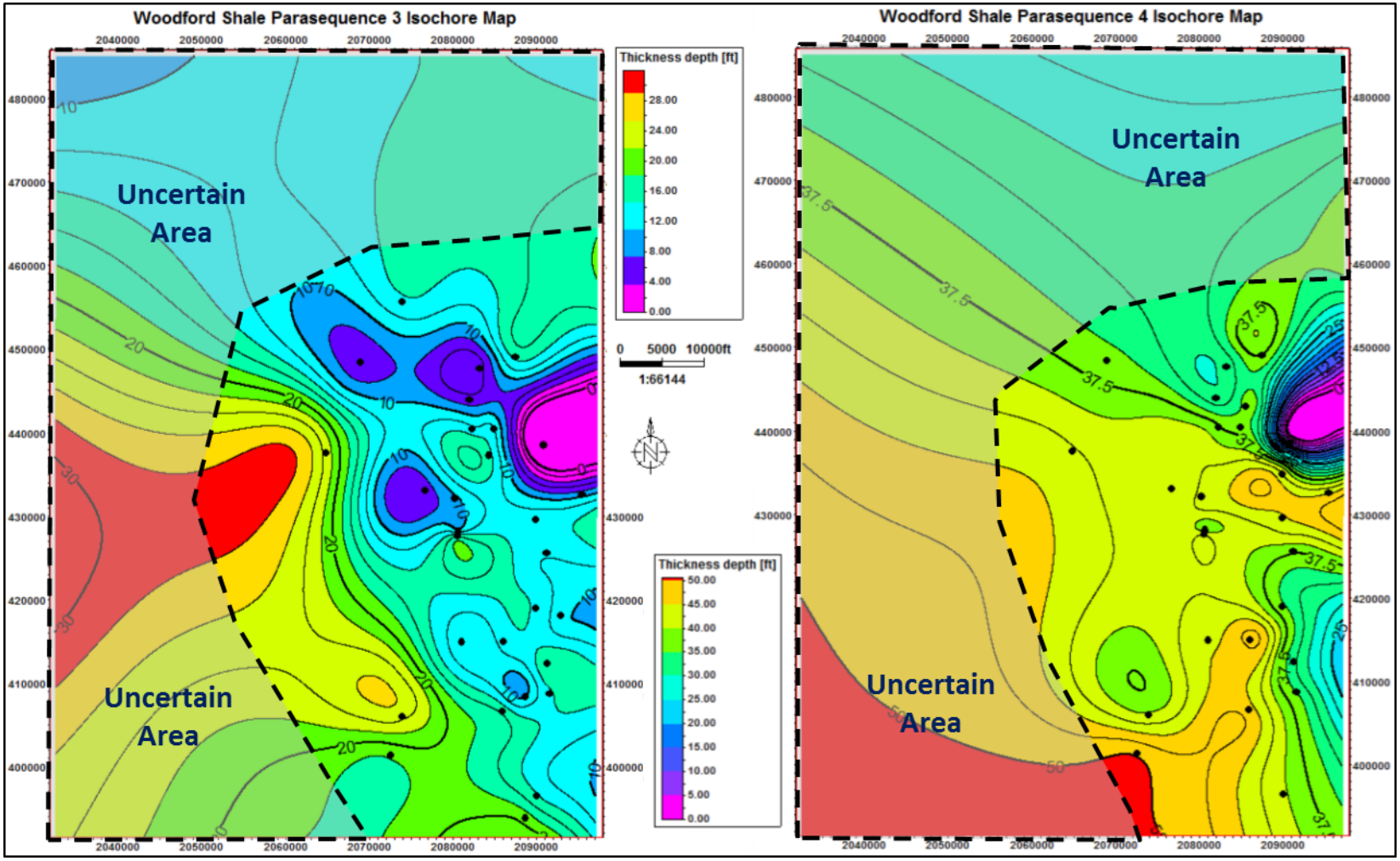

Figure 3.13: Parasequences 3 and 4, the area of non-deposition becomes smaller and extends more southward. Southwest part is thicker than the remainder of the area. The black spots are the isochore data points used to generate maps. Gray transparent areas with dashed boundary are the uncertain map area with no data point.

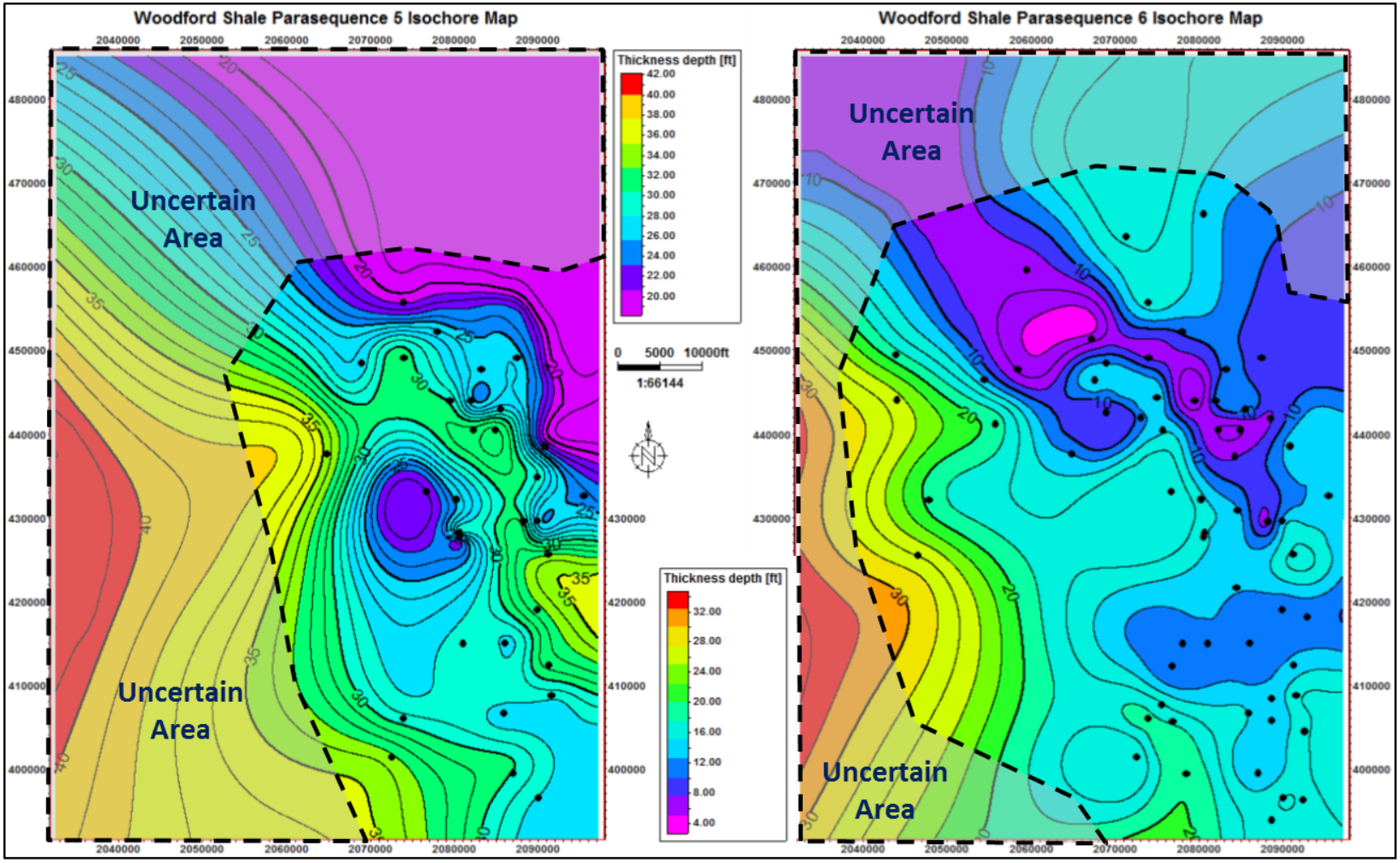

Figure 3.14: Parasequences 5 and 6 where the thin area now occurs from the north-east corner to the north-central part. The thicker part is located consistently on the south west side. The black spots are the isochore data points used to generate maps. Gray transparent areas with dashed boundary are the uncertain map area with no data point

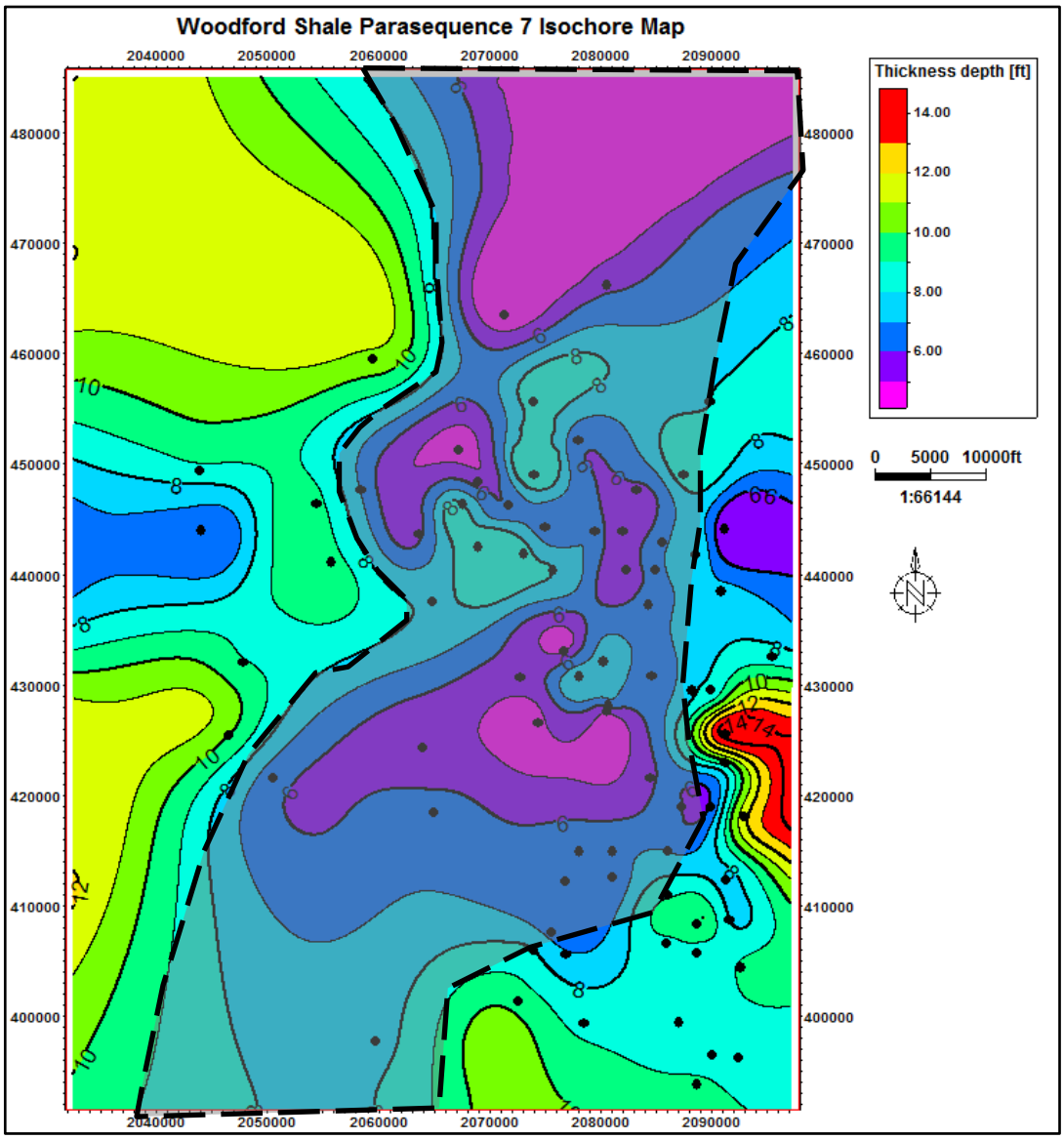

Figure 3.15: Parasequence 7, the top parasequences where the thinner part exhibits a valley shape from the northeast corner to the central study area.

Chapter 4: Mineralogy Analysis

4.1 Mineralogy Composition Analysis

The mineral content of the Woodford Shale is mainly obtained from the drill cutting samples by conducting the quantitative XRD bulk analysis. The mineral content percentage is then used for depositional environment analysis and brittleness calculation (Brady et al., 1995; Rickman et al., 2008; Wang and Gale, 2009; Butt, 2012; Jin et al., 2015). For this research, there are nine samples' XRD data measured at the University of Oklahoma Powder X-Ray Diffraction Laboratory: three samples are from the A1 well, three samples are from the A2 well and three samples are from the C1 well, respectively. There are also 22 interpreted XRD data provided by Longfellow Energy from the H2 well. The sample depths summary is shown in Table 4.1.

Well	**A1**			**A2**			**C1**		
Sample	1	2	3	1	2	3	1	2	3
Depth	6695	6720	6758	7720	7250	7280	6680	6710	6740
Well	**H2**								
Sample	1	2	3	4	5	6	7	8	9
Depth	6820	6840	6860	6880	6900	6920	6940	6960	6980
Sample	10	11	12	13	14	15	16	17	18
Depth	7000	7040	7080	7120	7160	7200	7240	7280	7320
Sample	19	20	21	22					
Depth	7360	7400	7440	7480					

Table 4.1: XRD data point summary from the A1, A2, C1 and H2 wells.

The MDI Jade 2010™ software was used for raw data analysis to obtain the mineral weight percentage from the cutting samples. Overall, the main mineral components in the Woodford Shale cutting are: illite, kaolinite, quartz, calcite, dolomite, pyrite, apatite and chlorite (O'Brien and Slatt, 1990; Kirkland et al., 1992; Chalmer et

al., 2012), the minerals percentage varies by the samples. Calcite is typically rare in the Woodford. The introduction of calcite in samples is mainly because the cuttings were blended with the upper Mississippian Lime formation. Since each mineral has identical parameters such as: interplanar spacing (D), the intensity of X-ray radiation reflection (I) and reflection angle 2 theta (2θ), a fingerprint plot of intensity (counts) vs. 2-theta (degree) was used for each sample to identify the mineral component referenced from the ICDD PDF-4+ database and manuals by Hanawalt (1986) and Harris and White (2008). The peaks and intensities used for reference are shown in Table 4.2.

Mineral	Major d-spacing (2 theta)		
	1	2	3
Kaolinite	7.170(12.33)	1.490(62.26)	3.580(24.85)
Illite	4.430(20.03)	2.560(35.02)	3.660(24.30)
Quartz	3.342(26.65)	4.257(20.858)	1.818(50.14)
Calcite	3.035(29.40)	2.285(39.40)	2.095(43.14)
Dolomite	2.883(30.99)	1.785(51.13)	2.191(41.17)
Muscovite	3.320(26.83)	9.950(8.88)	2.570(34.88)
Ankerite	2.899(30.82)	2.199(41.01)	1.812(50.31)
Sanidine	3.260(27.33)	3.220(27.68)	3.270(27.25)

Table 4.2: D-spacing and 2 theta value for common minerals in the Woodford that help mineral identification from XRD lab results (Harris and White, 2008).

When analyzing the plots, muscovite peaks are merged with illite peaks, and ankerite peaks are merged with dolomite peaks because of their similar chemical structures and common occurrence in the Woodford Shale (O'Brien, 1990; Kirkland et al., 1992; Chalmer et al., 2012). Figure 4.1 is the third sample from the A2 well fingerprint plot. The peaks are identified and labeled with minerals.

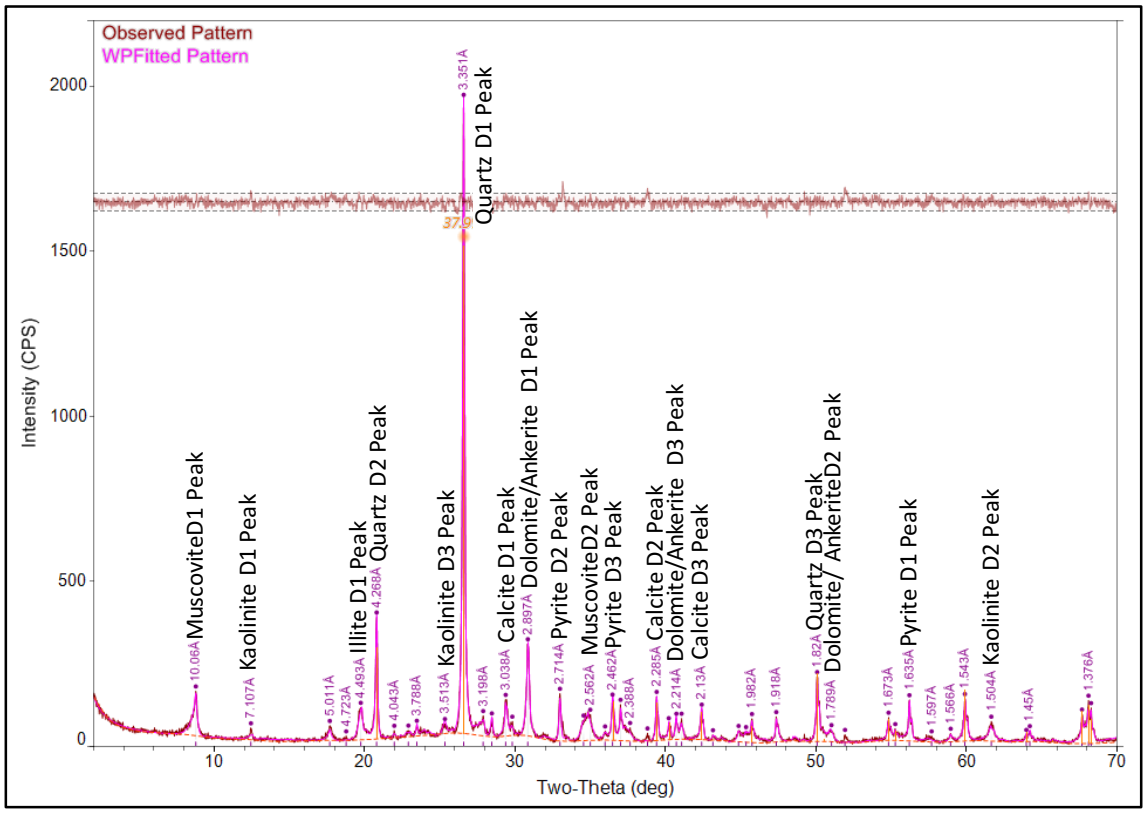

Figure 4.1: Intensity vs. 2 theta plot for the sample from the A2 well. Most peaks are identified with corresponding minerals.

After analyzing the XRD raw data, a summary of the mineral percentage of each sample was calculated (Table 4.3). In the table, the weight percentages of the minerals are recalculated to consider total organic carbon (TOC) percentage for brittleness calculation using the formula proposed by Jin et al., (2015):

$$BI_{Jin\ (2015)} = \frac{Qz + Dol + Cal}{Qz + Dol + Cal + Cly + TOC}$$

In order to better display the data, all the samples' compositions are reorganized into clay, quartz and carbonate percentage and displayed in a ternary plot as shown in Figure 4.2. In the ternary plot, the samples from four wells were plotted based on their clay, carbonate, and quartz percentage. The A1 and C1 wells have abnormal high carbonate content (about 50%) than the other samples due to the cutting blending issue

with the upper Mississippian Lime. The A1 and H2 wells' data points are more concentrated where clay content is 40-65%, carbonate content is less than 25 % and quartz is 38-60%. For the A2 well, three data points are slightly scattered with 10% variability of the three main components. This is due to the large sampling interval through the entire Woodford Shale. There are a total of three samples blending the whole Woodford formation thus making the variability large. The H2 well is a horizontal well and the sampling started when the well was sub-vertical and was trying to land in the target zone. The true vertical depth gap is small between two samples even though the sampling interval is 20 feet to 40 feet. Thus the blending issue does not affect the H2 well more than the A1, A2 and C1 wells. The H2 well sample XRD data was mainly concentrated in a high clay, low carbonate, moderate quartz zone. High quartz content contributes to the brittleness of the section and makes the drilling and fracturing process conduct smoothly.

Well	Sample	Depth (ft)	Chlorite	Kaolinite	Illite/Mica	Mix Ilite/Smectite	Calcite	Dolomite	Quartz	TOC	BI
C1	1	6680	0.0000	2.1526	9.5331	0.0000	52.5858	9.1231	25.8316	0.7738	0.8754
	2	6710	0.0000	2.3898	26.8847	0.0000	30.3697	6.7710	31.8633	1.7215	0.6900
	3	6740	0.0000	1.0011	17.7191	0.0000	31.2337	14.0151	33.9366	2.0943	0.7919
A1	1	6695	0.0000	5.2872	22.1657	0.0000	34.4687	14.0315	21.5557	2.4911	0.7006
	2	6726	0.0000	0.1026	2.5659	0.0000	42.3888	22.6827	31.9200	0.3398	0.9699
	3	6758	0.0000	0.1021	23.9919	0.0000	21.6438	0.0000	52.2718	1.9903	0.7392
A2	1	7720	0.0000	0.0000	41.6967	0.0000	0.4871	3.7995	49.2956	4.7211	0.5358
	2	7250	0.0000	0.0000	27.0952	0.0000	0.0000	8.4427	60.0806	4.3815	0.6852
	3	7280	0.0000	2.0807	27.1587	0.0000	5.9136	16.4266	43.2567	5.1637	0.6560
H2	1	6820	0.0000	0.0000	30.2292	3.9005	8.7762	5.8508	37.0551	2.5500	0.5849
	2	6840	1.1110	0.0000	36.6626	2.2220	7.7769	6.6659	42.2175	3.0100	0.5685
	3	6860	1.0811	0.0000	33.5135	4.3243	7.5676	4.3243	45.4054	3.5000	0.5746
	4	6880	2.1331	1.0666	26.6638	5.3328	5.3328	2.1331	53.3276	3.7600	0.6095
	5	6900	2.2587	0.0000	33.8811	4.5175	1.1294	6.7762	45.1748	5.5450	0.5346
	6	6920	2.2917	1.1459	36.6678	2.2917	0.0000	4.5835	45.8348	6.2700	0.5088
	7	6940	2.2722	1.1361	37.4915	1.1361	1.1361	5.6805	44.3081	6.0200	0.5155
	8	6960	2.2614	0.0000	37.3134	2.2614	1.1307	6.7843	44.0977	5.4400	0.5239
	9	6980	3.4443	0.0000	34.4432	3.4443	1.1481	6.8886	43.6280	6.1000	0.5214
	10	7000	3.3793	0.0000	37.1726	2.2529	1.1264	5.6322	43.9313	5.7750	0.5106
	11	7040	3.4239	0.0000	37.6626	2.2826	1.1413	5.7065	43.3691	5.6200	0.5062
	12	7080	3.4213	0.0000	37.6347	1.1404	1.1404	5.7022	44.4774	5.6850	0.5173
	13	7120	3.3998	0.0000	37.3980	3.3998	1.1333	6.7996	41.9311	5.2400	0.5021
	14	7160	2.2438	0.0000	40.3882	1.1219	1.1219	7.8533	41.5101	5.1350	0.5080
	15	7200	3.0000	0.0000	37.0000	2.0000	0.0000	9.0000	31.0000	N/A	N/A
	16	7240	2.2200	0.0000	44.4000	2.2200	0.0000	8.8800	35.5200	6.0900	0.4470
	17	7280	3.3546	1.1182	43.6095	1.1182	0.0000	4.4728	39.1368	6.4300	0.4394
	18	7320	2.0811	0.0000	42.6617	2.0811	0.0000	5.2026	40.5806	7.1050	0.4592
	19	7360	3.2895	0.0000	42.7632	2.1930	0.0000	6.5789	38.3772	6.2000	0.4523
	20	7400	3.1973	0.0000	38.3673	3.1973	1.0658	5.3288	42.6303	5.8300	0.4921
	21	7440	1.0613	0.0000	33.9631	6.3681	2.1227	8.4908	41.3925	6.2200	0.5221
	22	7480	3.1532	0.0000	37.8390	4.2043	1.0511	5.2554	42.0433	6.1400	0.4850

Table 4.3: XRD analyzed result summary for all available sample data. The mineral percentage is weight balanced with TOC to calculate brittleness index.

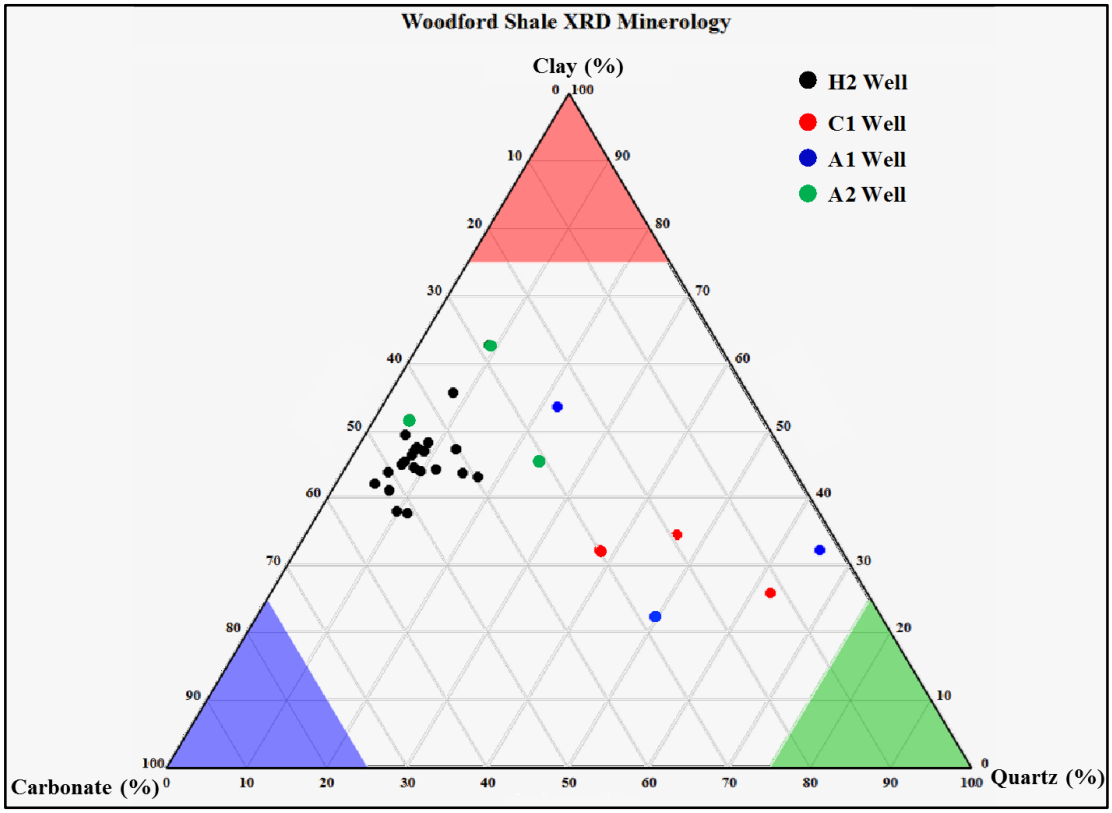

Figure 4.2: Ternary plot of all XRD data. The A1 and C1 samples have more carbonate content. Due to the sample blending issue, the H2 and A2 well samples show more consistent composition, which is clay dominated with moderate quartz content.

4.2 Thin Section Analysis

In order to verify the XRD results of the Woodford Shale cutting samples and to describe the more detailed internal structure of the cuttings, thin sections were made from the cutting sample of different depths and wells. Table 4.4 shows the sample depths summary from the A1, A2, C1, and H2 wells.

Making thin sections from drill cuttings is different than the typical technique for a whole rock. Firstly, mixing 1:1 epoxy A (epoxy resin) and B (hardener) with one ice cube tray volume quickly. It should sit to get rid of bubbles introduced by mixing, then the epoxy mix is gently poured into a plastic ice cube tray. The cutting chips are gently added on the epoxy and the rest of the epoxy is poured on top of the cutting

samples. After pouring all the epoxy in the tray, the epoxy and cuttings are gently stirred to rise the air between cutting samples then the cube sits for 24 hours. Once the cube of cuttings hardens, the following steps of making a thin section is no difference than the regular procedure.

Well	**A1**			**A2**				**C1**		
Sample	1	2	3	1	2	3	4	1	2	3
Depth	6695	6726	6758	7130	7160	7220	7250	6680	6710	6740
Well	**H2**									
Sample	1	2	3	4	5	6	7	8	9	10
Depth	6820	6840	6860	6880	6900	6920	6940	6960	6980	7000
Sample	11	12	13	14	15	16	17	18	19	20
Depth	7040	7080	7120	7160	7240	7280	7320	7360	7400	7440
Sample	21									
Depth	7480									

Table 4.4: Thin section data points summary, note that the A1, A2 and C1 wells cutting thin sections were made by the author and all the thin sections from the H2 well are provided with images.

From all the Woodford Shale thin sections, there are mainly six types of cuttings chips: limestone chips, quartz rich massive mudstone, quartz rich laminae mudstone, black massive organic-rich mudstone, dolomitic mudstone and radiolarian-rich cherty mudstone. The percentage of each type of cutting chip varies by wells and depths.

The carbonate chips are mainly derived from the Mississippian Lime near the formation boundary, thus the component is mainly pure limestone. The limestone chip is mainly present in the thin sections of the A1 and C1 wells where the sample blending is the main issue. The representative image of the limestone chips is shown in Figure 4.3 which is from the C1 well sample number 1.

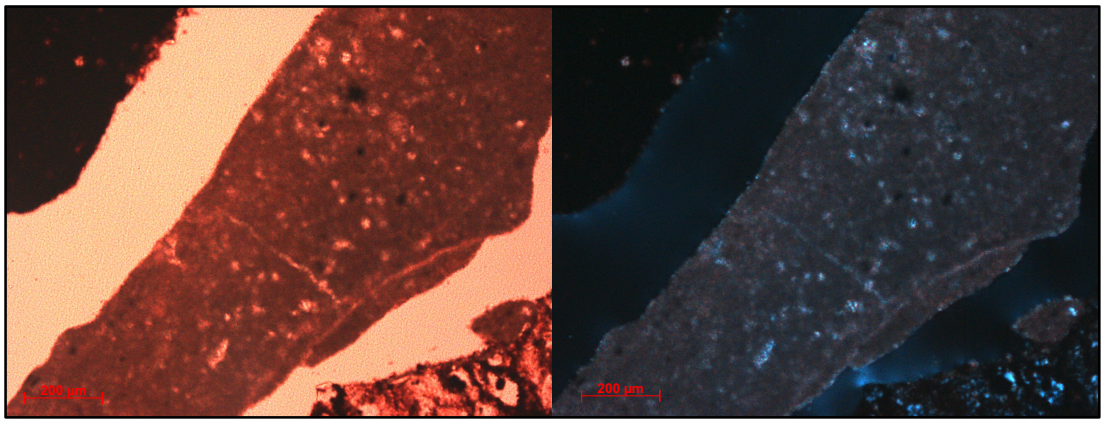

Figure 4.3: Limestone chip from the C1 well sample number one, this is the typical type of the Mississippian Lime cutting blended with the Woodford cutting. The left figure is under plane polarized light and the right figure is under the perpendicular polarized light.

The quartz rich massive mudstone has more orange tone color, and contains more quartz, thus the entire chip has 90° extinction angle under the perpendicular polarized light. There is no obvious internal structure for this type of chip thus it is described as massive. This cutting is interpreted as the shale deposited with thicker bed under moderate flow energy and quartz debris was blended with clay. The demonstration of this type of chip is shown in Figure 4.4, the chip is from the A2 well first sample. In the figure, bright spots are the quartz debris within the clay matrix.

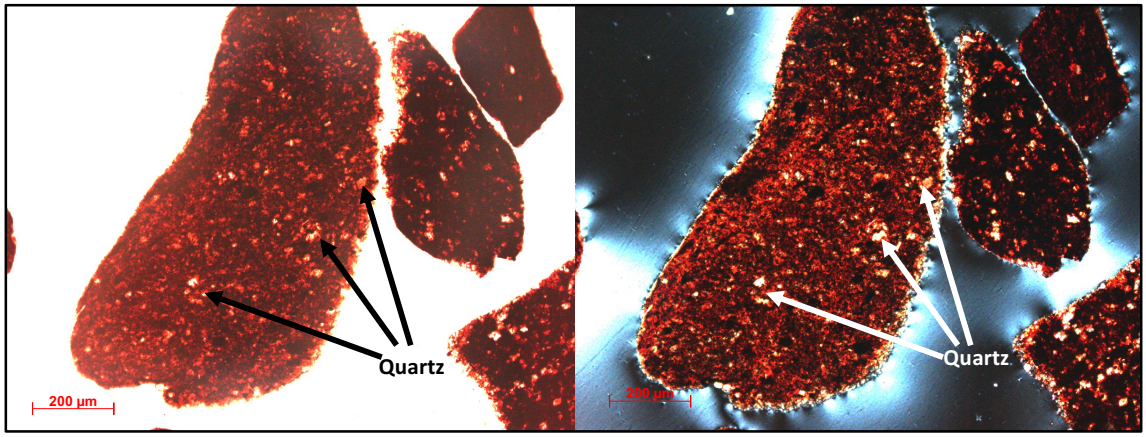

Figure 4.4: Quartz rich massive mudstone cutting, the color is orange to light brown. The bright spots are the quartz debris; the chip has 90-degree extinction angle under the perpendicular polarized light (right).

The quartz rich laminae mudstone is similar to the former one but with observable laminae. The color of chips is typically dark brown and they have more clay instead of quartz than the former one. This type of cutting is interpreted as the mud deposited under a low flow energy that forms the very thin laminae while clay was depositing. The demonstration of this type is shown in Figure 4.5; the cutting sample is from the A2 well second sample.

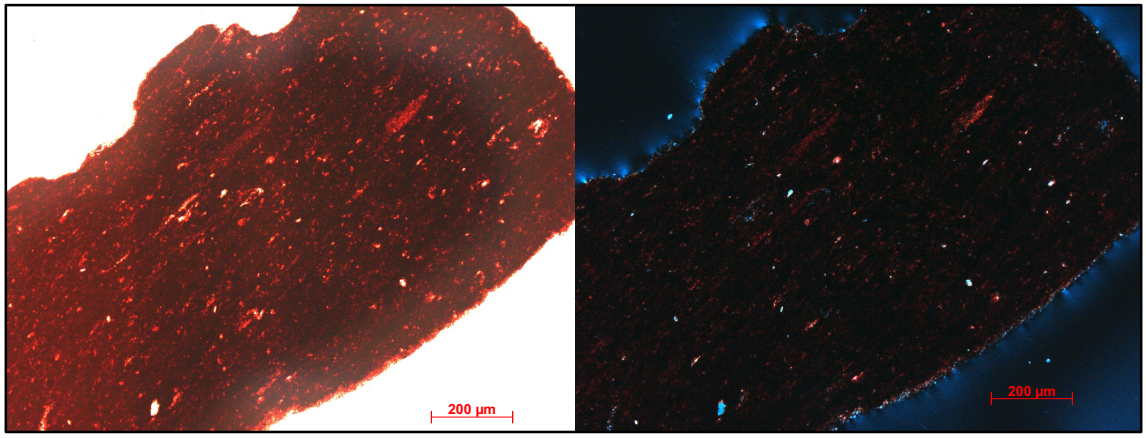

Figure 4.5: Quartz rich laminae mudstone the laminae is highlighted by the flattened quartz flakes, the depositional environment is interpreted as low energy flow environment to maintain the laminae as internal structure. The left figure is under plane polarized light and the right figure is under the perpendicular polarized light.

The black, massive, organic-rich mudstone is the chip with dark brown to black color and no observable internal structure. It is pure clay with organic matter that makes the cutting black and opaque. Locally it contains chert which replaced tasmanites. The tasmanites is flattened from the original circular shape into wavy like shape. The demonstration of this type of cutting is shown in Figure 4.6. The cutting sample is from the third sample of the A2 well. Tasmanites in the figure are replaced by chert with undulose extinction. The tasmanites in the Woodford Shale is the main contributor of organic matter, thus it mainly appears in the massive, black, organic-rich mudstone.

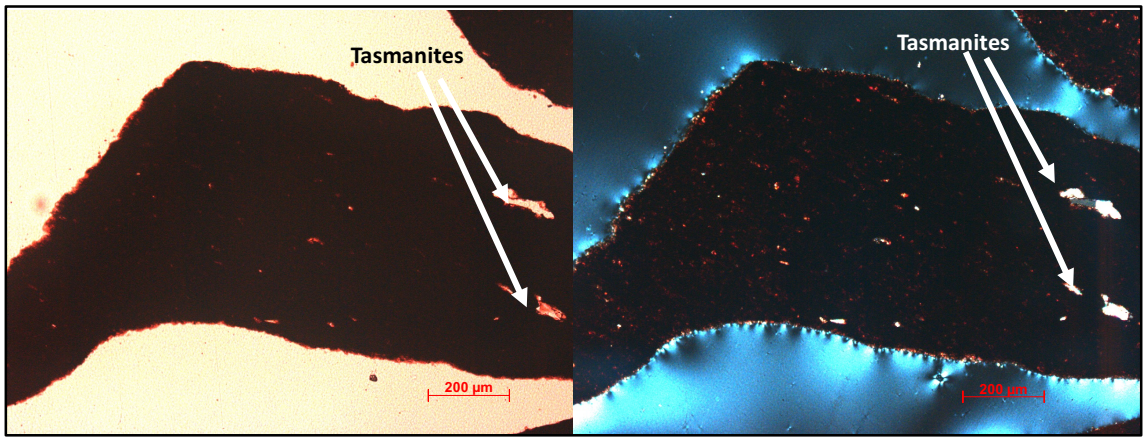

Figure 4.6: The black massive organic-rich mudstone cutting, black color is contributed by the clay minerals and organic matter within the cutting. Tasmanites occurs occasionally in wavy like shape. The left figure is under plane polarized light and the right figure is under the perpendicular polarized light.

The dolomitic mudstone is the cutting type that has dolomite crystal growth after deposition (McHargue and Price, 1982). Identical diamond shape dolomite crystals are scattered within the massive black shale matrix. The dolomite crystal percentage varies from 40% to 80% in the clay matrix which depends on the depositional history. The demonstration of this type of cutting is shown in Figure 4.7. The cutting in the figure is from the A2 well second sample.

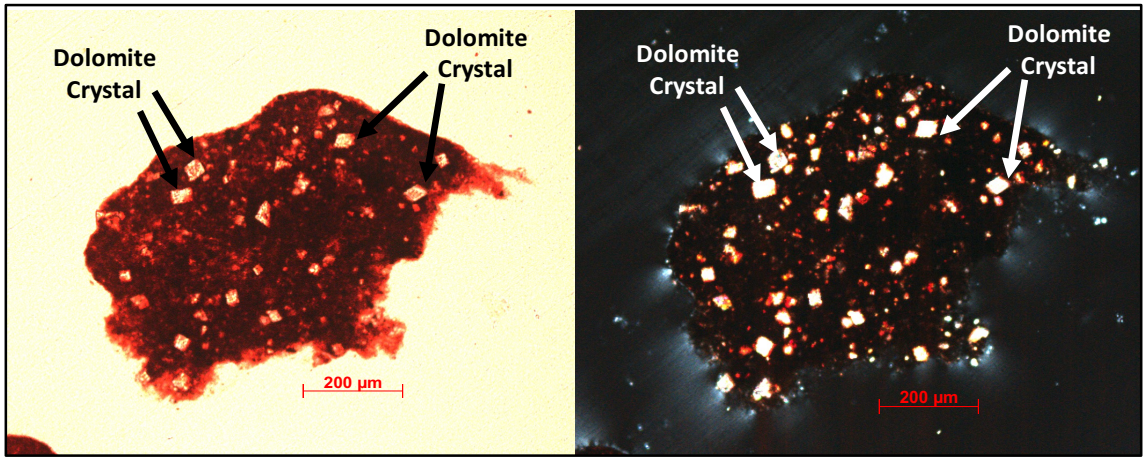

Figure 4.7: The dolomitic mudstone. The dolomite is crystalized after deposition of shale. The left figure is under plane polarized light and the right figure is under the perpendicular polarized light.

The radiolarian-rich cherty mudstone is one of the main components of the upper Woodford, where the chert beds start to occur in the formation. The radiolaria mostly retain their original rounded shape or slightly compacted into elliptical shape. Most of them were replaced by chert after deposition. Pyrite is observed in the center of some radiolaria as opaque diamond shaped crystals; this means the pyrite is crystalized after the replacement of radiolaria. This feature suggests the radiolaria is replaced by chert within a short period after deposition, thus it can maintain the original shape before compaction. The cherty radiolarian rich shale is deposited at the shelf margin area with less detrital sediment input and less water circulation, pyrite occurrence in the center of radiolarian also indicates the more anoxic environment of deposition (Knoll and Barghoorn, 1974; Noble and Renne, 1990; Phillips and Dong, 2010). The demonstration of this type of cutting is shown in Figure 4.8. The cutting is from the first sample of the A2 well.

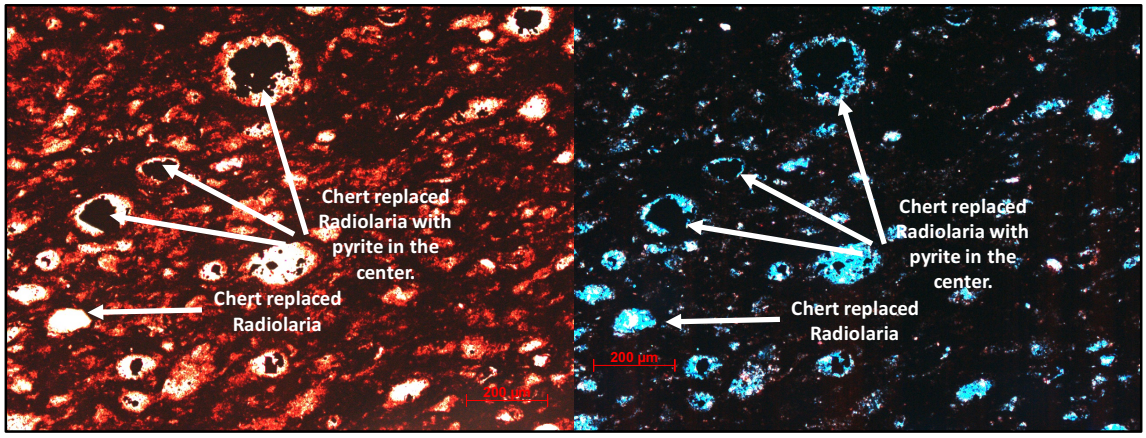

Figure 4.8: The radiolarian-rich cherty mudstone. Some radiolaria center have opaque pyrite that formed after the chert replacement. The left figure is under plane polarized light and the right figure is under the perpendicular polarized light.

The A1 well cuttings are composed mainly of the limestone cuttings and black massive organic-rich mudstone. The first sample has 70% of limestone with 30% of

black shale. The second sample is almost only limestone which explains the XRD result and low TOC from Table 4.2. The third sample of the A1 well has an increase of shale cuttings to 60%, then the dolomite in mudstone starts to appear within radiolarian-rich cherty mudstone and silty to sandy massive mudstone cuttings. The A2 well has a significant increase in shale cuttings percentage. The silty to sandy massive mudstone is 70% in the top sample. Deeper there is an increase in black, massive, organic-rich mudstone. The deepest sample of the A2 well contains 70% of organic-rich mudstone and merely observes the siliceous mudstone cuttings. This trend represents the increase in clay and organic matter in the formation and also corresponds with the gamma ray response, because higher percentage of organic rich mudstone has higher gamma ray response. The C1 well has all types of cutting chips described above and the amount of each type is similar between the samples: about 50% limestone chips, 20% siliceous mudstone, 10% radiolarian-rich cherty mudstone and 20% massive organic-rich mudstone. The H2 well cutting samples have fewer limestone chips. The upper part is mainly silty to sandy mudstone cuttings and radiolarian-rich cherty mudstones in thin sections with an increase in measured depth, down to the horizontal well landed zone the cuttings become massive organic-rich mudstone and dolomitic mudstone.

Chapter 5: Chemostratigraphy Analysis

5.1 Cutting sample XRF analysis.

The Hand Held X-Ray Fluorescence (HHXRF) is a useful tool to understand the paleo depositional environment, correlations, and the sediment content by scanning the elemental composition of each sample. It has been utilized in unconventional shale reservoir characterization by studying core (Rowe et al., 2009; Rowe et al., 2015), outcrop samples (Turner et al., 2015), and drill cutting sample (Seyfarth et al., 2014). This thesis research utilized drill cuttings along a horizontal well bore. The XRF procedure is to scan cores and outcrop samples to obtain a high resolution vertical profile of elements and reconstruct the paleo-depositional environment. However, drill cutting samples from a vertical well have a 20 to 40 feet sampling interval, which is too generalized to provide detailed and high resolution vertical chemo profiles.

For the Woodford Shale in the study area, the average thickness is about 100 feet. When the sampling interval is 40 feet, there are only 3 bags of samples in total for the Woodford and that includes blended cuttings from the upper formations. Horizontal well drill cuttings are a common data source and have better vertical resolution because the well track only stays and fluctuates up and down within a smaller vertical depth range. Measuring the cutting sample XRF profile along the horizontal well is also an effective way to characterize the horizontal heterogeneity within the target zone.

For mudrock interpretation, this research used several specific elements as proxies for minerals based on previous studies. Ti and Zr are used as continental sediment proxies (Finlow-Bates and Stumpfl, 1981; Tribovillard et al., 2006). Ca and Sr are the carbonate rock proxies; Sr is especially correlated with dolomite (Banner, 1995).

K and Al are the most common elements in the mudrock, occurring in clay minerals such as illite and kaolinite and potassium feldspar (Perry and Hower, 1970; Tribovillard, et al., 2006). Mo and V are two elements mainly preserved in the anoxic environment, thus they are indicators of a deep, low circulation water column environment (Tribovillard et al., 2006; Algeo and Rowe, 2012). Si/Al, and Si/Ti are also calculated to identify the quartz content and source, if the Si/Al and Si/Ti ratios are high, there is high quartz content. The same is true for high Si/Ti ratio. The quartz is biogenic instead of detrital which Si/Ti and Si/Al are both high (Pearce and Jarvis, 1992; Pearce et al., 1999; Tribovillard et al., 2006).

In this research, cutting samples along the H2 well were measured and compared with the other types of data since the H2 well drill cuttings were less to none contamination that is caused by the upper formation limestone so the Ca elemental level in most deeper measured depth sample can represent true component in the Woodford shale instead of contamination from Mississippian Lime. The measurements start close to the formation boundary where the well track is still vertical. 147 cuttings samples were measured for both major and trace elements and calibrated into the ppm unit after scanning. After calibration, all the elemental data was compiled together and hierarchical clustering analysis (HCA) was conducted. HCA is a technique that quickly sorts the data points based on similarities between each other (Ward, 1963; Kaufman and Rousseeuw, 1990; Lior, 2005). The software used for HCA is an Excel plug-in called XLSTAT. The similarities are calculated with the Euclidean distance method. The first software sorting has 20 groups, which are then manually combined into a similar set of 12 groups with moderate dissimilarity. In Figure 5.1, the software sorted

all 147 samples into 20 groups. Second round manual sorting is based on the calculated average value of all the element proxies for each group. Two groups are manually combined if most of the proxy elements have a similar average value and low group dissimilarity. The final 12 groups are interpreted as 12 chemofacies along the horizontal well track. For each group, the proxy elements average values are shown in Table 5.1, which is used for paleo-environment and deposit composition interpretation. Note that there are still some contaminations in the upper most samples (limestone component from upper Mississippian Lime). From Table 5.1, chemofacies 12 has the highest Ca ppm and samples which are chemofacies 12 mainly distributed in shallow measured depth which are close to formation top, thus the high Ca reading is highly possible caused by sample contamination instead of true mineral in place, interpretation of chemoface 12 need to exclude the effect of Ca.

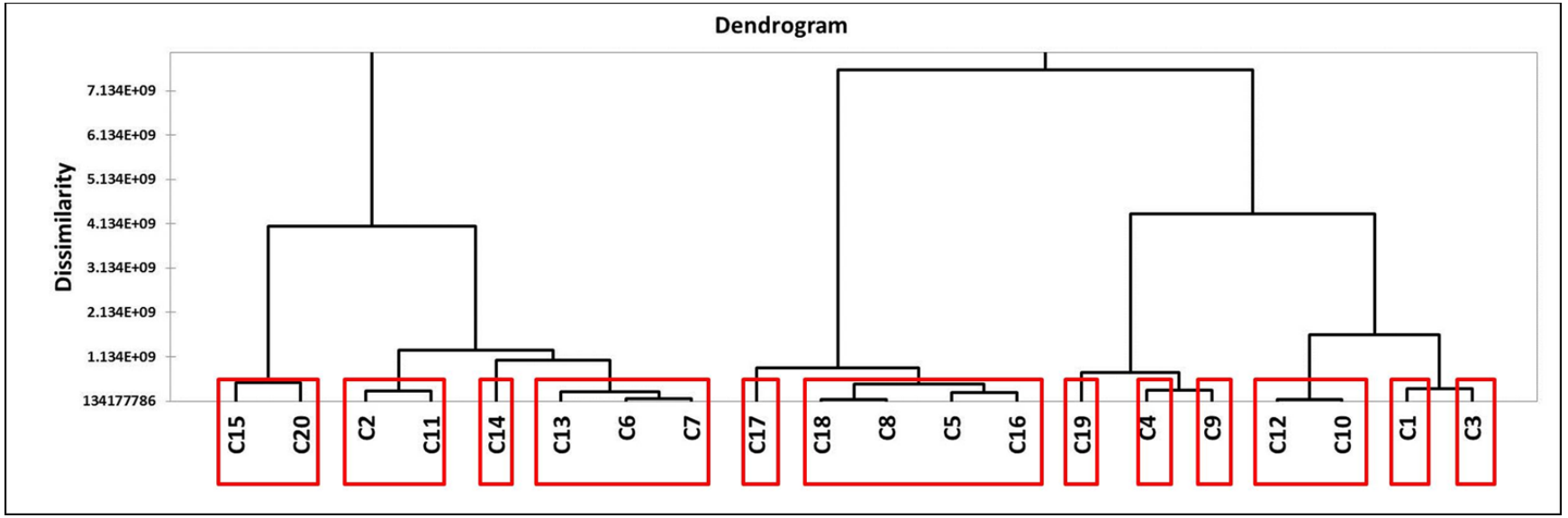

Figure 5.1: Dendrogram showing the group distribution and dissimilarity level. The black character represents the original group sorting by the software, the red rectangles represent the manually sorted groups based on the dissimilarity of group average values.

Chemofacies	Al (ppm)	Si (ppm)	S (ppm)	K (ppm)	Ca (ppm)	Ti (ppm)	V (ppm)	Zr (ppm)	Mo (ppm)	Si/Al	Si/Ti	Si/K
1	10957.77	78482.33	4547.22	10860.57	7684.65	1309.40	218.84	117.95	102.83	7.17	60.00	7.29
2	6489.80	57953.10	3014.95	14402.93	8199.88	1845.22	322.68	121.80	108.91	9.07	34.92	4.46
3	13728.54	103632.74	5488.85	14114.08	26317.54	1923.17	228.69	110.12	75.13	7.70	56.51	7.54
4	14307.01	105744.75	4960.71	16217.44	8728.44	1932.39	355.22	128.13	124.94	7.42	55.33	6.58
5	12612.54	90293.51	5616.06	13274.42	19502.21	1765.54	217.91	122.24	80.71	7.17	51.29	6.81
6	13006.23	95512.07	5329.29	14897.31	10382.50	1838.83	285.67	121.60	114.02	7.37	52.49	6.44
7	22831.64	158995.15	6826.95	20182.96	9179.16	2234.27	464.97	125.53	131.46	6.97	72.05	7.94
8	21111.41	146900.83	8456.23	18832.85	13735.51	2172.37	307.93	119.31	109.47	6.98	67.97	7.83
9	16721.30	122599.46	5557.75	16722.19	9653.86	1900.65	274.61	123.70	105.09	7.35	64.79	7.35
10	19612.37	133554.01	8425.49	17815.86	12731.97	2085.00	264.94	119.46	96.68	6.85	64.26	7.53
11	20610.45	141280.10	7758.76	17928.93	27516.45	2371.91	277.54	116.41	69.67	6.87	59.61	7.88
12	16321.87	124818.27	6077.10	15319.90	36786.71	2068.60	227.34	100.47	64.25	7.86	61.73	8.30

Table 5.1: Average elemental level of 12 defined chemofacies. Elements listed are the proxies used for interpretation.

To connect the elemental levels with sequence stratigraphy, all the environmental proxies are used for comparison and interpretation. The interpretation method of horizontal XRF profile is different than the vertical profile. For the vertical profile, the interpreter focuses on the fluctuation of each element proxy in the vertical scale, which provides clues for regional correlation and constructing sequence stratigraphic framework.

For a horizontal profile this thesis proposes a new method to characterize cuttings XRF. It focuses on single well characterization， especially the brittleness evaluation and local environment interpretation by comparing the differences between the 12 chemofacies. For the H2 well case study, average element concentrations of 12 chemofacies after HCA were plotted in Figure 5.2. Each colored line represents one elemental proxy, 12 columns on the plot represents 12 chemofacies. Thus the fluctuations of lines along the horizontal axis reveal different chemofacies. Chemofacies are interpreted based on the fluctuation and defined as either transgressive system tract or highstand system tract. The transgressive system tract should contain low continental proxies (Ti and Zr), Al and K should remain at a high level relative to Ti and Zr, and high Mo and V due to increase in water depth. Highstand system tract should have the characteristics of low Mo and V due to high water circulation and shallower water depth. Ca, Sr, Ti and Zr increases to high levels implies more detrital inputs and getting more close to the shore line. The summary of each chemofacies characteristics and interpretation are shown in Table 5.2.

Note that the words high and low elemental level, deep and shallow water depth in the description chart are interpretative terms, there is no absolute reference for the

water depth since there is no direct relationship between each chemofacies. The trend between neighboring points is not related. Based on the interpretation, the XRF horizontal profile can be used to estimate brittleness along the well bore, which provides benefits for fracturing job design. The estimation will be discussed in the third section of this chapter.

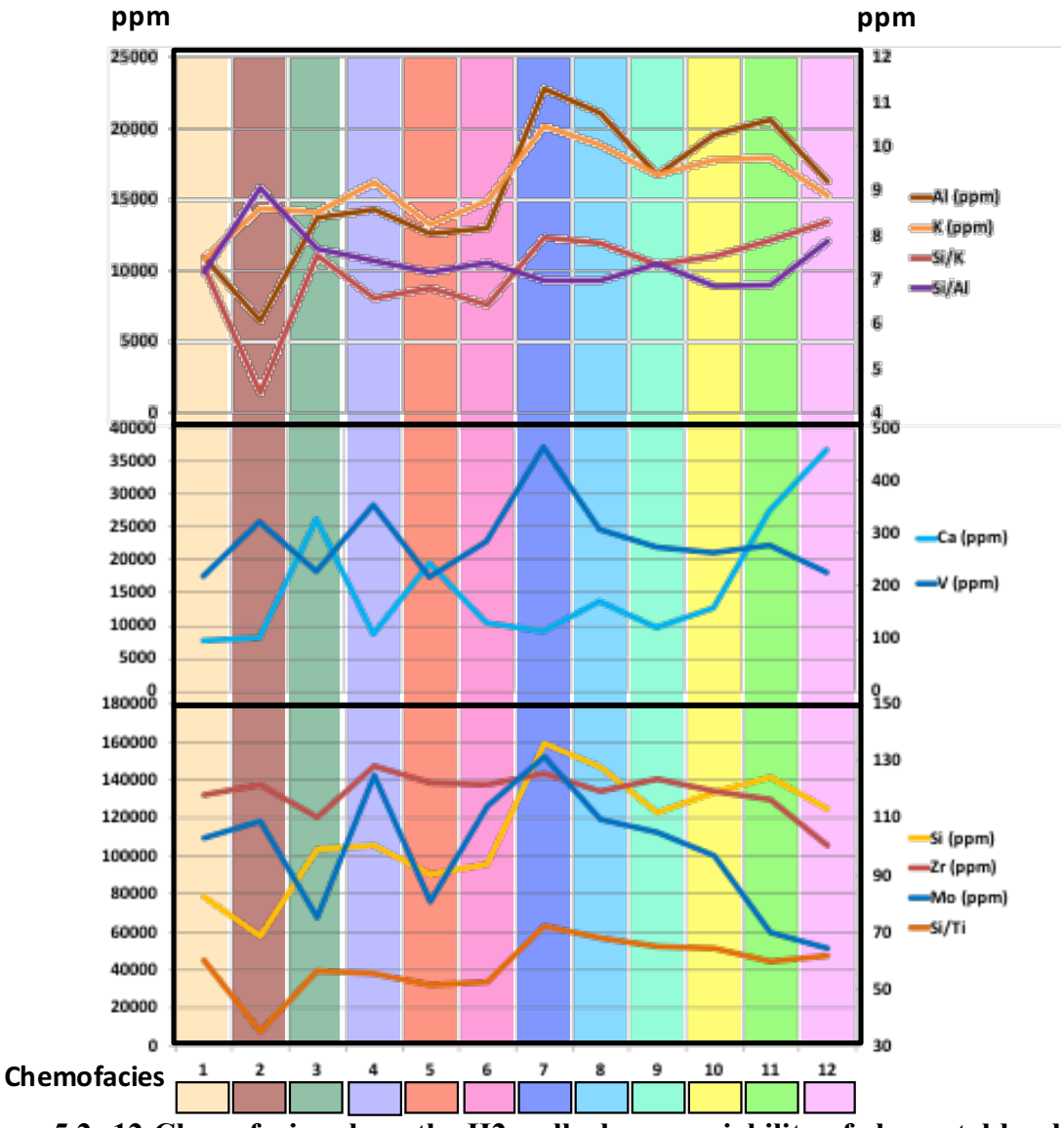

Figure 5.2: 12 Chemofacies along the H2 well, shows variability of elemental level between each facies. Each colored column represents a chemoface, the curves fluctuations are the proxy elements ppm level of the correspond chemofacies. The interpretation of 12 chemofacies is based on the fluctuation of the proxies.

Chemofacies	Characters	Interpretation	Stratigraphy Preference
Chemofacies 1	Moderate to low Al, K, Ca, Moderate to high Mo, moderate V	Low clay and carbonate deep water shale with low detrital input	TST
Chemofacies 2	Low Ca, Si/K, Al, Si, Si/Ti Moderate Mo and V	Detrital input dominates shallow marine shale	HST
Chemofacies 3	Low Mo and V Moderate Si/K, Si/Al, Si/Ti High Ca	Less detrital input with carbonate and biogenic quartz mix	TST
Chemofacies 4	Low Ca and Si/K Moderate Si/Ti Very high Mo and V	Deep water depth or low circulation water column while deposition, clay mineral and biogenic quartz dominate	TST
Chemofacies 5	Low Mo and V Moderate Al and K Moderate to high Ca	Shallow water, medium detrital input	HST
Chemofacies 6	Moderate Si, Si/Ti and Si/K Moderate to high Mo and V,	Low level circulation with moderate amount of detrital input, low carbonate content.	TST
Chemofacies 7	Low Ca High Mo, V, Al, K, Si/Ti and Si/Al	Deep water depth with low carbonate, high clay and biogenic quartz	TST
Chemofacies 8	Moderate high Mo, V, Si/Ti, Al and K	Moderate constrained water circulation, clay and biogenic quartz dominate	TST
Chemofacies 9	Low Ca Moderate Mo, V, Si/Ti, Al and K	Biogenic quartz and few clays deposit	HST
Chemofacies 10	Moderate Mo, V, Si/Ti, Al and K	Medium water depth with medium clay content	HST
Chemofacies 11	Low Mo and V High Al, K and Ca	High level water column circulation, high carbonate and clay content	HST
Chemofacies 12	Low to moderate Mo and V. High Si/Ti, Si/K and Ca	Low detrital input with high level water circulation, high Ca not necessary represents the high carbonate in the formation due to the contamination	HST

Table 5.2: Summary of 12 chemofacies characters, interpretation and preferred sequence system tract. The descriptive term in the interpretation is not an absolute value but a relative descriptive term.

5.2 Chemofacies Modeling

Once the chemofacies are defined, they can be input into Petrel™ as data points along the horizontal wellbore, as shown in Figure 5.3. In order to better display the model and chemofacies the model is 40 times vertically exaggerated. The background grid is the fine grid model intersection along the well track. Since the Woodford Shale surface in this small area is flat and parallel between each parasequence surface, the model used the Woodford top and Woodford base as the input surfaces, 50 layers divided the entire formation proportionally with thickness of 5 feet thick. The same chemofacies can be traced along the same layer for certain distances. For example, the chemofacies number 8, with the blue color grid can be traced on both sides of the well track fluctuation in Figure 5.3. Spherical variograms were estimated by tracing the chemofacies along the model layer. Since some layers have limited data points, there are some errors during estimation. Each horizontal variogram of chemofacies is estimated individually and the vertical anisotropy is set manually as 3 feet due to limitation of data points. The horizontal variogram range is mainly estimated from the major direction which is the H2 well track strike direction; the minor direction variogram is estimated based on the major direction to keep the facies in a circular shape because the chemofacies data points are mostly distributed in the major direction. The chemofacies percentage and variograms summary are shown in Table 5.3.

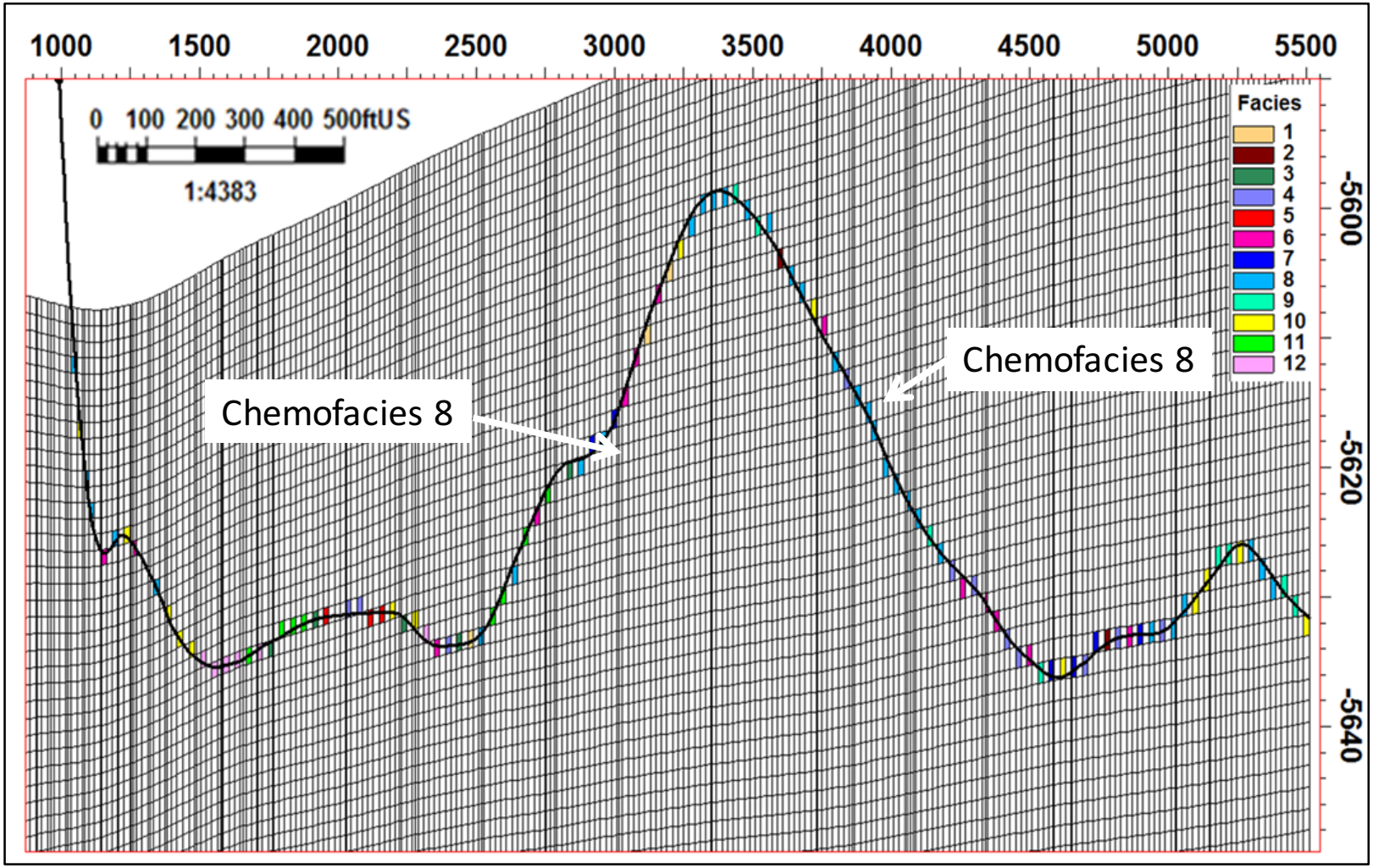

Figure 5.3: Chemofacies in fine grid Woodford model. The well track is 40 times vertically exaggerated to show the distribution and details.

Chemofacies	Percentage	Horizontal Major Direction Anisotropy	Horizontal Minor Direction Anisotropy	Vertical Direction Anisotropy
Chemofacies 1	2.56	2106.833	2000	3
Chemofacies 2	2.22	2223.271	2200	3
Chemofacies 3	4.74	1943.821	1900	3
Chemofacies 4	11.36	1757.521	1700	3
Chemofacies 5	3.18	2394.045	2300	3
Chemofacies 6	10.16	1516.885	1300	3
Chemofacies 7	5.85	1252.961	1200	3
Chemofacies 8	27.3	1788.57	1700	3
Chemofacies 9	8.15	903.648	900	3
Chemofacies 10	11.46	732	700	3
Chemofacies 11	7.05	1617.797	1600	3
Chemofacies12	5.95	2549.294	2500	3

Table 5.3: Chemofacies percentage and variogram for modeling, 12 chemofacies have different horizontal anisotropy range.

Based on the estimated variogram, the chemofacies are modeled using the sequential indicator simulation method in Petrel™ (Figure 5.4). From the intersection of the model, the chemofacies are not a layer by layer structure like a geologic framework. This is mainly because the chemofacies reflect more details and the shale reservoir lateral heterogeneity. However, the chemofacies distribution model's accuracy outside the vertical range of the H2 well track is less because of the lack of raw data. In order to obtain a high accuracy model for the entire formation, multiple horizontal wells' XRF profiles in the nearby area are necessary.

The chemofacies model result is verified by the H1 well, which is close to the H2 well head. The vertical chemofacies profile is projected from the model to the H1 well location. From Figure 5.5, the chemofacies vertical profile matches the sequence

stratigraphic surfaces interpreted from the well logs of the H1 well. This vertical profile verified the accuracy of the chemofacies model, but the model may only be used for the nearby area to retain the accuracy, and to assist the future well landing decision.

The chemofacies do have a relationship with sequence stratigraphy. From Figure 5.5 HST preferred chemofacies are more likely to stay within the HST sections defined from the well logs, and TST preferred chemofacies are more likely to stay within the TST sections. For the entire Woodford Shale with seven parasequences, there is no direct relationship between chemofacies with certain parasequence, since the chemofacies are defined based on the data from portion of the Woodford, so chemofacies cannot be used for direct correlation with parasequences.

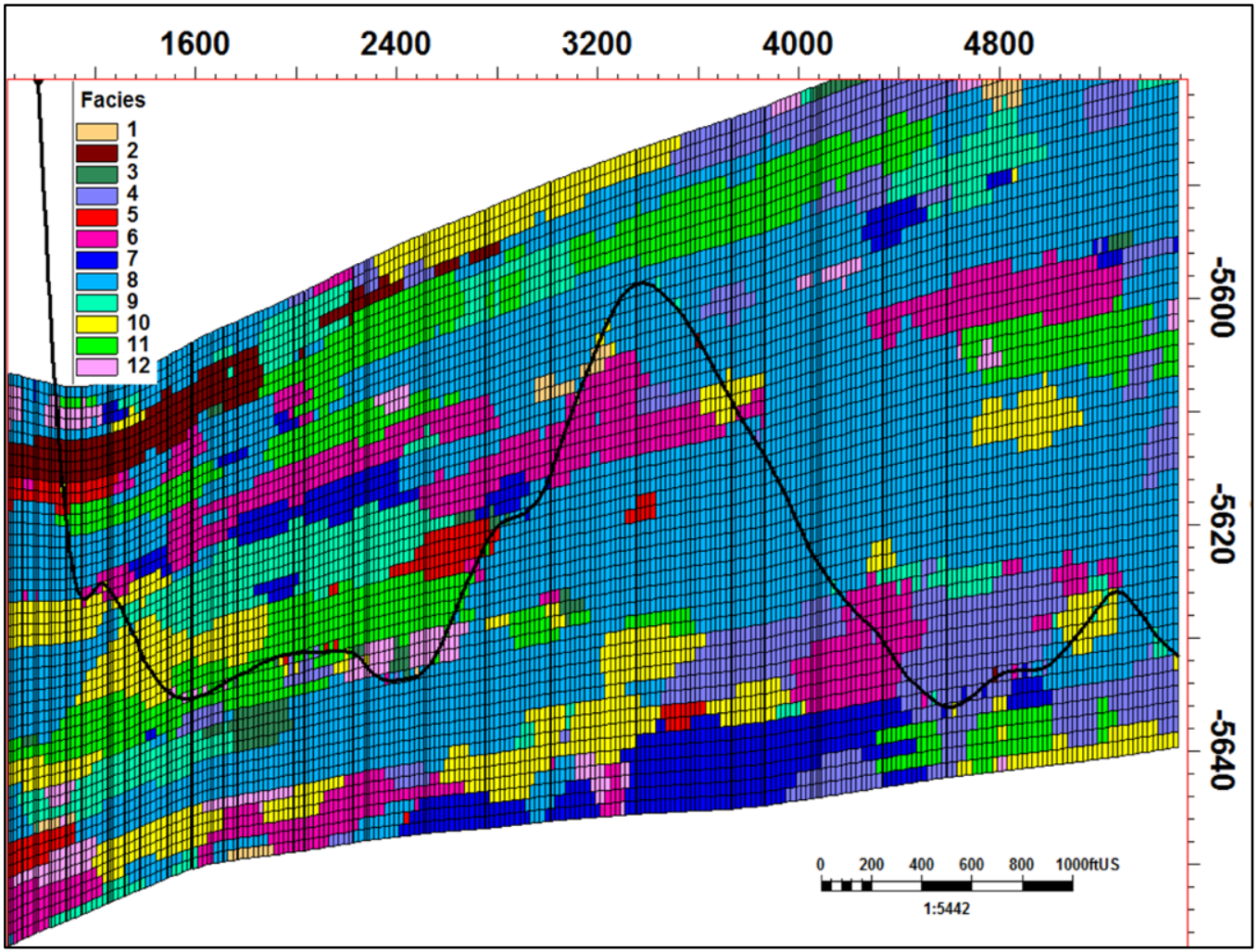

Figure 5.4: Chemofacies model along the horizontal well track intersection. The chemofacies distribution is not the pancake model. This model reflects the reservoir heterogeneity.

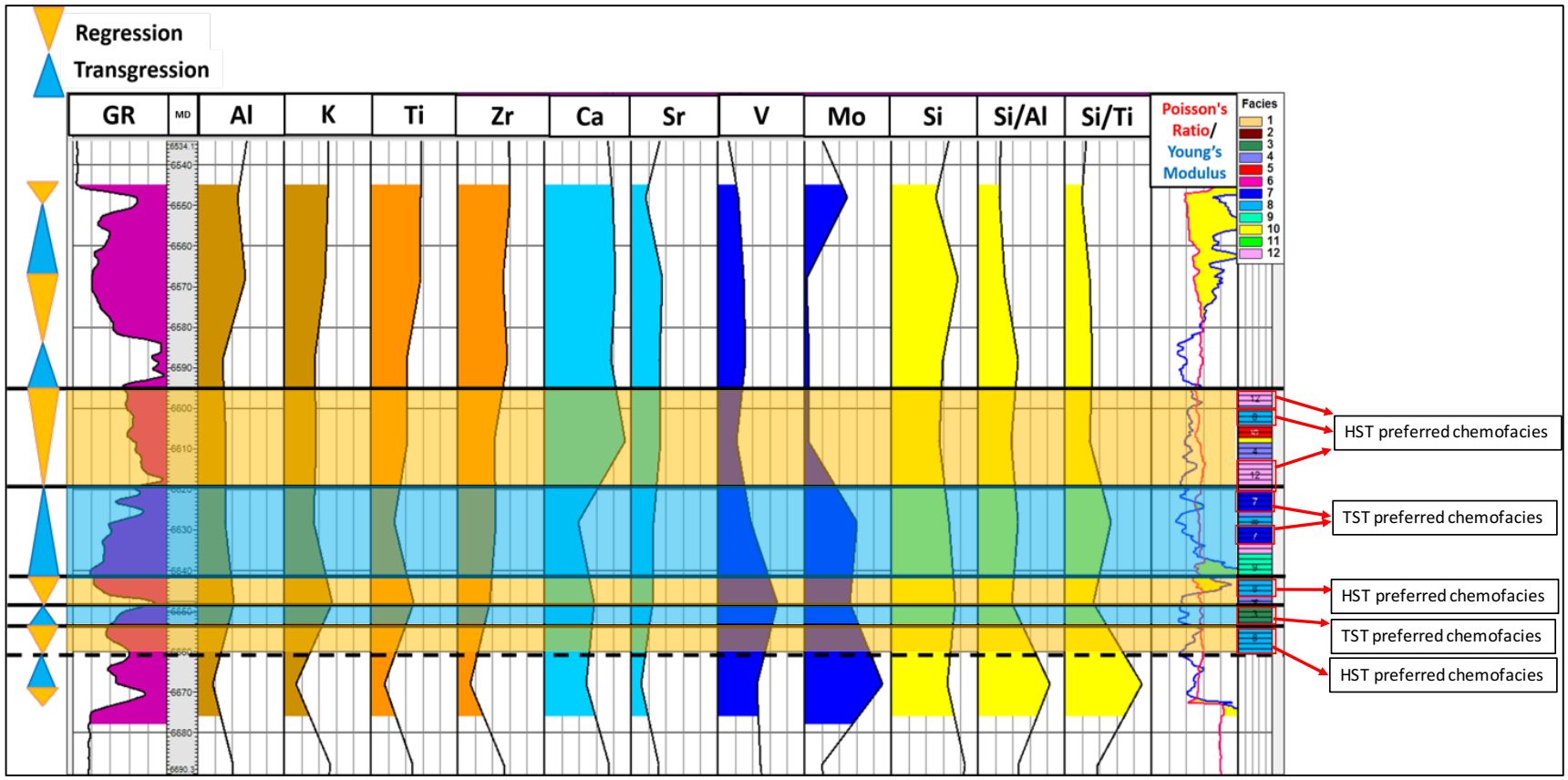

Figure 5.5: The projected vertical chemofacies profile at the H1 well, the chemofacies result matches the sequence stratigraphic framework.

5.3 XRF, XRD and Brittleness Correlation

The shortcoming of the XRF technique is that it can only be able to provide the elemental data. To better characterize the mineral composition and brittleness of the formation, it is necessary to convert the XRF-derived elemental data into the mineral percentages.

This thesis research uses linear regression to correlate XRF data and XRD data. Chapter 4 concluded the minerals in the Woodford Shale mainly are calcite (mainly sample contamination), pyrite, illite, quartz, dolomite and kaolinite. The first step is to check the Pearson correlation factor of all the mineral and element proxies and then pick the high Pearson correlation pairs (Table 5.4). Some other elements which are not environmental proxies are not taken into consideration because it is hard to directly correlate them back to the mineral composition. The samples used here for correlation are the 22 samples from the H2 well, 3 samples from the A1 well, 3 samples from the A2 well and 3 samples from the C1well.

	Calcite	Pyrite	Illite	Quartz	Dolomite	Kaolinite
Si	-0.738305			0.92		
K	-0.839607	0.788991	0.818			
S	-0.839607	0.8575				
Ca	0.849761			-0.8122		
V	-0.808444		0.743489	0.869002		
Th	-0.7777	0.789756				
Mo	-0.905058	0.762897				
Sr	0.890877			-0.814248		
Pb		0.848040				
Al			0.851		-0.7276	
Si/K						0.711141
Si/Ti				0.701757		

Table 5.4: Mineral and elements Pearson correlation factor. The cells highlighted in yellow are considered as high positive or high negative correlation.

Simple linear regression was conducted on the high correlation pairs for nine samples in wells A1, A2 and C1. Since the XRD data from the H2 well was provided by the donor company, in order to keep data consistency, the cross plot only shows the self-measured data points (fig 5.6-fig5.15).

Calcite has regression equations for K, Mo, S and multiple regression with all three elements together. The regression equations and cross plot are as follows in Figure 5.6-5.9. The highest R square regression equation is the multiple linear regression using Mo, K, and S, which is used for future calculations.

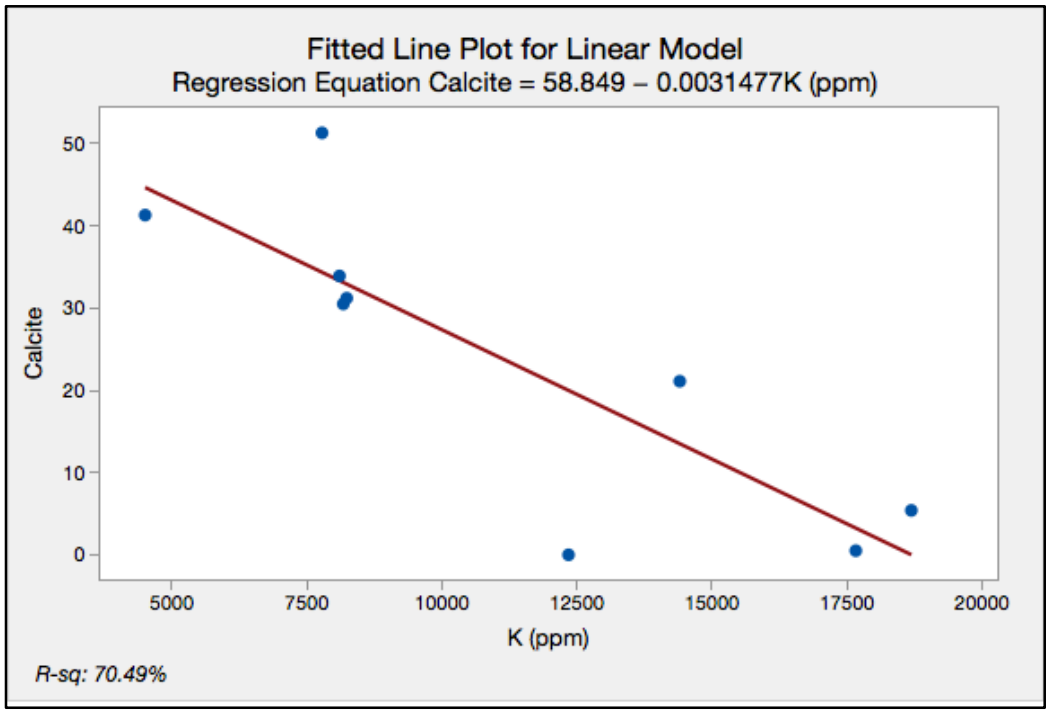

Figure 5.6: Simple linear regression of calcite with K. Equation: Calcite (%) = 58.849-0.0031477K (ppm).

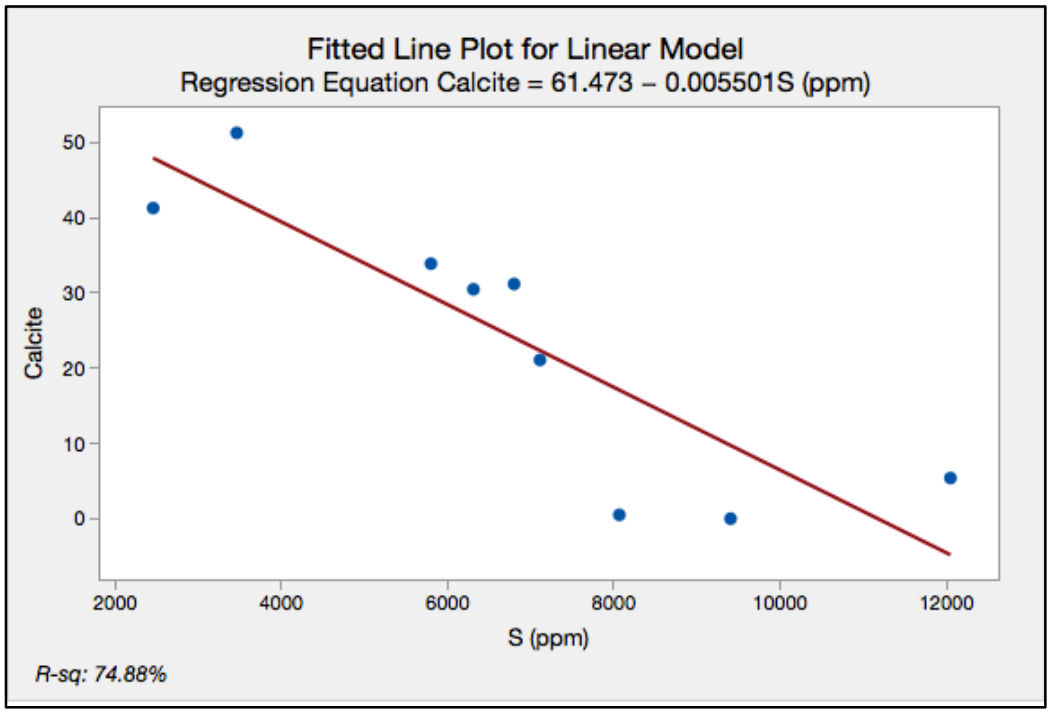

Figure 5.7: Simple linear regression of calcite with S Equation: Calcite (%) = 61.473-0.005501S (ppm).

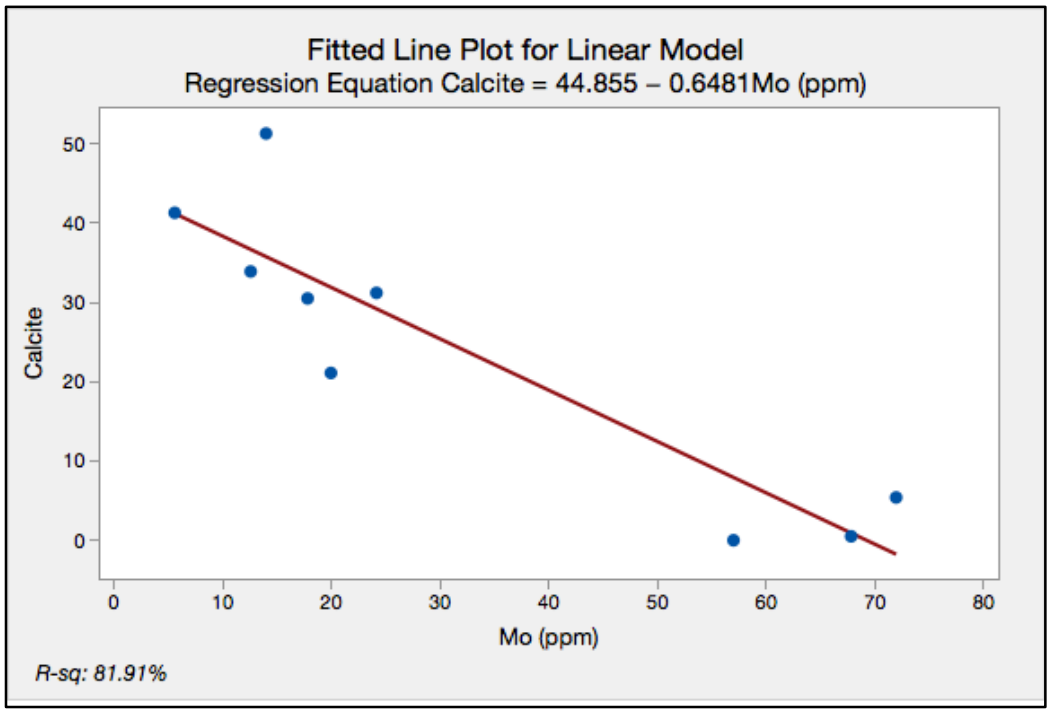

Figure 5.8: Simple linear regression of the calcite with Mo. Equation: Calcite (%) = 44.855-0.6481Mo (ppm).

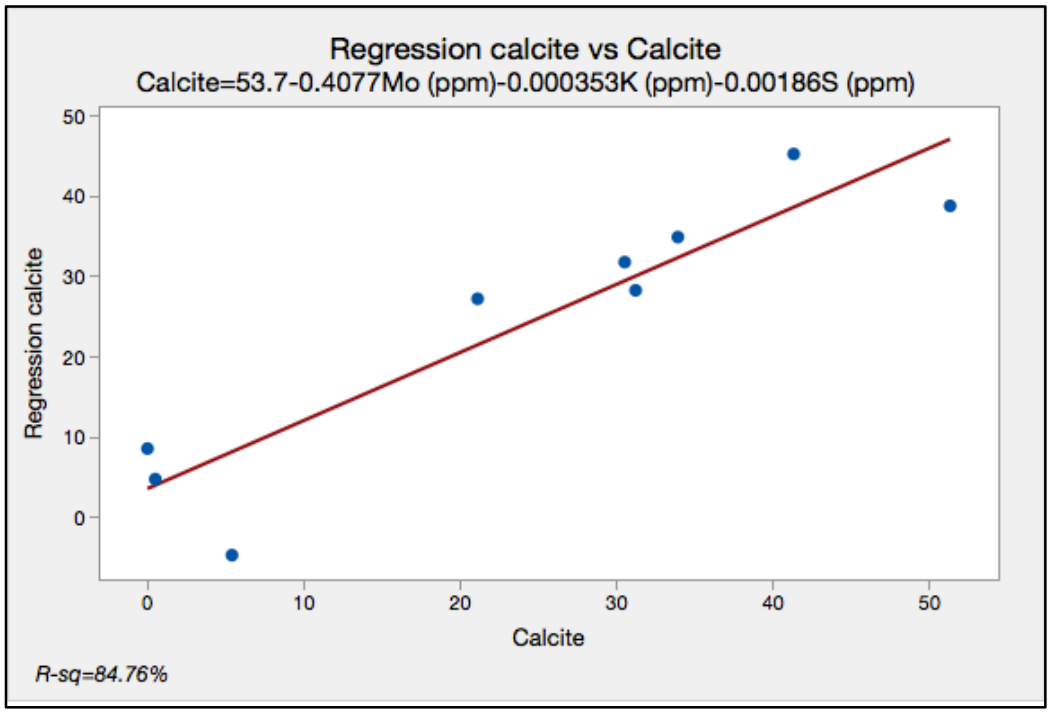

Figure 5.9: Multiple linear regression of calcite with Mo, K and S. Equation: Calcite (%) = 53.7-0.4077Mo (ppm)-0.000353K (ppm)-0.00186S (ppm).

Quartz has a simple linear regression equation using Si and multiple regression with Si and Si/Ti together. The regression equations and cross plot are as follows in Figure 5.10-5.11. The highest R square regression equation is the multiple linear regression using Si and Si/Ti. It is used for future calculation.

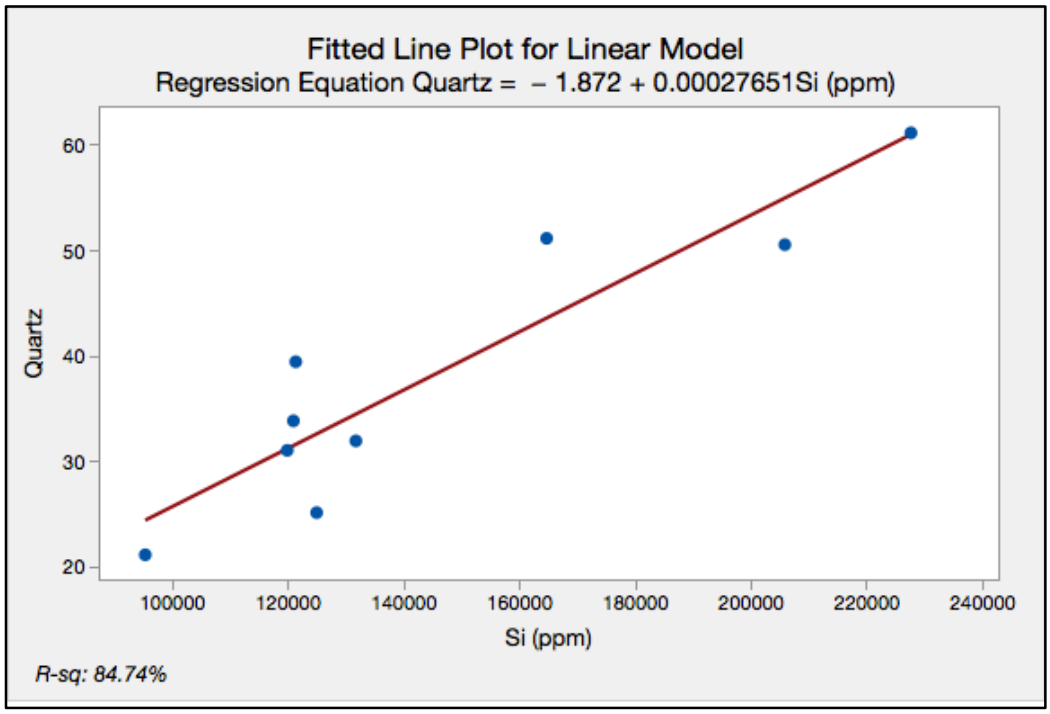

Figure 5.10: Simple linear regression of the quartz with Si. Equation: Quartz (%) =-1.872+0.00027651 Si(ppm).

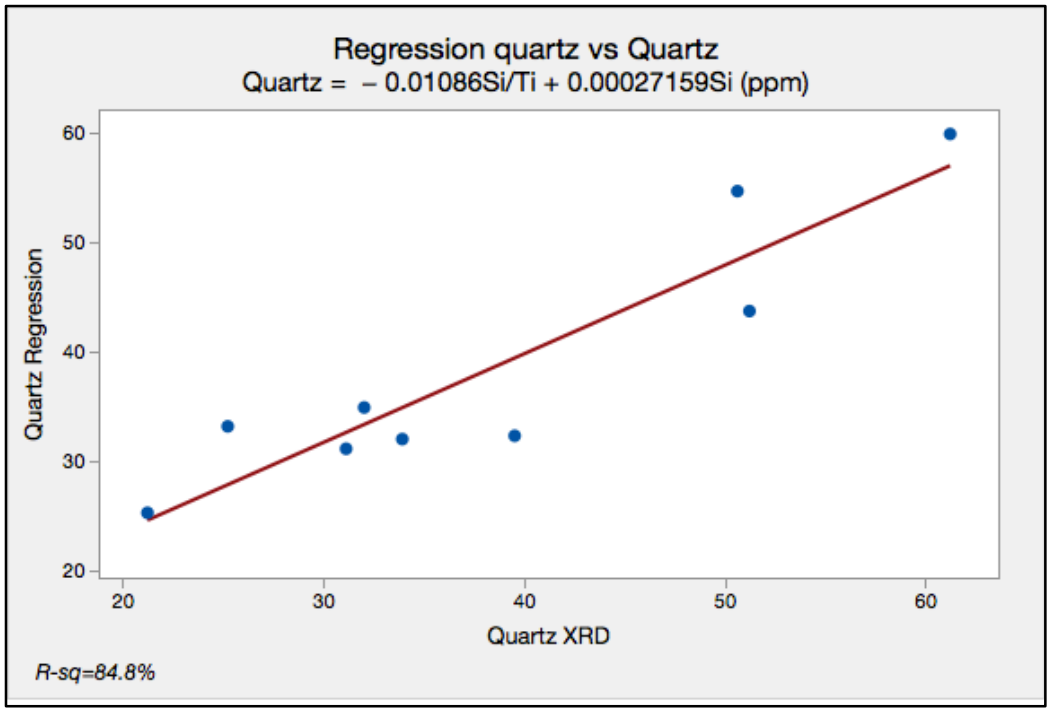

Figure 5.11: Multiple linear regression of the quartz with Si and Si/Ti. Equation: Quartz (%) = -0.01086Si/Ti + 0.00027159Si (ppm).

Pyrite simply used S to run the simple linear regression as below in Figure 5.12:

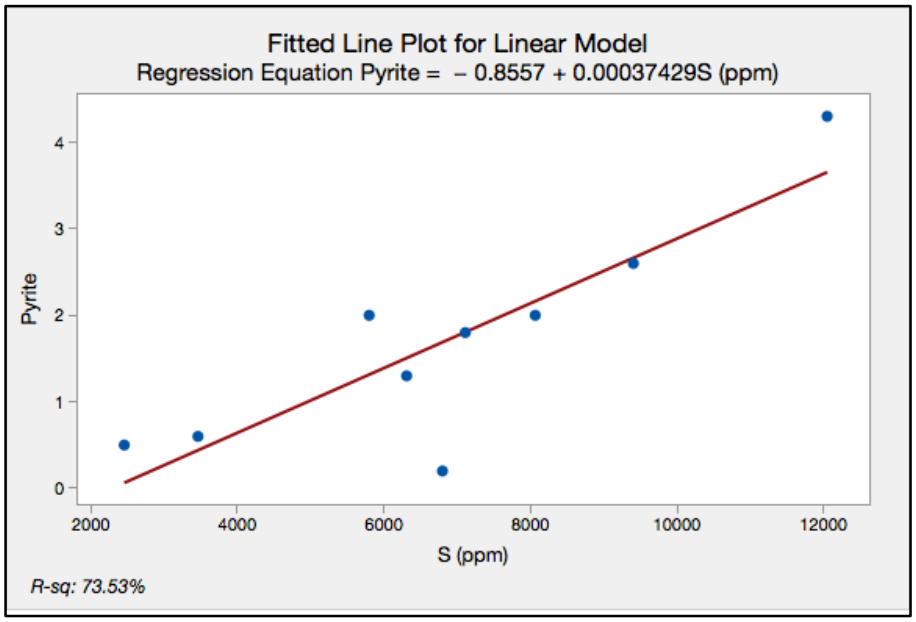

Figure 5.12: Simple linear regression of the pyrite with S. Equation: Pyrite (%) = -0.8557+0.00037429 S(ppm).

Dolomite does not have a very high correlation with any of the proxy elements. The regression of dolomite only used Al which has a negative correlation. The equation of regression and cross plot is as follows in Figure 5.13:

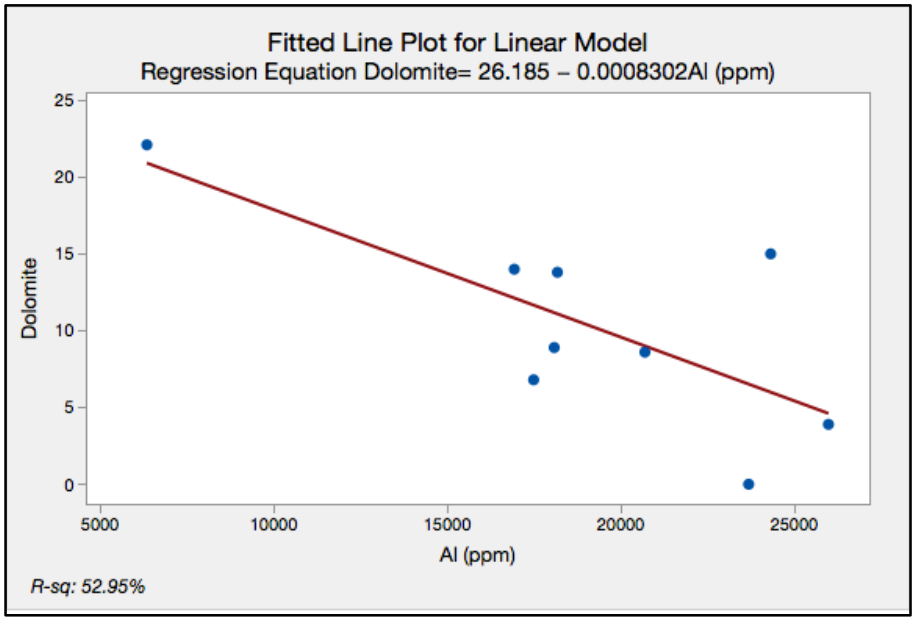

Figure 5.13: Simple linear regression of the dolomite with Al. equation: Dolomite (%)=26.185-0.0008302 Al (ppm).

For regression of Illite using multiple linear regression with K and Al, the equation and cross plot are as follows in Figure 5.14.

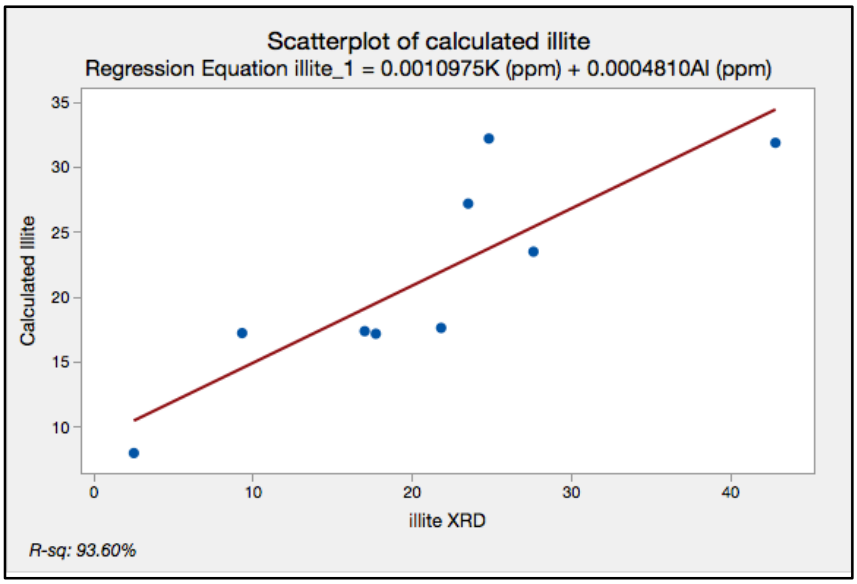

Figure 5.14: Multiple linear regression for illite with K and Al as two main elements. Equation: Illite (%) =0.0010975 K (ppm)+ 0.000481 Al (ppm).

Kaolinite uses Si/K ratio for a simple linear regression, the R-sq number is not as optimistic as the other elements' regressions. The equation and cross plot are as follows in Figure 5.15.

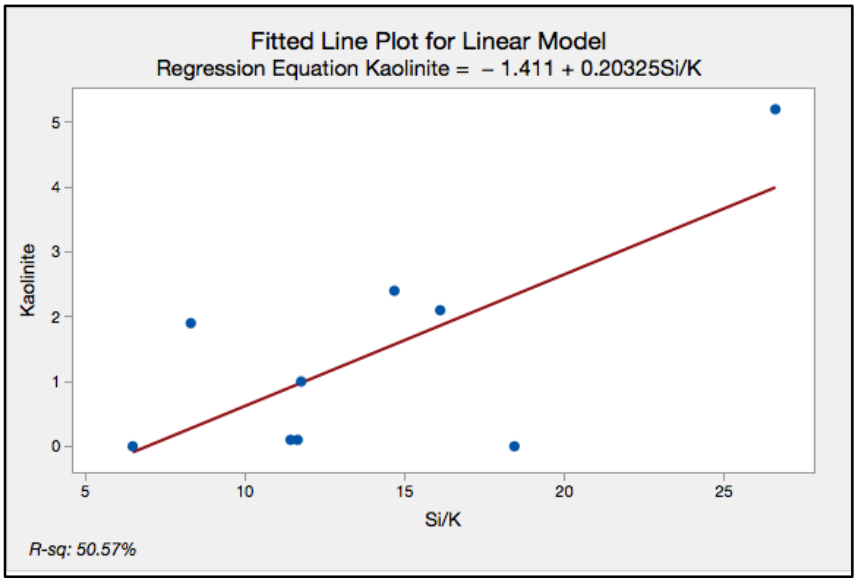

Figure 5.15: Simple linear regression for kaolinite with Si/K. Equation: Kaolinite=-1.411+0.20325Si/K.

The main goal of this exercise was to calculate the formation brittleness from the XRF data, which typically is calculated by the mineral percentage. This research compared four different methods of calculation to estimate the brittleness from XRF data.

The first method is to obtain the brittleness from the XRD data using the equation firstly proposed by Wang and Gale (2009) and revised by Jin et al., (2015):

$$BI_{Jin\ (2015)} = \frac{Qz + Dol + Cal}{Qz + Dol + Cal + Cly + TOC}$$

A1, A2, C1 and H2 wells have 29 samples. The elements are all cross plotted with the brittleness index; the highly related elements are Al, Ti, Sr, K, Mo, V, Si/K, Si/Al and Si/Ti (Figure 5.16). Multiple linear regression with these elements provided a very high R square value of 85.35% (Figure 5.17). The equation is:

BI = 0.00002854 Al (ppm) − 0.00002313 K (ppm) − 0.0000032 Ti (ppm)

+ 0.0003157 Mo (ppm) + 0.0004109 Sr (ppm) + 0.05328 Si/Al

− 0.001144 Si/Ti − 0.00556 Si/K

The shortcoming of this regression method is that some element factors do not make geologic sense, for example: Al, the clay and feldspar proxy has a positive factor for the BI calculation. Mo typically exists in clays but has a positive factor for the BI calculation. Si/K, the quartz content proxy, has negative factor for BI calculation. Even though the correlation result is optimistic, it might not apply universally due to the pure statistic calculation.

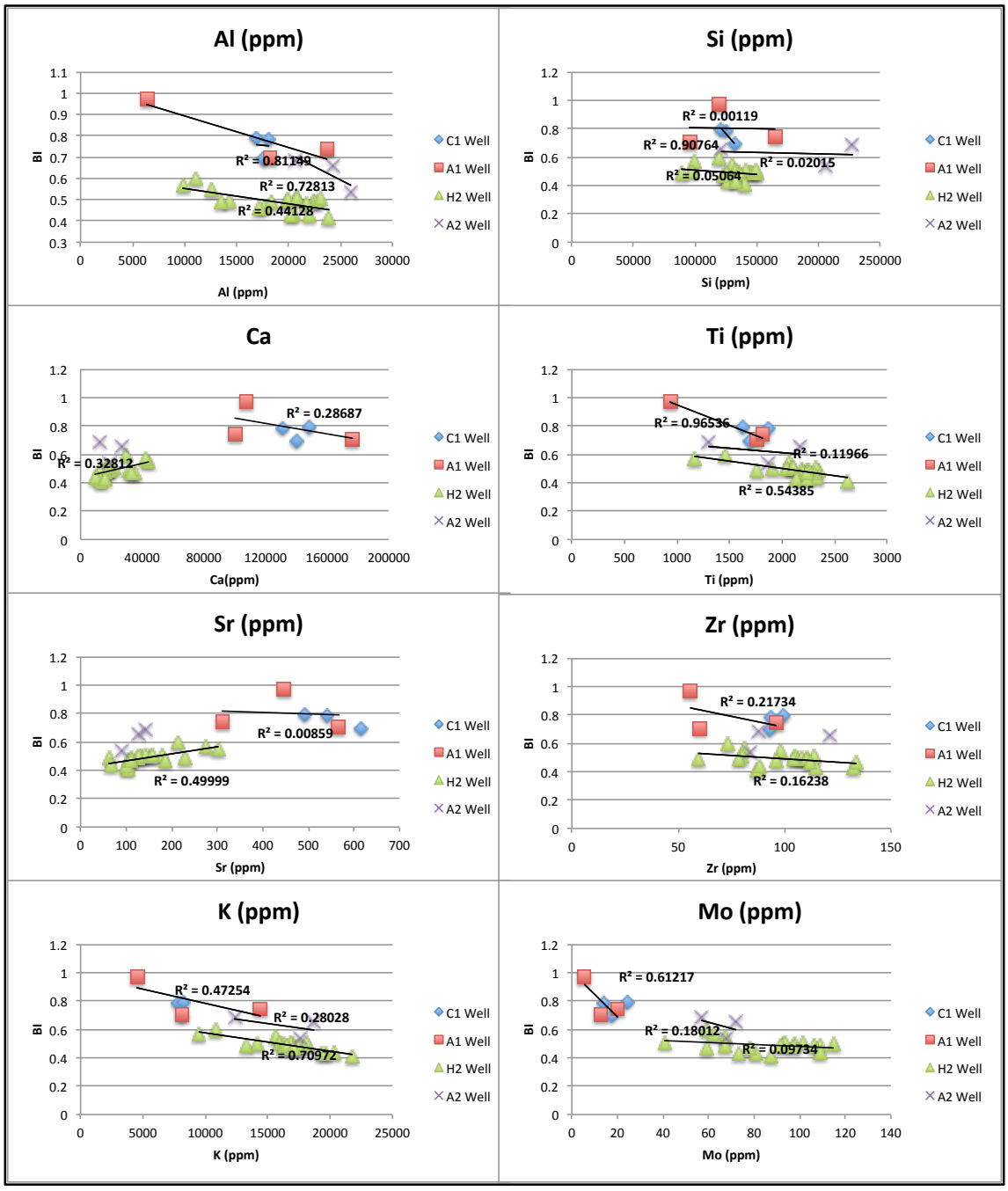

Figure 5.16 (Part A): Elements correlated with XRD data measured brittleness index. The Al, Ti, Sr, K and Mo have higher correlation than the other elements

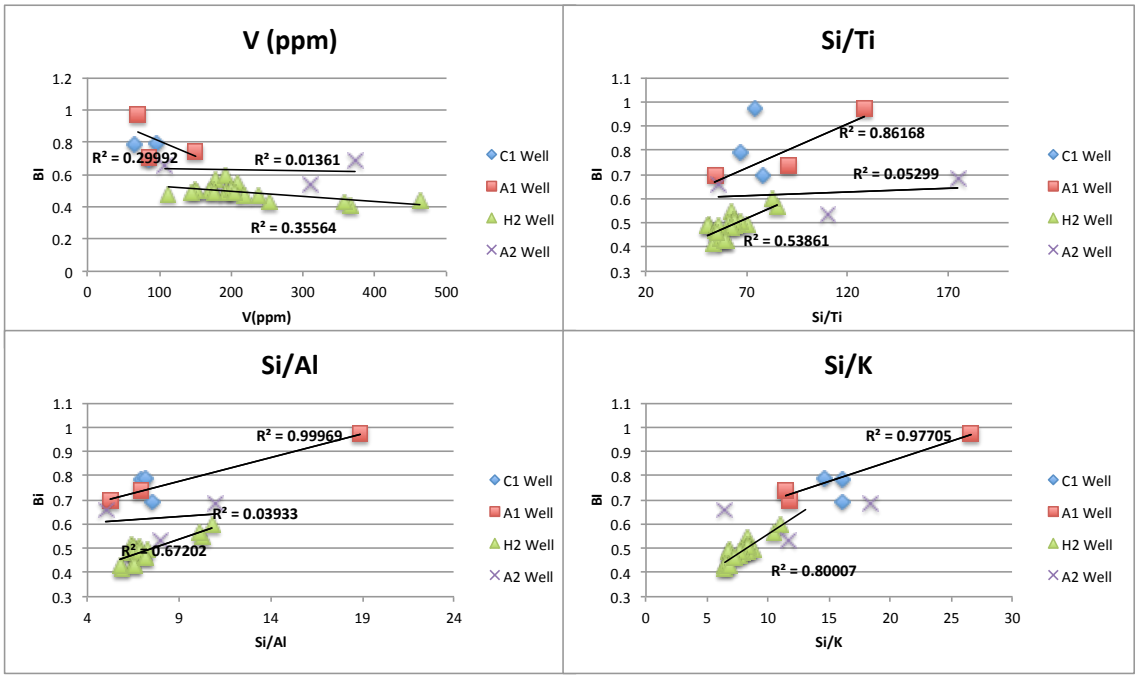

Figure 5.16 (Part B): Elements correlated with XRD data measured brittleness index. V, Si/K, Si/Al and Si/Ti have higher correlation than the other elements.

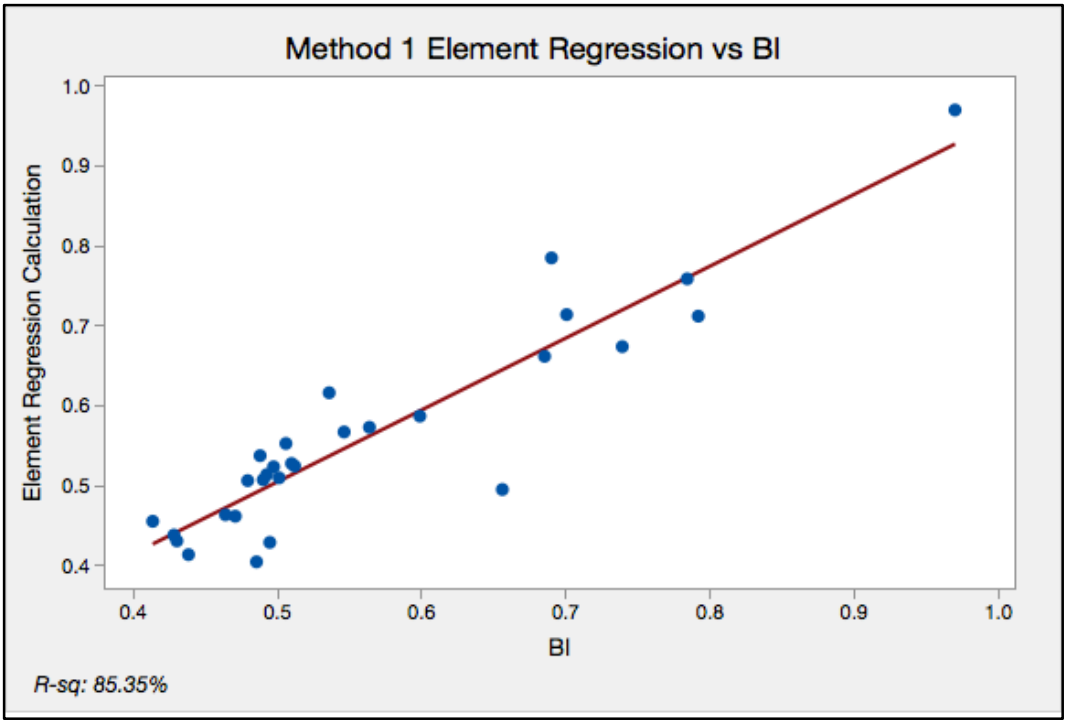

Figure 5.17: Multiple linear regression of related elements with BI; the correlation is high for the overall regression.

The second method directly uses the results of the XRF to XRD linear regression equations and brittleness calculation equation of Jin et al., (2015). The TOC weight percentage is also re-calculated to fit within the 100 weight percentage.

$$BI_{Jin\ (2015)} = \frac{Qz + Dol + Cal}{Qz + Dol + Cal + Cly + TOC}$$

Quartz = −0.01086 Si/Ti + 0.00027159 Si (ppm) + Dolomite = 26.185 − 0.0008302 Al (ppm) + Calcite = 53.70 − 0.4077 Mo (ppm) − 0.000353 K (ppm) − 0.001860 S (ppm)

Quartz = −0.01086 Si/Ti + 0.00027159 Si (ppm) + Illite = 0.0010975 K (ppm) + 0.0004810 Al (ppm) + Kaolinite = −1.411 + 0.20325 Si/K + Calcite = 53.70 − 0.4077 Mo (ppm) − 0.000353 K (ppm) − 0.001860 S (ppm) + Dolomite = 26.185 − 0.0008302 Al (ppm) + TOC

The calculation results have a lower correlation of 57.28% R-sq than the first method (Figure 5.18). The reason of this is each regression has some error, especially for the dolomite and kaolinite with low correlation coefficient. This will increase the error for the overall calculation.

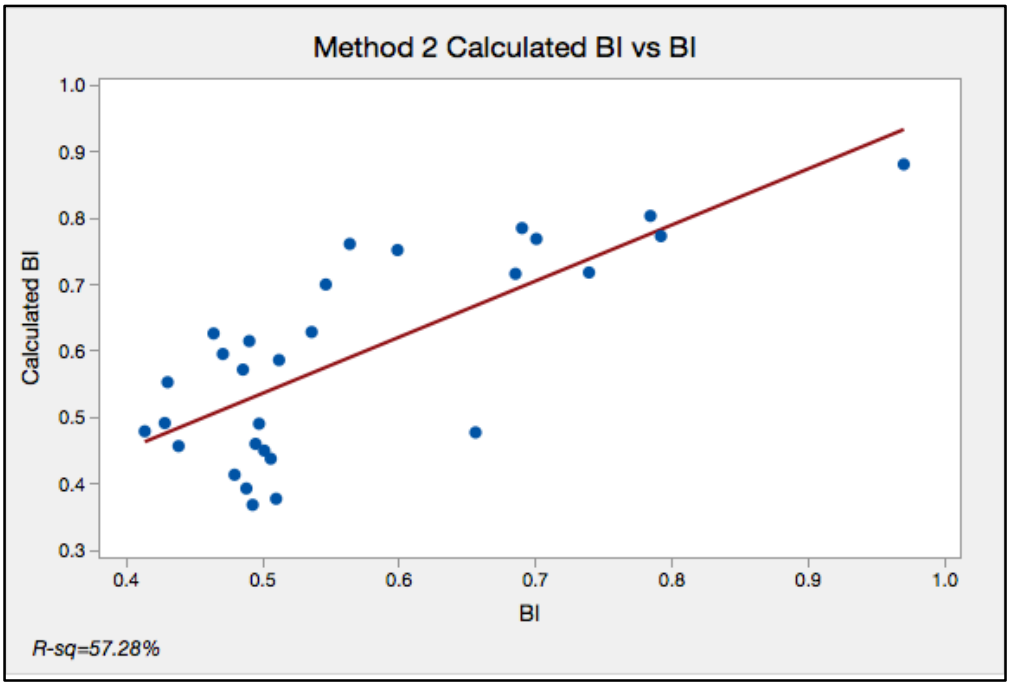

Figure 5.18: Brittleness Index formula calculated result with the real data; the correlation factor is lower than method 1 due to cumulative mineral regression error.

The third method is based on the elements' weight percentage in the mineral to calculate the brittleness index. Even though the chemical formula of the same mineral can be different, for calculation convenience, here the general formulas used are:

Illite: $(K,H_3O)(Al,Mg,Fe)_2(Si,Al)_4O_{10}[(OH)_2,(H_2O)]$

Molecular Weight = 389.34 gm

Potassium	6.03 % K	7.26 % K_2O
Magnesium	1.87 % Mg	3.11 % MgO
Aluminum	9.01 % Al	17.02 % Al_2O_3
Iron	1.43 % Fe	1.85 % FeO
Silicon	25.25 % Si	54.01 % SiO_2
Hydrogen	1.35 % H	12.03 % H_2O
Oxygen	55.06 % O	

Quartz: SiO_2

Molecular Weight = 60.08 gm

Silicon	46.74 % Si	100.00 % SiO2
Oxygen	53.26 % O	

Dolomite: $CaMg(CO_3)_2$

Molecular Weight = 184.40 gm

Calcium	21.73 % Ca	30.41 % CaO
Magnesium	13.18 % Mg	21.86 % MgO
Carbon	13.03 % C	47.73 % CO2
Oxygen	52.06 % O	

Calcite: $CaCO_3$

Molecular Weight = 100.09 gm

Calcium	40.04 % Ca	56.03 % CaO
Carbon	12.00 % C	43.97 % CO2
Oxygen	47.96 % O	

Kaolinite: $Al_2Si_2O_5(OH)_4$

Molecular Weight = 258.16 gm

Aluminum	20.90 % Al	39.50 % Al2O3
Silicon	21.76 % Si	46.55 % SiO2
Hydrogen	1.56 % H	13.96 % H2O
Oxygen	55.78 % O	

Assume that in one sample, the illite weight percentage is A, quartz weight percentage is B, dolomite weight percentage is C, calcite weight percentage is D. kaolinite weight percentage is E. The resulting equation set is:

A+B+C+D+E+TOC=100

BI=(B+C+D)/(A+B+C+D+E+TOC)

K(ppm)=10^6*A*0.000603

Al(ppm)=10^6*(A*0.000901+E*0.00209)

Si(ppm)=10^6*(A*0.002525+B*0.004674+E*0.002176)

Ca(ppm)=10^6*(D*0.002173+C*0.004004)

Each sample has a solution for converting to mineral percentage and then for brittleness calculation. The calculation formula is the same as the second method, but the correlation factor is much higher which means the third method is a feasible way to calculate the formation brittleness (Figure 5.19).

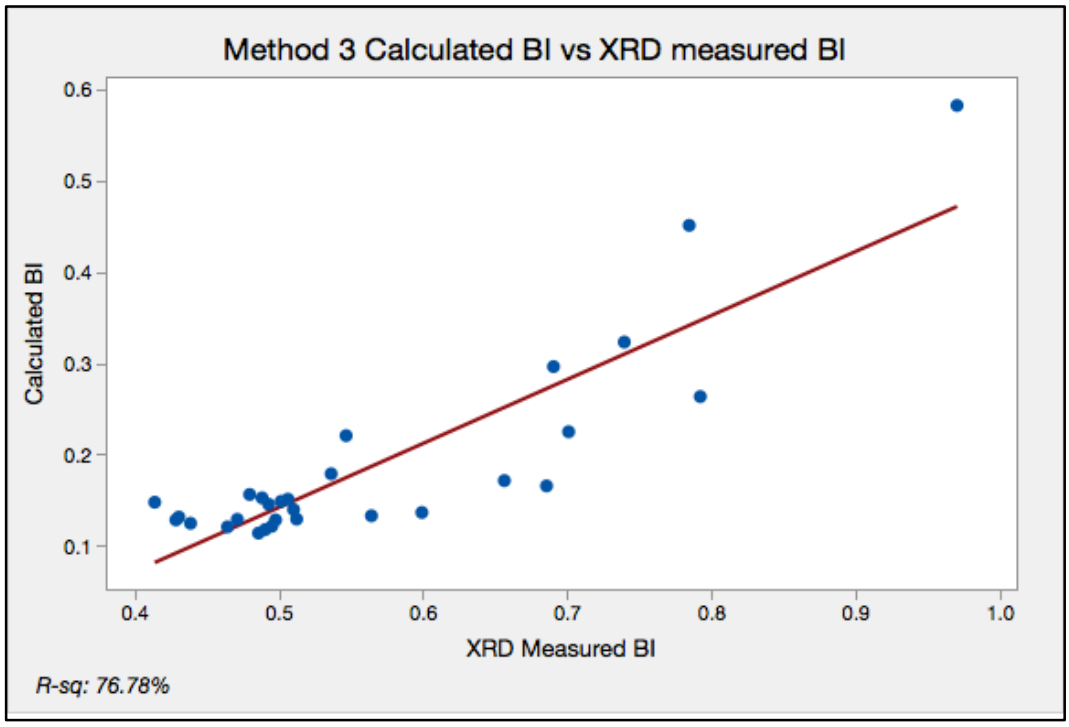

Figure 5.19: Method 3 calculated brittleness and XRD data calculated brittleness. The correlation is high compared to the method 2.

The fourth method only uses the H2 well data for the purpose of consistency. As the chemofacies for the H2 well are defined and interpreted, plotting the brittleness of different chemofacies as Figure 5.20. In the figure, each chemofacies has a certain range of brittleness. For example, the facies 12 and facies 10 were defined as HST preferred, with more brittle facies. The brittleness average range is higher than the facies 8 and 6 which is TST preferred. Facies 3 as a single point might be an error point with higher brittleness index value. Thus the chemofacies method can provide a range of brittleness for estimation.

Overall, the method three and the method four can be used together to estimate the brittleness within the formation or certain part along the horizontal wellbore. These methods also benefit the future research since the XRF is a cheaper and faster technique than the XRD technique.

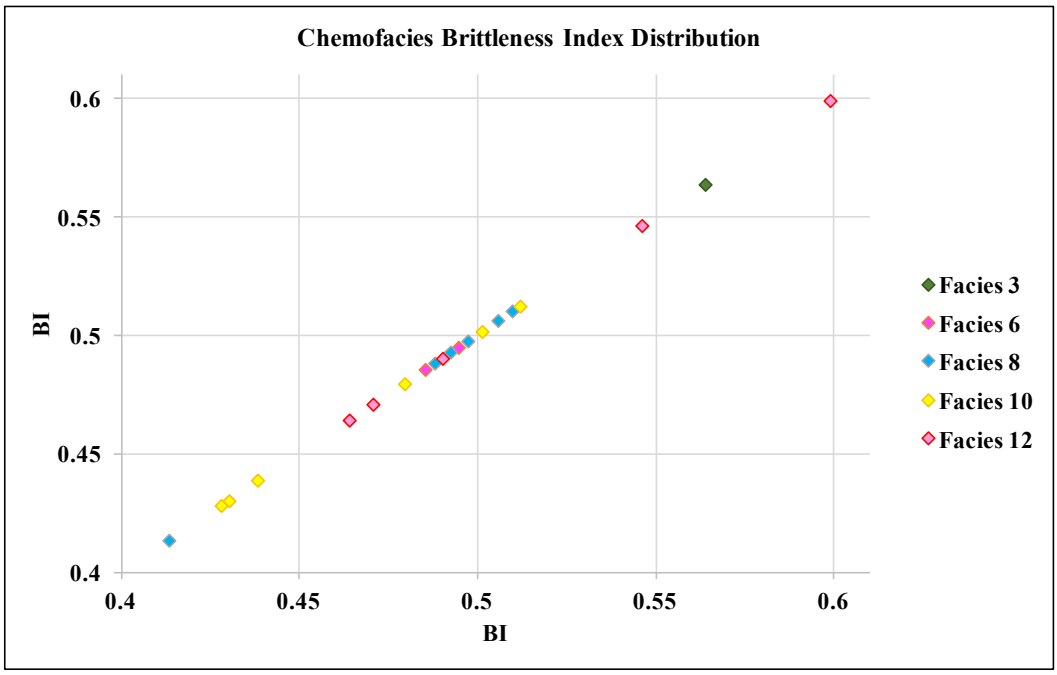

Figure 5.20: Brittleness index distribution with different chemofacies, for the chemofacies interpreted as highstand system tract which have a higher range of brittleness than the chemofacies interpreted as transgressive system tract preferred.

Chapter 6: Source Rock Potential

16 cutting samples from the A1, A2, C1 and H2 wells were selected by the author and measured by the Geomark Research. LTD. Three were from the A1 well, six from the A2 well, four from the C1 well and three from the H2 well respectively. Selecting the depths of sampling is based on the Woodford depth range and well type. There were an additional 21 samples with Rock-Eval data from the H2 well provided by Longfellow Energy and the measurements were conducted by Weatherford geochemistry lab.

The Rock-Eval lab results can provide parameters that are used to evaluate the source rock potential, such as organic matter type, richness and maturity. The procedure of Rock-Eval 6 is described by Lagargue et al. (1998) and Behar et al. (2001). It is the technique to conduct pyrolysis on rock samples, in other words "heat" the sample. The first preparation step is to pulverize and acidize the sample to remove the carbon associated with the carbonate and other contaminations, then the sample is combusted in a helium- or nitrogen- filled chamber to crack the kerogen and measure the converted CO and CO_2. The temperature of combustion has a gradient of increase with 25^{o}C/min up to 300℃, then stay with 300 ℃ until no more gas is generated. Then the temperature is raised at the same gradient to 850 ℃, and then is dropped down to the room temperature. The flame ionization detector (FID) detects the organic compounds extracted during the heating process which indicates the amount of organic matter decomposed from the sample; the diagram shows the time and organic matter extracted as a pyrogram (Espitalié and Bodenave, 1992) On the pyrogram there are three to four observable peaks associated with different S1, S2, S3 and S4 temperature, respectively.

S1 occurs at 300℃, when the free oil and gas generated in the subsurface are extracted. The S2 peak appears during the second heating stage as a result of cracking the kerogen within the sample, which represents the potential hydrocarbon production still in the source rock. This peak temperature is called T_{max}. For this research vitrinite reflectance is not available, so T_{max} used for maturity estimation: the higher the T_{max}, the higher maturity is of the sample (Barker and Pawlewicz, 1986; Espitalié, 1986). The S3 peak represents the carbon dioxide generated during cracking of the remaining kerogen. The S4 peak indicates the residual carbon from the dead oil. A pyrogram is shown in Figure 6.1. All peaks use the unit of mg per gram of rock (Tissot and Welte, 1984). Some important indices are calculated based on the basic parameters obtained from pyrolysis. Hydrogen index: HI=100*S2/TOC, is used for indicating the hydrogen amount in the kerogen. The oxygen index: OI=100*S3/TOC, is related to the oxygen amount in the kerogen. The production index: PI=S1/(S1+S2), represents the maturity and production potential. The higher the maturity of the source rock, the higher the PI value. These indices are used to evaluate the kerogen type and maturation (Tissot and Welte, 1984).

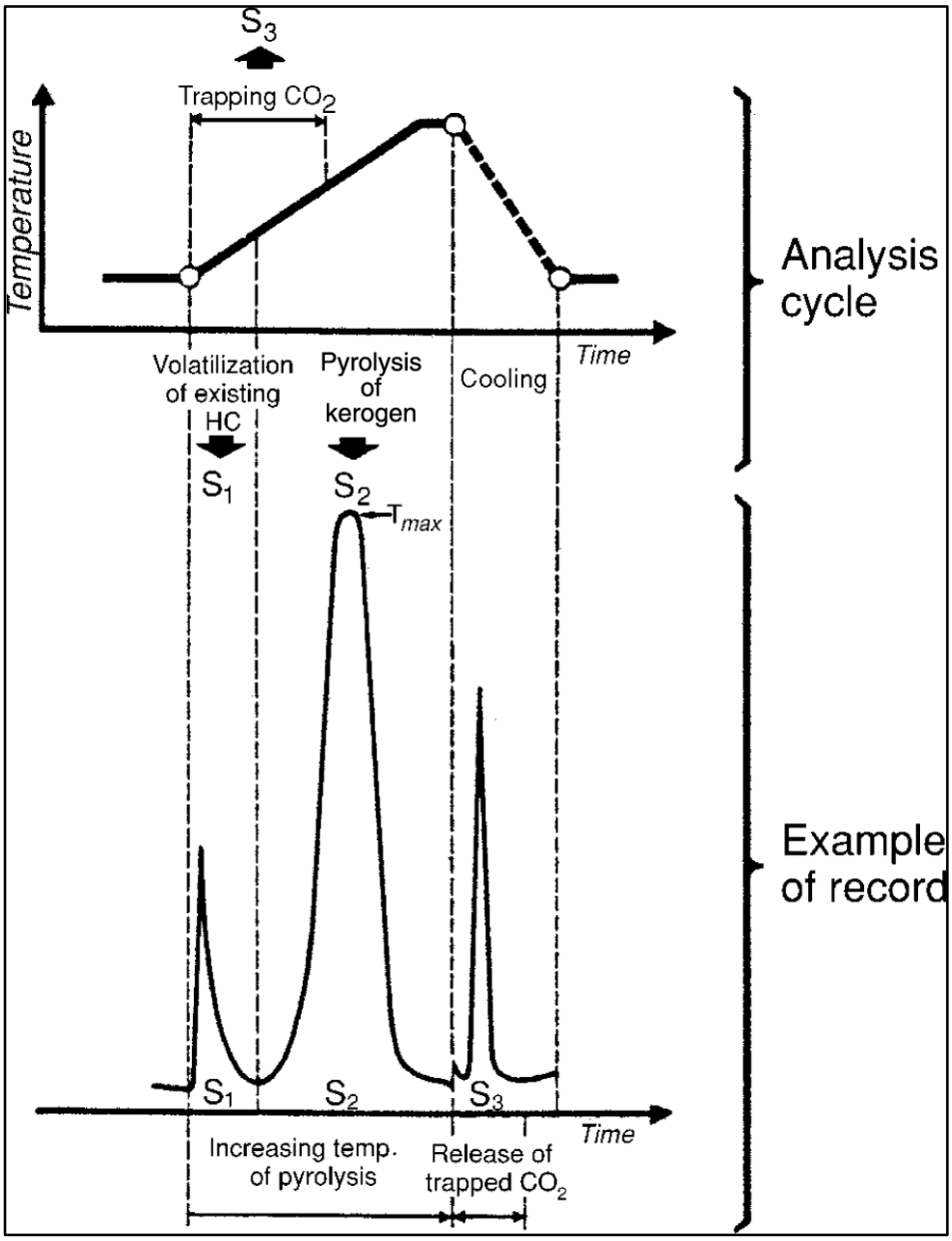

Figure 6.1: Pyrolysis temperature gradient and peaks of oil extraction from pyrogram. The pyrogram does not include all the peaks but the three main peaks used for resource shale evaluation are shown (Tissot and Welte, 1984).

This research was aimed to obtain an estimation of organic compounds from different depths. Table 6.2 shows the summary of the Rock-Eval analyse results from the four wells. The TOC values vary by the depths and wells. The TOC of A1 and C1 wells is low in S2 peaks, which is mainly caused by sample contamination because most of the samples were blended with carbonates from the Mississippian Lime due to

the large sampling interval. A2 and H2 have more reliable data because they both are horizontal wells with lesser true vertical sampling interval which leads to less sample blending and contamination. According to Jarvie (1991), the TOC value can be used directly to estimate the kerogen quality as shown in Table 6.1. Most of the samples show the Woodford has good to very good or even excellent quality in some portions. The average T_{max} value is about 445 ℃, which indicates the Woodford Shale is in the oil window.

(a)

Generation Potential	TOC in Shales (wt. %)	TOC in Carbonates (wt. %)
Poor	0.0–0.5	0.0–0.2
Fair	0.5–1.0	0.2–0.5
Good	1.0–2.0	0.5–1.0
Very good	2.0–5.0	1.0–2.0
Excellent	>5.0	>2.0

(b)

	TOC (wt. %)
Inadequate	0.0–0.5
Marginal	0.5–1.0
Adequate	>1.0

Table 6.1: Kerogen quality interpretation based on the TOC value (Jarvie, 1991).

Well	Sample	Depth (MD)	Leco TOC	Tmax	S1	S2	S3	HI	OI	PI	Note
A1	1	6695	2.45	441	0.35	3.2	0.42	130.61	17.14	0.10	Self Measured
	2	6726	0.333	0	0.02	0.19	0.22	57.06	66.07	0.10	Self Measured
	3	6758	1.97	443	0.26	2.18	0.4	110.66	20.30	0.11	Self Measured
A2	1	7130	4.68	446	2.64	10.08	0.52	215.38	11.11	0.21	Self Measured
	2	7160	4.48	445	2.84	10.77	0.44	240.40	9.82	0.21	Self Measured
	3	7190	4.55	443	2.76	9.08	0.47	199.56	10.33	0.23	Self Measured
	4	7220	4.64	443	3.31	11.21	0.38	241.59	8.19	0.23	Self Measured
	5	7250	4.28	445	2.89	10.39	0.39	242.76	9.11	0.22	Self Measured
	6	7280	4.52	442	2.88	9.91	0.44	219.25	9.73	0.23	Self Measured
C1	1	6680	0.748	444	0.44	1	0.41	133.69	54.81	0.31	Self Measured
	2	6710	1.7	442	0.94	2.67	0.48	157.06	28.24	0.26	Self Measured
	3	6740	2.05	444	1.05	3.54	0.45	172.68	21.95	0.23	Self Measured
	4	6770	2.19	442	1	4.05	0.39	184.93	17.81	0.20	Self Measured
H2	1	6820	2.55	441	1.35	6.92	0.62	271.37	24.31	0.16	Provided
	2	6840	3.01	442	0.82	3.3	0.81	109.63	26.91	0.20	Provided
	3	6860	3.5	448	1.42	11.08	0.34	316.57	9.71	0.11	Provided
	4	6880	3.76	442	0.75	4.9	0.7	130.32	18.62	0.13	Provided
	5	6900	5.545	439	1.11	7.33	1.01	132.19	18.21	0.13	Provided
	6	6920	6.27	444	2.95	20.78	0.32	331.42	5.10	0.12	Provided
	7	6940	6.02	444	2.96	20.76	0.29	344.85	4.82	0.12	Provided
	8	6960	5.44	441	1.63	14.64	0.74	269.12	13.60	0.10	Provided
	9	6980	6.1	443	2.84	20.57	0.29	337.21	4.75	0.12	Provided
	10	7000	5.775	444	2.91	19.22	0.33	332.81	5.71	0.13	Provided
	11	7040	5.62	443	2.65	18.22	0.37	324.20	6.58	0.13	Provided
	12	7080	5.685	441	1.76	14.5	0.66	255.06	11.61	0.11	Provided
	13	7120	5.24	439	1.27	13.35	0.59	254.77	11.26	0.09	Provided
	14	7160	5.135	444	2.8	16.63	0.33	323.86	6.43	0.14	Provided
	15	7240	6.09	444	1.15	3.58	1.3	58.78	21.35	0.24	Provided
	16	7280	6.43	439	1.2	5.78	1.29	89.89	20.06	0.17	Provided
	17	7320	7.105	450	3.66	23.34	0.25	328.50	3.52	0.14	Provided
	18	7360	6.2	447	2.86	20.48	0.32	330.32	5.16	0.12	Provided
	19	7400	5.83	445	2.52	16.91	1.22	290.05	20.93	0.13	Provided
	20	7440	6.22	446	3.23	19.35	0.84	311.09	13.50	0.14	Provided
	21	7480	6.14	447	3.74	19.41	0.64	316.12	10.42	0.16	Provided
	22	7920	10.6	443	3.01	28.8	0.98	271.70	9.25	0.09	Self Measured
	23	8800	10.9	445	4.37	35.25	1.09	323.39	10.00	0.11	Self Measured
	24	8840	10.5	443	3.84	33.01	1.07	314.38	10.19	0.10	Self Measured

Table 6.2: Rock-Eval analysis of all four wells cutting samples, A1 and C1 well data is not very reliable due to the sample contamination A2 and H2 wells data are more reliable.

The TOC value of the A1 well and data location is shown in Figure 6.2. There are only three sampling points throughout the Woodford Shale, and the top one is partially blended with carbonate from the upper formation. The three data points have TOC values of 2.45, 0.3, and 1.97 from top to bottom. The TOC value can be rated as good quality kerogen except for the second point, which is considered as a contaminated sample from the XRD data: 41.2% of carbonate lowers the TOC concentration. The evaluation results also confirmed by pyrograms of these three samples is shown in Figure 6.3 that the second point merely has the S2 peak, which means the sample is organic matter lean due to sample contamination.

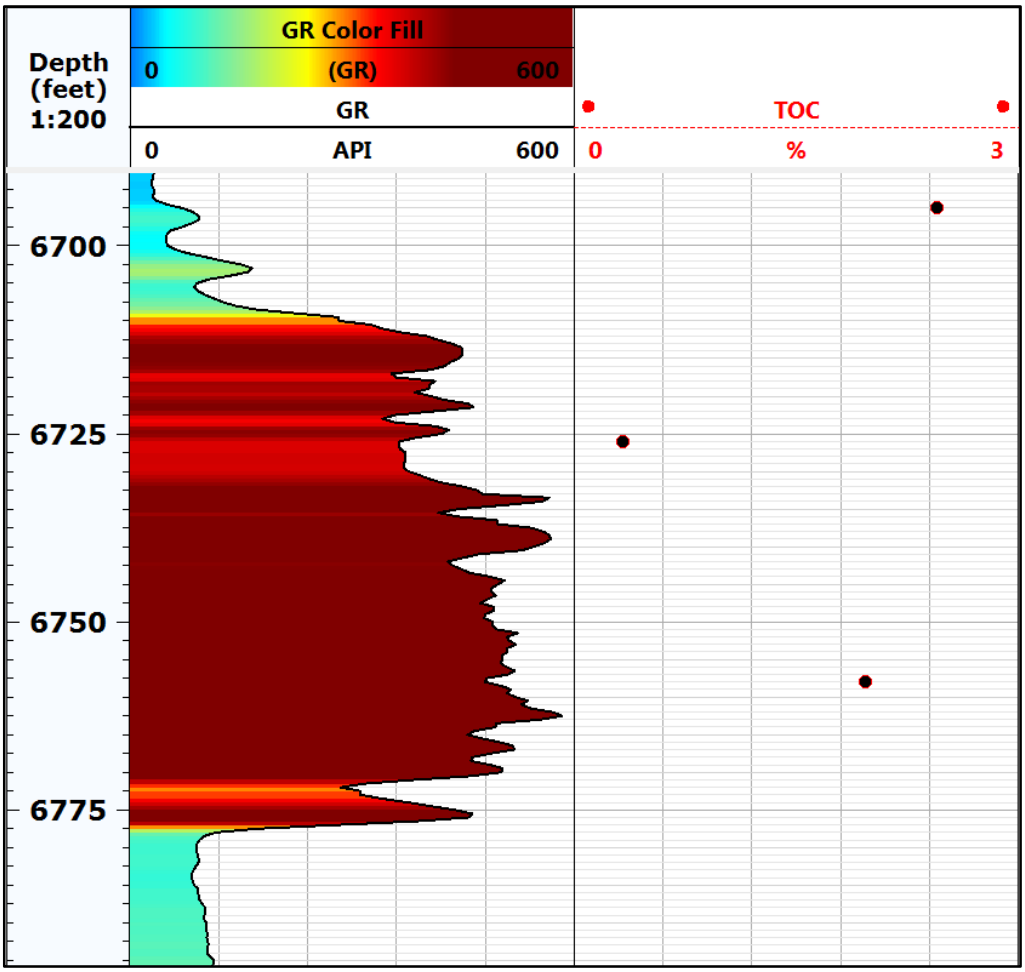

Figure 6.2: Rock-Eval sampling points along the A1 well, the upper sample is almost out of the Woodford Shale and only three samples are shown throughout the Woodford Shale.

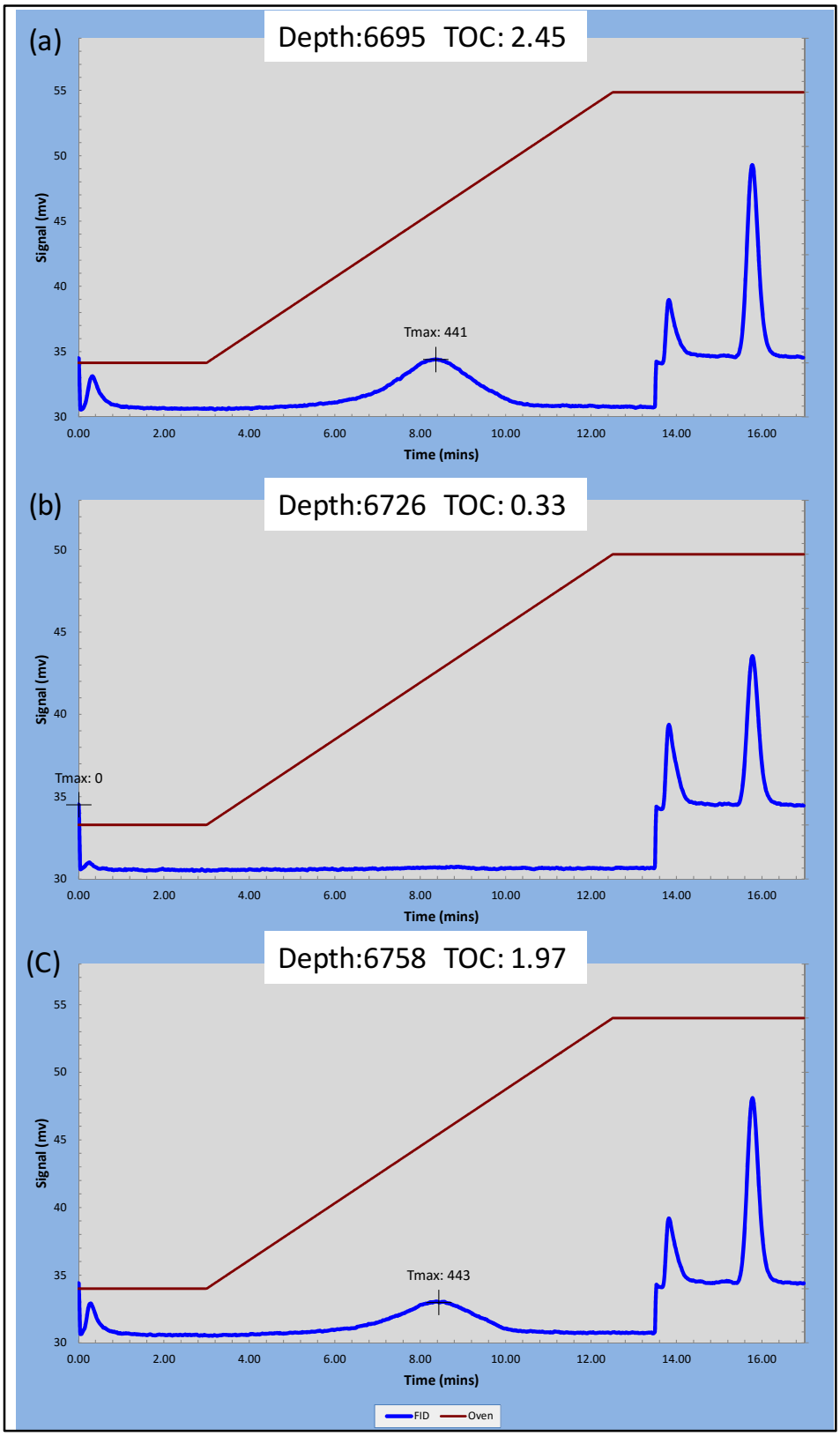

Figure 6.3: Pyrograms of three samples from the A1 well, the low S1 and S2 peaks reveals low oil generation potential due to sample contamination.

The A2 well has six depths of Rock-Eval data through the Woodford Shale (Figure 6.4). Since the A2 well is a horizontal well, sample selection stops at the fully landed measured depth. The average TOC of 4.5% is rated as very good source rock. Since the pyrograms of these six samples are similar, only the bottom second one is shown in Figure 6.5. From the pyrogram, S1 and S2 peaks are both higher than the A1 well because the A2 well sample is less contaminated by the upper formation. High S1 and S2 peaks indicate that the samples contain the hydrocarbon and optimistic oil generation potential.

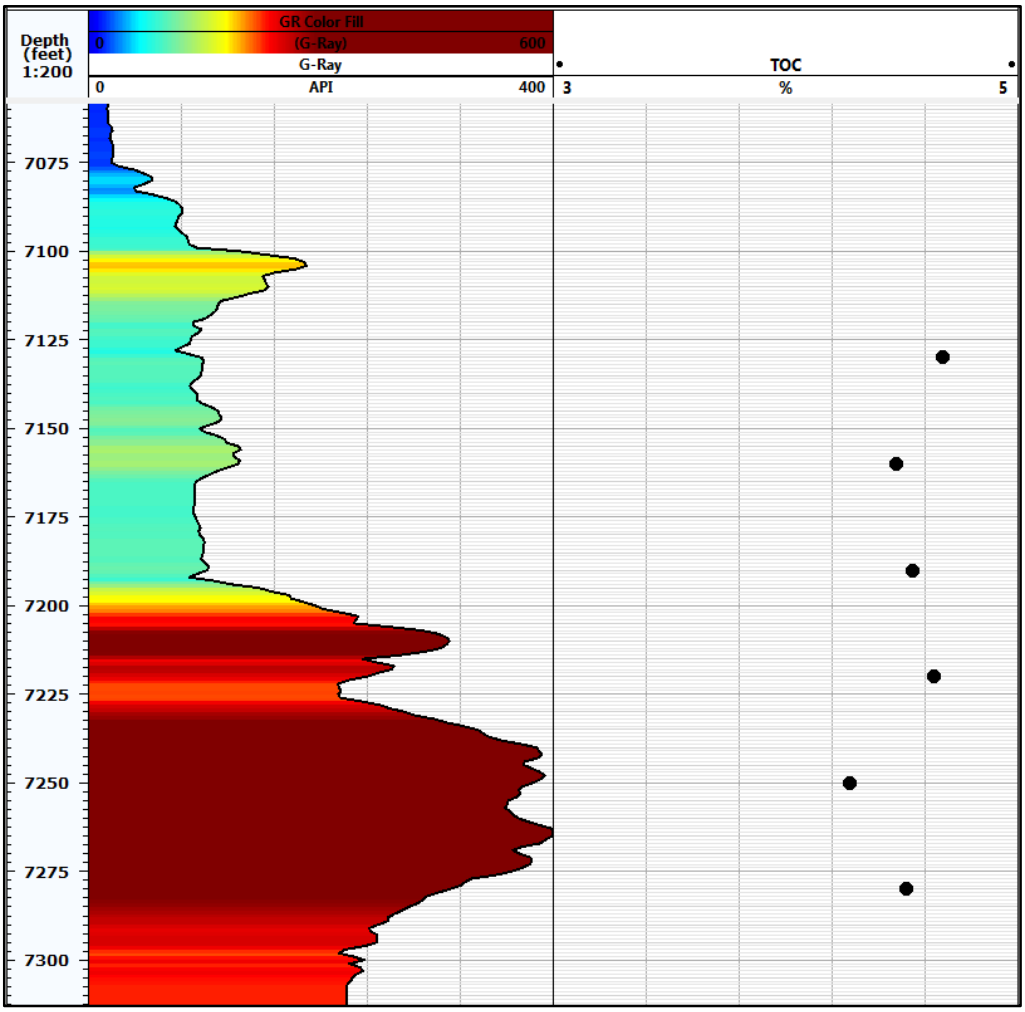

Figure 6.4: A2 well Rock-Eval sampling depths and TOC measurement. The TOC within the Woodford is in average 4.5 making the Woodford a very good source rock.

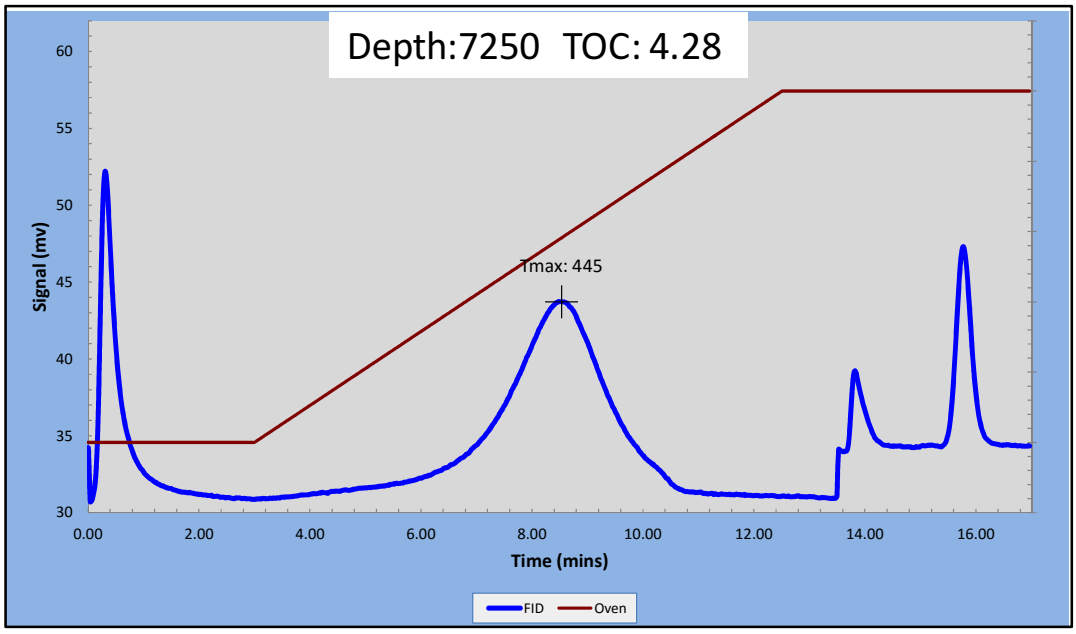

Figure 6.5: The pyrogram of the A2 well sample which is located at measured depth 7250 ft. High S1 and S2 peaks indicate the high oil content and good oil generation potential.

Since the C1 well is a sub-vertical well, there are a few more data points in the Woodford available for the Rock-Eval analysis. From Figure 6.6, four cutting samples at different depths within the Woodford have low to moderate TOC from 0.7-2.19, which means the source rock quality is fair to good. However, this lower value especially from the top sample is interpreted as the result of sample blending and contamination just like the A1 well. The overall TOC value for the C1 well is lower than the real formation and the data quality is affected by the large sampling interval and blended sample with the upper formation. The pyrogram of the C1 well is shown in Figure 6.7. The top sample merely has a S2 peak and low S1 peak. They both confirm the low TOC and poor oil generation potential of that sample due to the contamination. The following three sample have similar moderate S1 and S2 peaks, which are also affected by sample contamination.

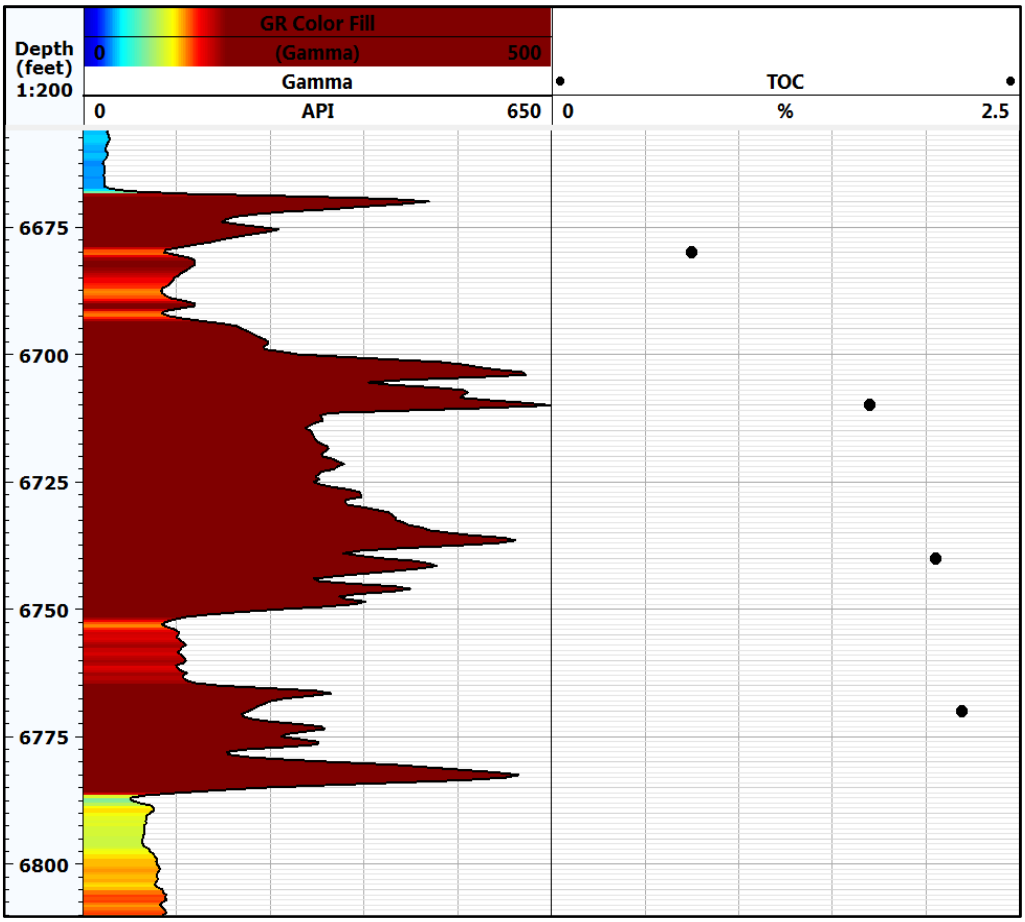

Figure 6.6: Rock-Eval sample points in the C1 well. The top sample has lower TOC because the upper formation was blended with the Woodford Shale cuttings. The following three samples suffer minor contamination issues with moderate TOC value.

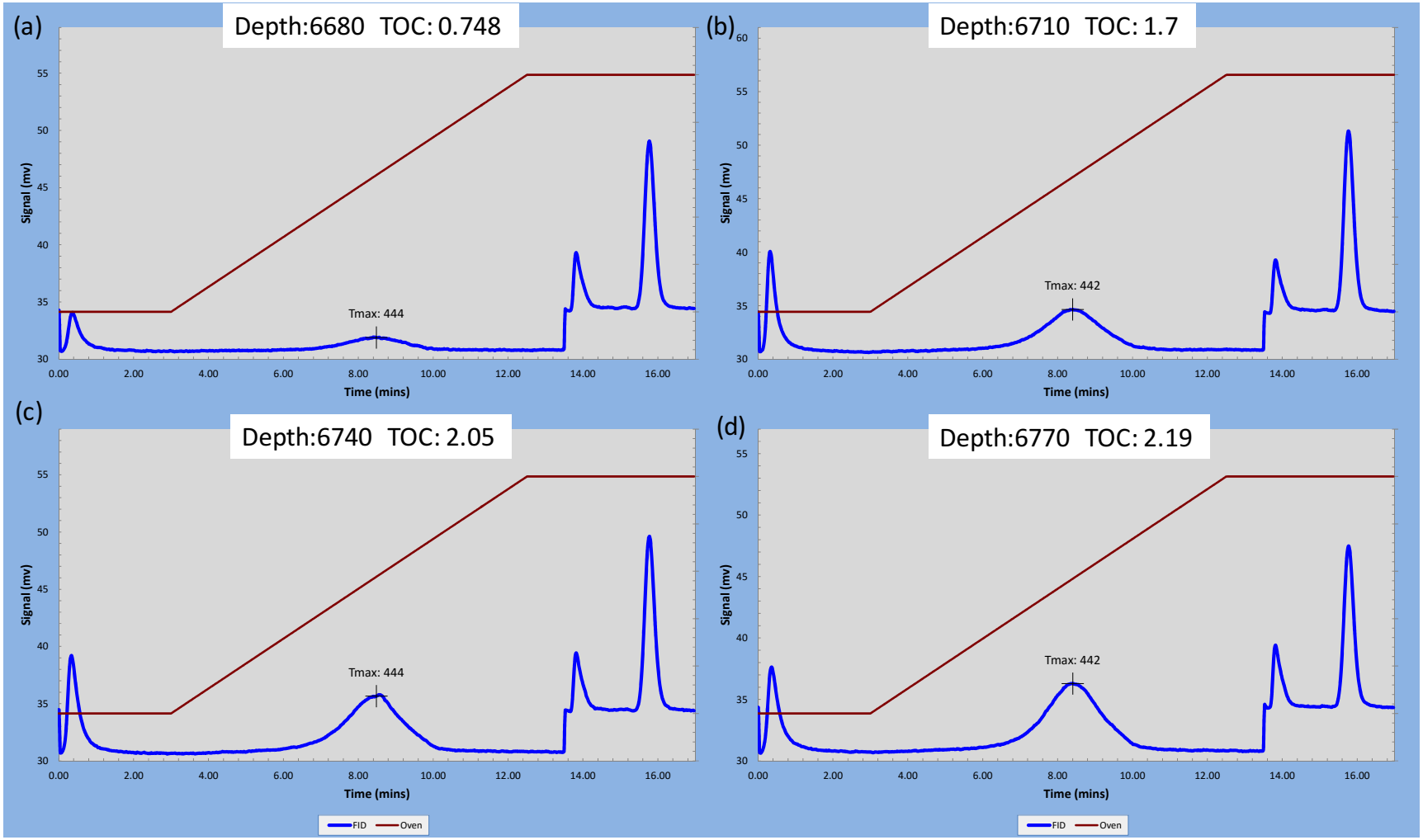

Figure 6.7: Pyrograms for the C1 well samples. (a) The top sample is contaminated thus has low S1 peak and unnoticeable S2 peak. (b) - (d) are similar, they all have moderate S2 peak and S1 peak, which is affected by minor sample contamination.

The H2 well is the well with the most Rock-Eval data points because many upper points were provided by Longfellow Energy (Figure 6.8). The lowermost three points are self-measured data points because there are high Mo and V pockets from the XRF profile that need to be verified. The TOC is generally increasing from top to the bottom. The top sample has a lower reading of 2.5% but still is considered as a good source rock. The average TOC throughout all the samples is about 6% which is considered an excellent quality source rock. The lower three points have extremely high readings of 10% because of the high Mo and V at these depths. From Figure 6.9, a cross plot of all the Rock-Eval samples' TOC with Mo and V shows there is a high correlation between TOC and Mo and V. Mo and V are used as proxies for a paleo-anoxic environment which is beneficial for preserving the organic matter.

From Figure 6.10, four pyrograms are selected to represent the source rock quality through the entire wells. The first one has lower TOC value. The lower gamma ray reading at that depth confirmed that the sample itself is not rich in organic matter, which ultimately leads to low TOC value instead of being affected by contamination such as the A1 and C1 wells. The 6920 foot sample represents the average level of the other provided data points. The very high TOC value associated with high S1 and S2 peaks indicate that the Woodford is oil prone and still has high potential to generate oil. The lower two self-measured pyrograms have extremely high TOC and high Mo and V pockets. The S1 and S2 peaks are both very high.

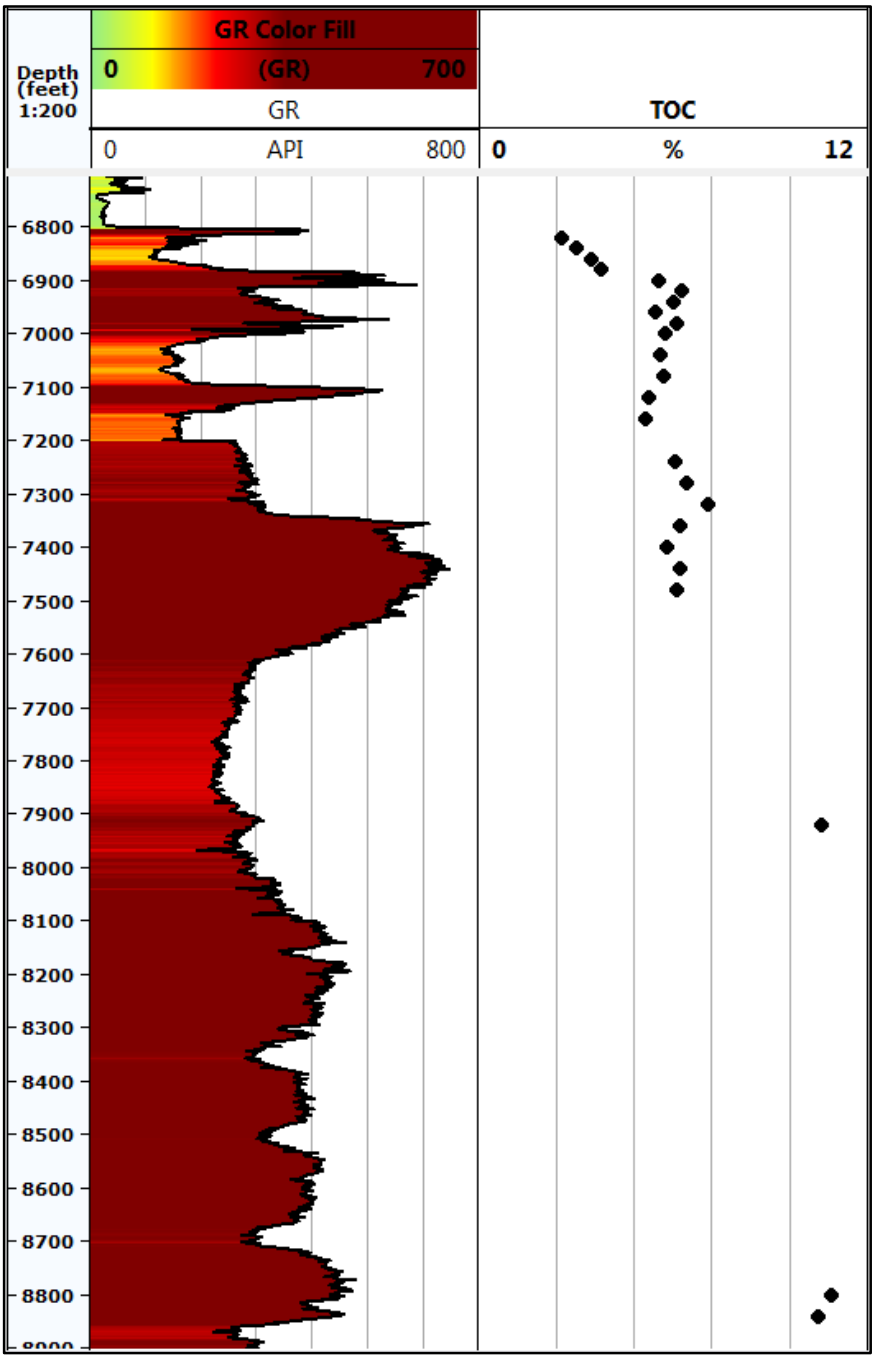

Figure 6.8: Rock-Eval data points along the H2 well. The average TOC is about 6% making the Woodford Shale an excellent source rock, the lower three data points are extremely high TOC values which correlate with the high Mo and V readings which indicates there was a paleo-anoxic environment, which benefits preserving organic matter.

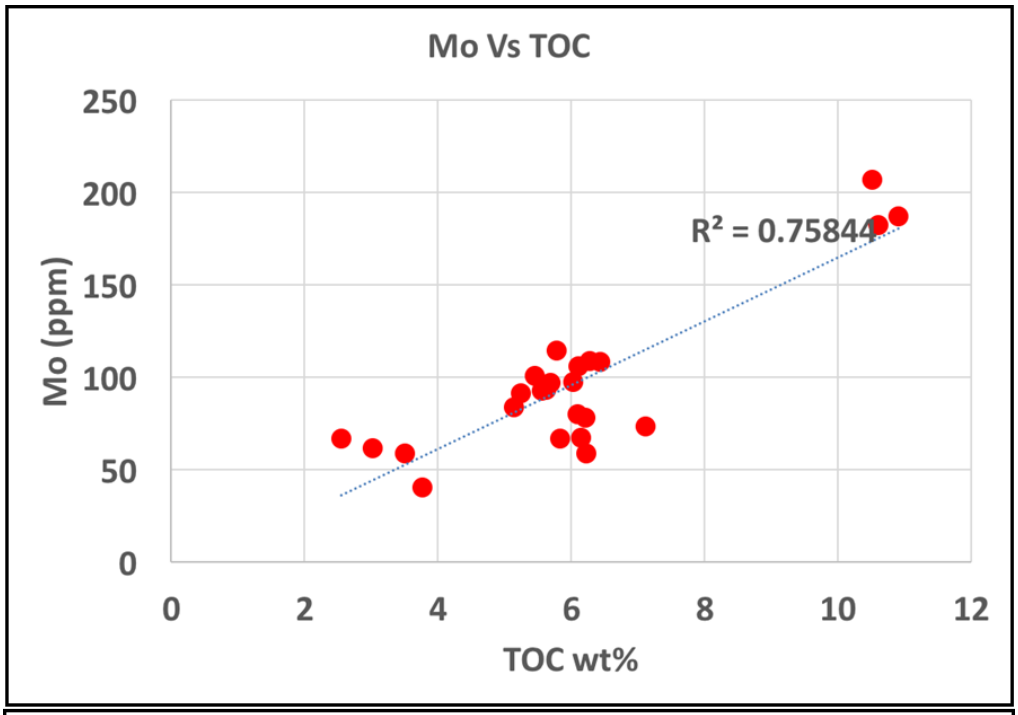

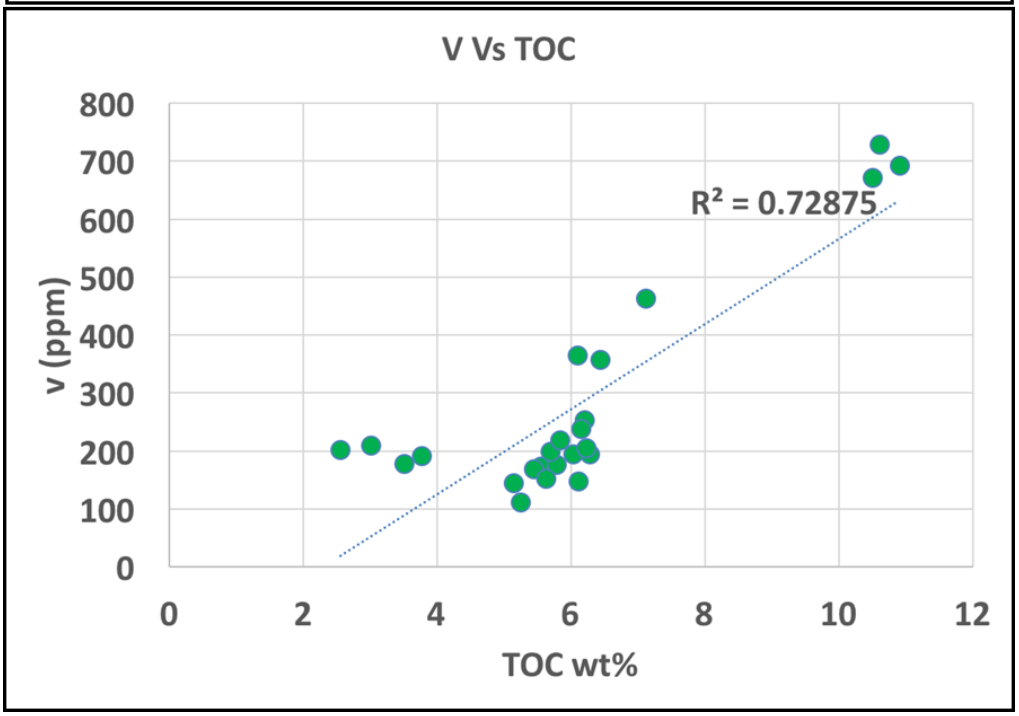

Figure 6.9: High correlation between Mo V and TOC. High Mo and V are proxies for paleo-anoxic environment.

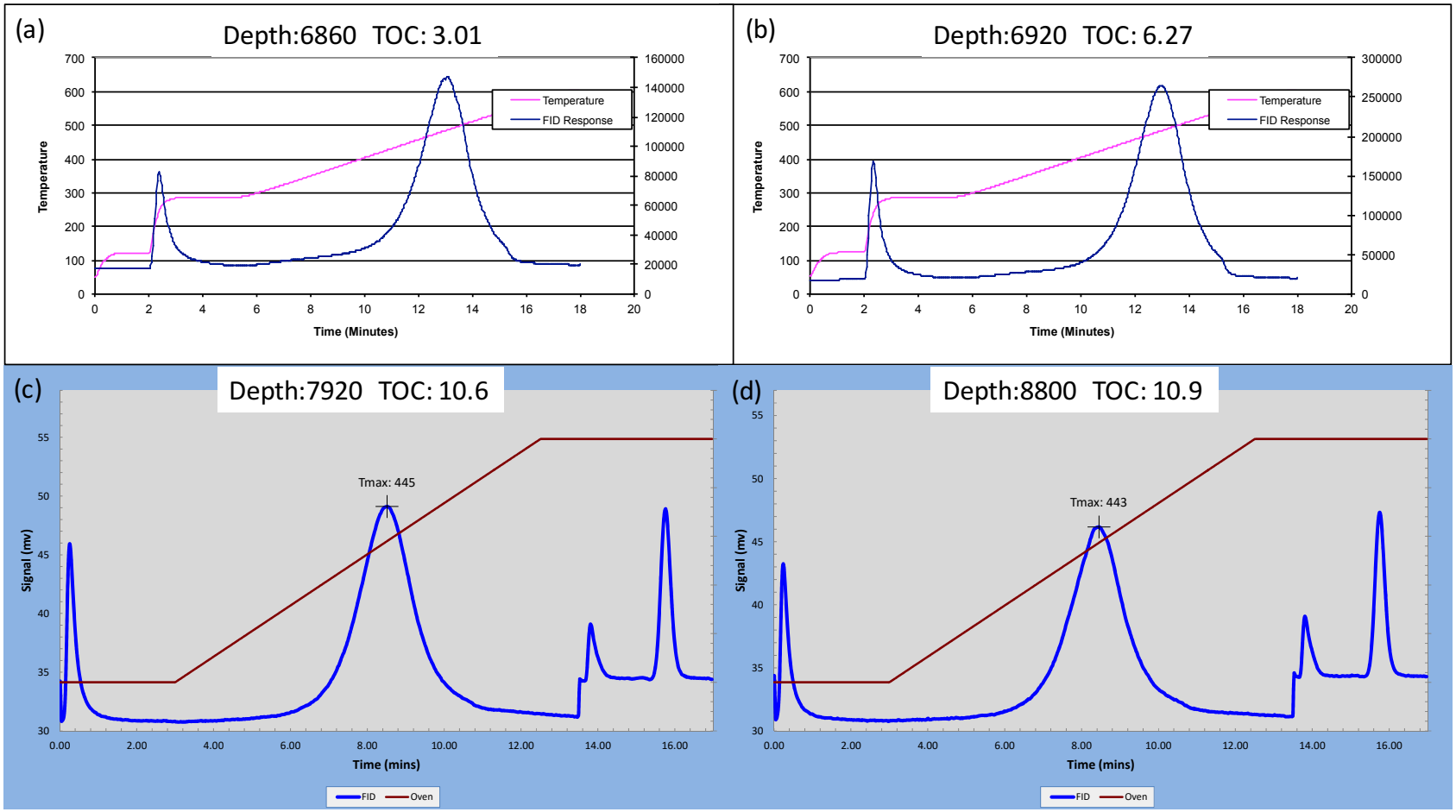

Figure 6.10: Pyrograms summary of H2 well samples. The S1 and S2 peaks are all obvious with optimistic values, which indicates that the Woodford Shale is oil prone and has a high oil generation potential.

A pseudo-Van Krevelen diagram is the most common method to evaluate the kerogen type and maturity. It is a cross plot of HI and OI to observe the data points fall into certain kerogen type zones (Espitalie et al., 1977; Peters, 1986; Baskin, 1997).

There are four kerogen types defined based on different organic matter sources, hydrogen and oxygen percentage and depositional environments. Type I kerogen oil generates kerogen that is sourced from land plant debris and fresh water algae, they derive mostly from lacustrine deposits and anoxic or hypersaline lakes. Type 2 kerogen produces oil and gas; the organic matter is sourced from plants, pollen, plankton and animal bodies which mostly originated from the marine environment. Type 3 kerogen is mostly sourced from land plants and produces gas. Type 4 kerogen mainly contains decomposed organic matter that does not have any production potential. (Tissot et al., 1974; Hunt, 1979; Tissot and Welte,1984; Espitalie et al., 1985).

The Woodford Shale kerogen is interpreted as Type 2 kerogen based on former studies indicating deposition in shallow marine water (Lewan, 1983). From Figure 6.11, HI and OI of four wells were plotted in the pseudo-Van Krevelen diagram. A2 well and some H2 well data points fall into the Type 1 kerogen field. Most points of the C1 and A1 well fall within Type 2 kerogen field which is the marine shale type source rock. The wide distribution of data points that causes errors and misleading results for kerogen type interpretation is mainly because the mineral matrix and organic enrichment affect absolute and relative hydrocarbon and CO_2 yields and ultimately affects the HI and OI obtained by Rock-Eval. Thus pseudo-Van Krevelen diagram has limitation to identify the kerogen type (Katz, 1983; Dembicki, 2009).

Langford and Blanc-Valleron (1990) proposed that plotting S2 vs TOC can avoid the errors introduced by HI and OI plotting and identify the kerogen type more accurately. In Figure 6.12, the S2 and TOC from all the samples are plotted and from the diagram, the data points are more concentrated in the mixed Type 2 and Type 3 kerogen which is an oil and gas prone resource shale.

To analyze the maturity of the shale, a cross plot of HI vs T_{max} can identify the kerogen type and maturity at the same time. From Figure 6.13, all the data points have similar T_{max} values which indicates that the Woodford Shale is located in the oil window and kerogen type falls within the Type 2 and 3 mixed.

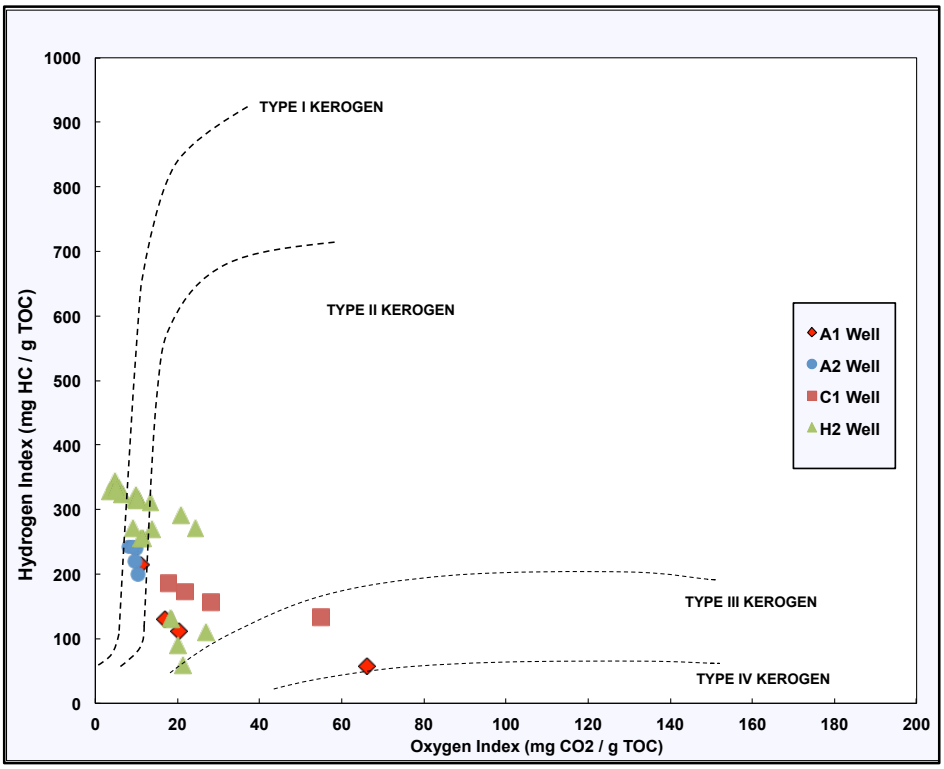

Figure 6.11: Pseudo-Van Krevelen diagram of all the samples. The data points are scattered and located within Type 1 to type 2 kerogen territories. This is the common shortcoming of Pseudo-Van Krevelen diagram in identifying the kerogen type.

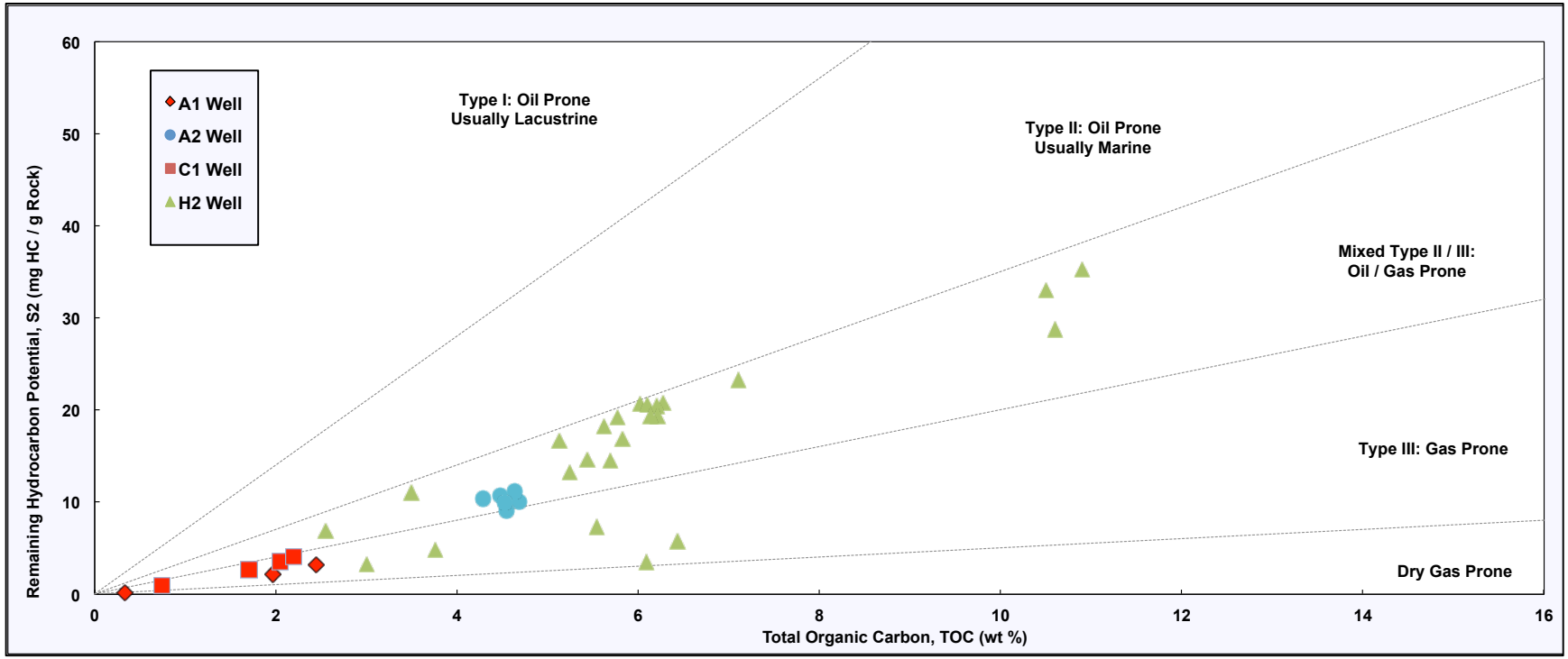

Figure 6.12: Cross plot of S2 and TOC of all the samples. The distribution of data points indicates that the Woodford Shale is mixed Type 2 and Type 3 which is oil and gas prone shale.

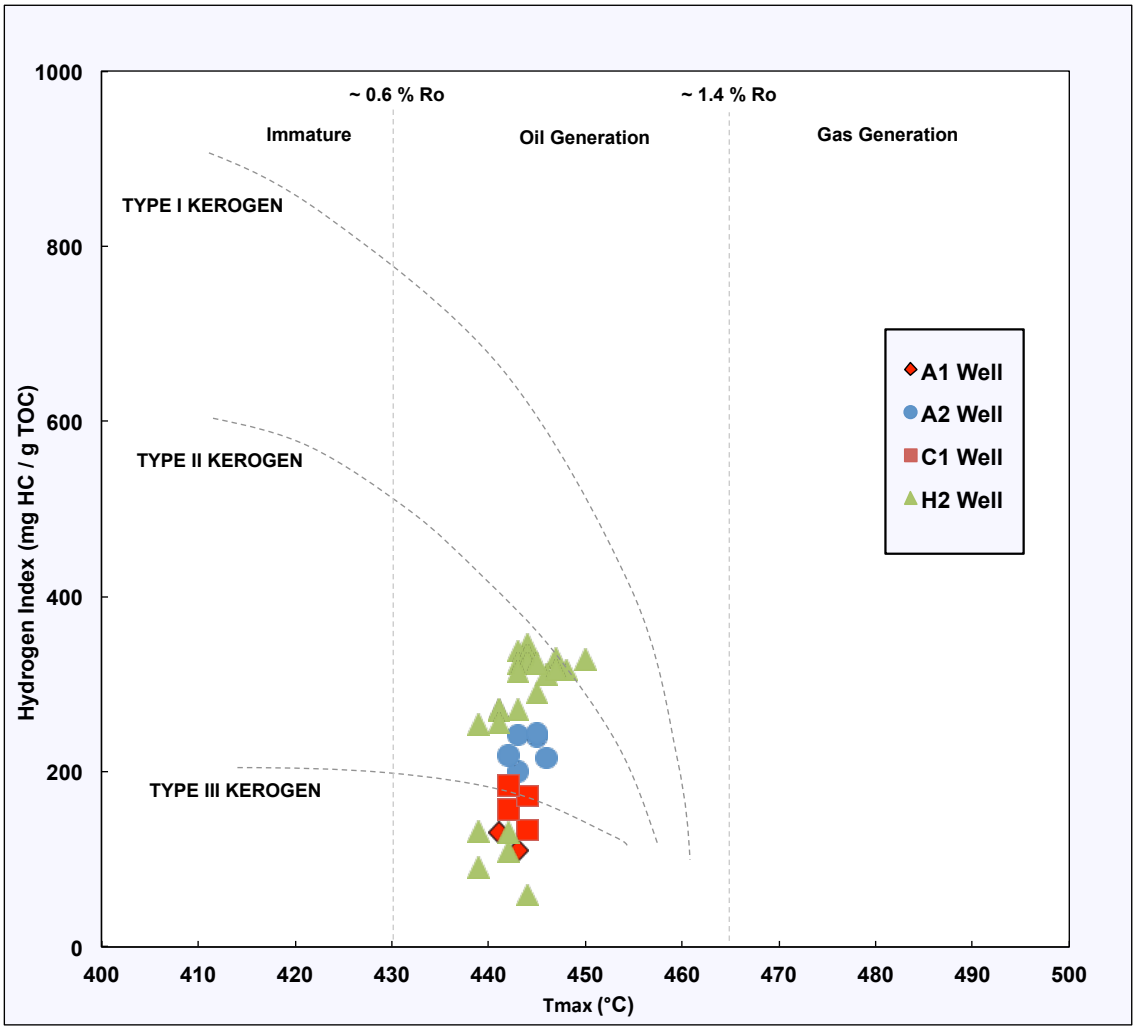

Figure 6.13: Cross plot of HI vs T_{max}, all the data points indicate that the Woodford Shale is in the oil window and the kerogen type is type 2 and type 3 mixed.

The type of kerogen is essentially defined by different organic matter sources and depositional environments and using the element ratios such as H/C and O/C as conditions of identification (Tissot et al., 1974). The element ratio still cannot be a direct indicator of the depositional environment and organic matter source type because it can be affected by various factors such as during the sample preparation stage, acid treatment and rinsing can remove some kerogen. Mixing two or even more types of kerogen is common and can also bring confusion when simply using a pseudo-Van Krevelen plot to identify the kerogen type (Dembicki, 2009). When the TOC is lower

than 2% the mineral matrix is going to affect the Rock-Eval process and elevate the OI and lower the HI dramatically (Espitalie et al., 1980; Katz, 1983). Due to the factors mentioned above, plotting the HI and OI cannot be used alone for kerogen classification. The better solution is to use pyrolysis-gas chromatography (PGC). It analyzes the materials that are associated with the S2 peak. The gas chromatography analysis focuses on the chemical information during kerogen thermal decomposition, which provides a direct indicator of kerogen type even when there is a mixture of kerogen (Giraud, 1970; Larter and Douglas, 1980; Dembicki et al., 1983; Dembicki, 2009).

Chapter 7: Microseismic Interpretation

7.1 Microseismic Model Analysis

The stimulated well with the microseismic data is the well H2 operated by Longfellow Energy. The H2 well was drilled from north to south, landed at the lower middle part of the Woodford Shale where the gamma ray is low, and brittleness is high. The microseismic data was obtained from the surface survey where 1413 receiver stations were spread along the 12 radial lines in an elliptical shape (Figure 7.1). There are a total of 12 stages of perf and plug stimulations along the H2 wellbore and 1552 events were recorded with the coordinate location, time, amplitude, signal/noise ratio, event strike and dip.

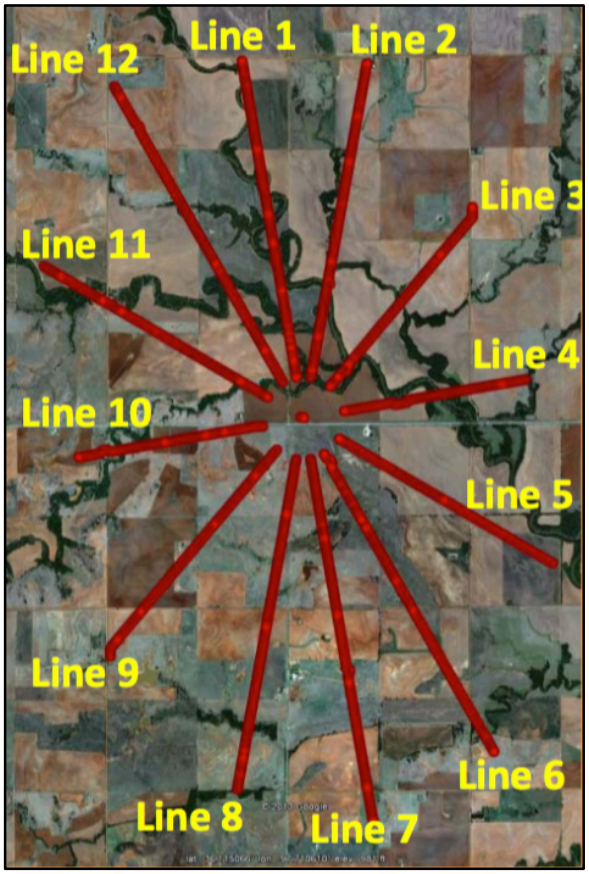

Figure 7.1: Microseismic surface array distribution map. Stations are equally distributed along the 12 survey lines.

The first step was to import the events by stages into the Petrel^{TM} software. The microseismic events were imported as points with attributes (Figure 7.2). The amplitude of the microseismic events were normalized to the magnitude using the equation 1 as follows.

$$Magnitude = (\log_{10} Amplitude - \frac{\min \log_{10} Amplitude}{\max \log_{10} Amplitude - min \log_{10} Amplitude} \times 4) + 4$$

In this equation:

Magnitude means the normalized magnitude for one certain microseismic event.

Amplitude means the amplitude of one certain microseismic event.

Minlog$_{10}$Amplitude means the minimum value of all events' logarithmic amplitude.

Maxlog$_{10}$Amplitude means the maximum value of all events' logarithmic amplitude.

After normalization, all of the amplitudes were calculated into the magnitude within the range from -4 to 0. The range is defined to keep all the magnitudes below 0 for counting convenience and based on the general microseismic magnitude range. Thus the magnitude imported is not considered as the real magnitude, but as the relative magnitude.

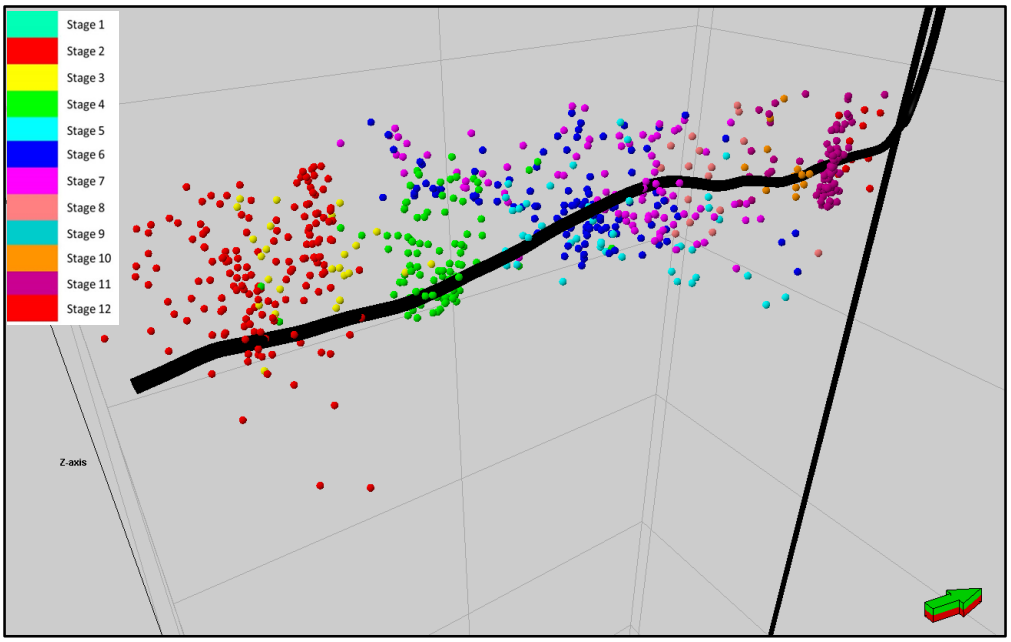

Figure 7.2:12 stages of microseismic events along the H2 well. Stages are differentiated by colors. The vertical well near the H2 well head is the H1 well.

To analyze the microseismic distribution pattern, a local sequence stratigraphic framework was constructed with 28 nearby wells. Seven parasequences were identified within the Woodford Shale formation based on the gamma ray log, resistivity log, density and neutron porosity log. Two cross sections were used for correlation: A-A' from north to south and B-B' from west to east (Figure 7.3).

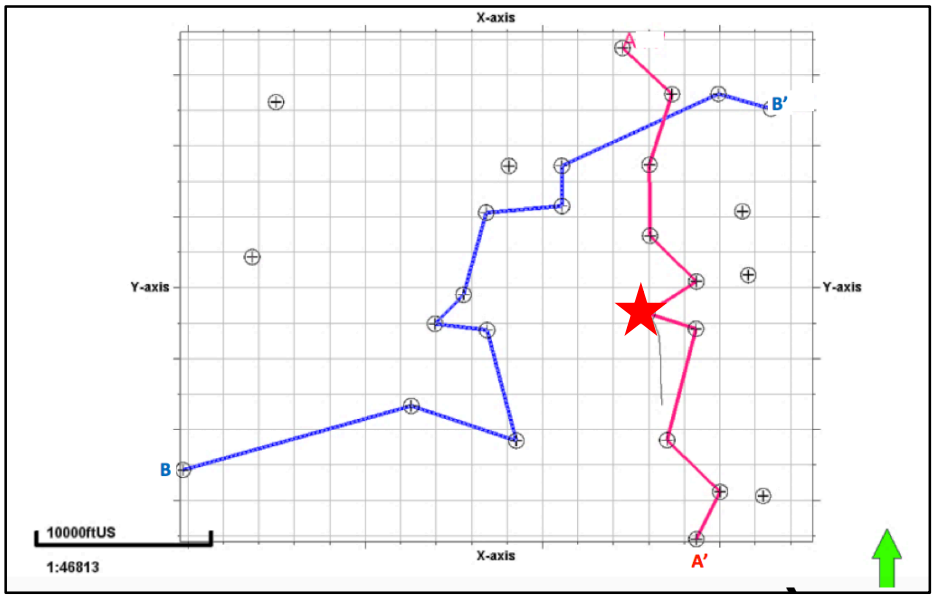

Figure 7.3: Cross section for the local correlation near the microseismic survey area, A-A' from north to south, B-B' from west to east. The entire area is about 28 square miles. Microseismic well locations are in the middle right part at the star.

In cross section A-A’ (Figure 7.4), the key parasequence surfaces have the higher continuity with all the existing sequences that can be correlated. For the crossection B-B’ (Figure 7.5) the lower parasequences 1, 2, 3 and upper parasequence 7 pinch out to the west, thus the Woodford is thinner. In the westernmost well, the Woodford Shale was deposited directly on the Viola Limestone. This indicates that there is a paleo topographic high that was exposed during subaerial exposure of the Hunton Group and Sylvan Shale all of which underlie the Woodford deposits. The paleo-topographic high area does not deposited the lower Woodford parasequences and underlying formations.

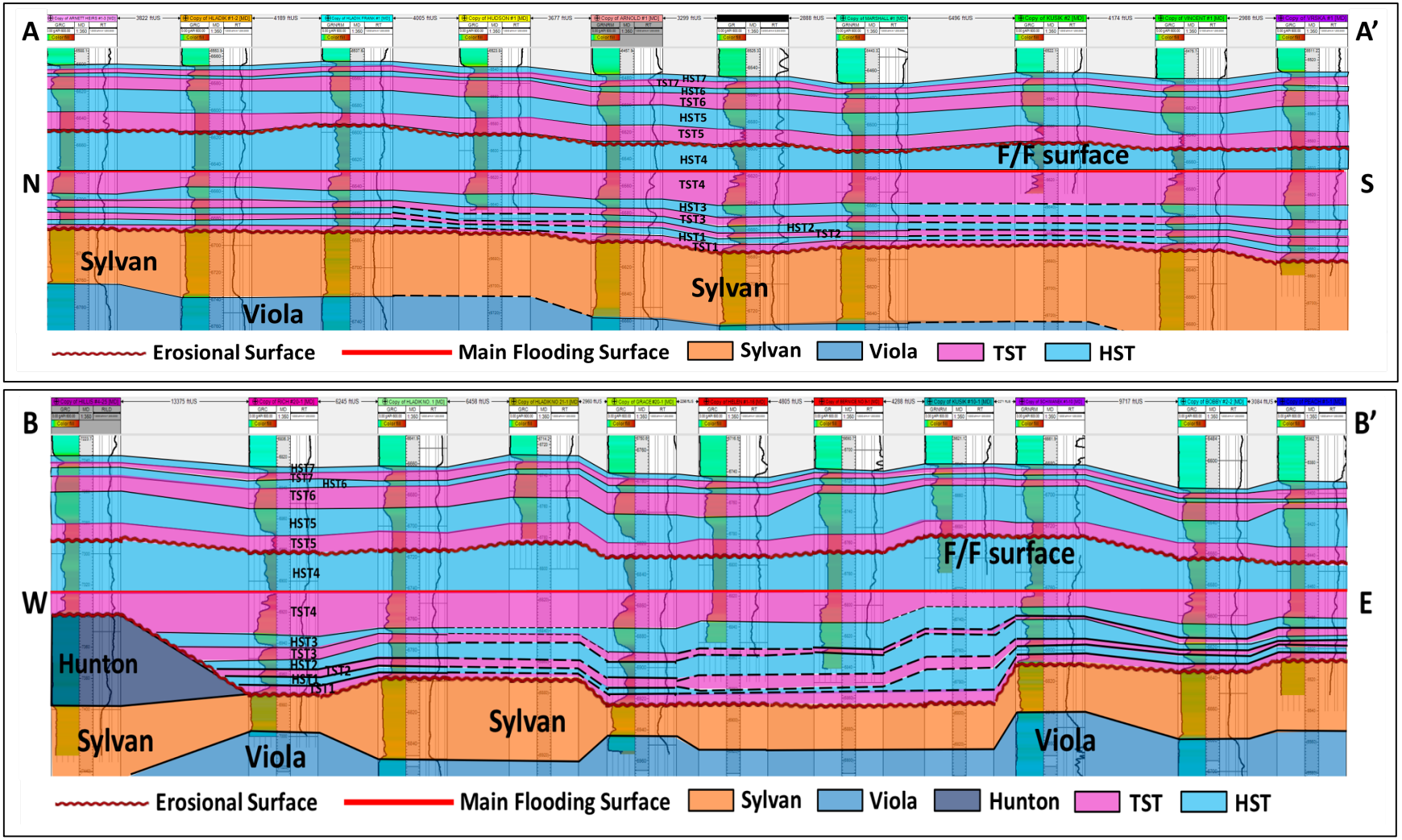

Figure 7.4: Cross section A-A' and B-B'. The well log on the left is the gamma ray log and the resistivity log is on the right. A-A' has more lateral continuity than B-B'. Note two cross sections use the two different horizontal scales.

The stratigraphic framework model was constructed after completing all the correlations. Smaller polygons were used to cover only the microseismic impact area using the pre-identified key surfaces from the larger area in order to make the model run smoothly. The stratigraphic model contains 14 zones of which seven are highstand system tracts and seven are transgressive system tracts. There is no pinch out zone within the smaller polygon, and the beds dip towards the southwest (Figure 7.5).

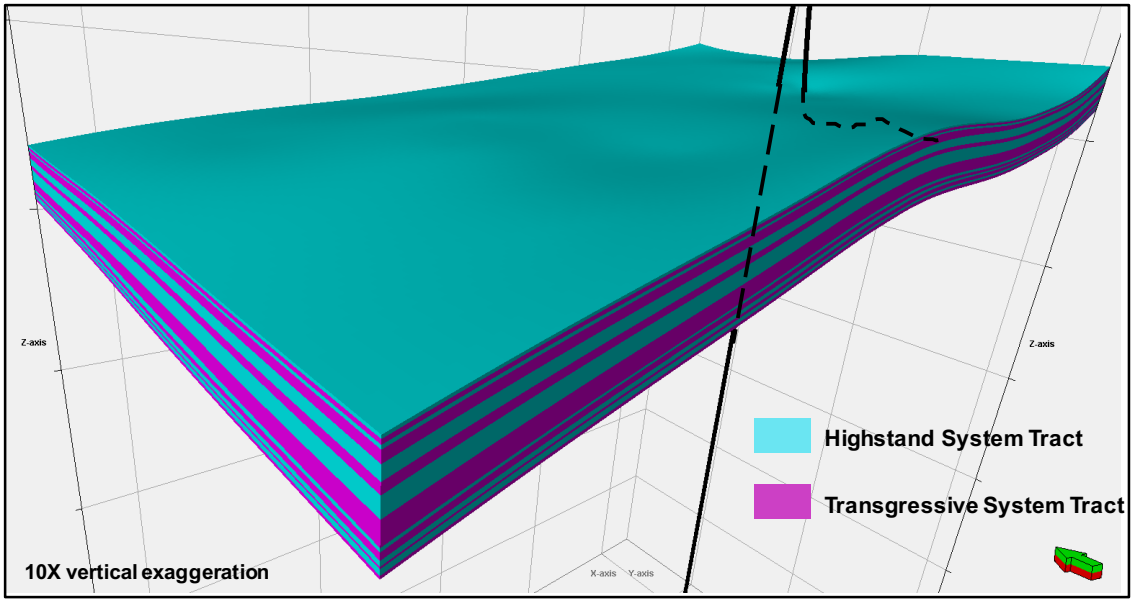

Figure 7.5: Sequence stratigraphic framework model and the stimulated H2 well. Blue color zones stand for the highstand system tract, pink color zones stand for the transgressive system tract.

In many outcrop case studies, the Woodford Shale has the chert interbedded with thin bed shale. These are brittle and ductile couplets (Slatt and Abousleman, 2011) in the shale reservoir. They occur at different scales from first order to third order cycles that correspond with lithofacies changes and paleo-sea level fluctuations. Thus, the brittle and ductile couplets are the consequence of sea level changes and sequence stratigraphy for most cases (Slatt and Abousleman, 2011). This thesis research also constructs a brittle and ductile couplets model using the key surfaces in the sequence

stratigraphic model. The brittle and ductile sections are mainly identified by Young's Modulus and Poisson's Ratio crossover plot. The H1 well has the sonic log derived Young's Modulus and Poisson's Ratio, the brittle and ductile couplets are picked from the H1 well and phantom horizons were made using the sequence stratigraphic framework surfaces (Figure 7.6).

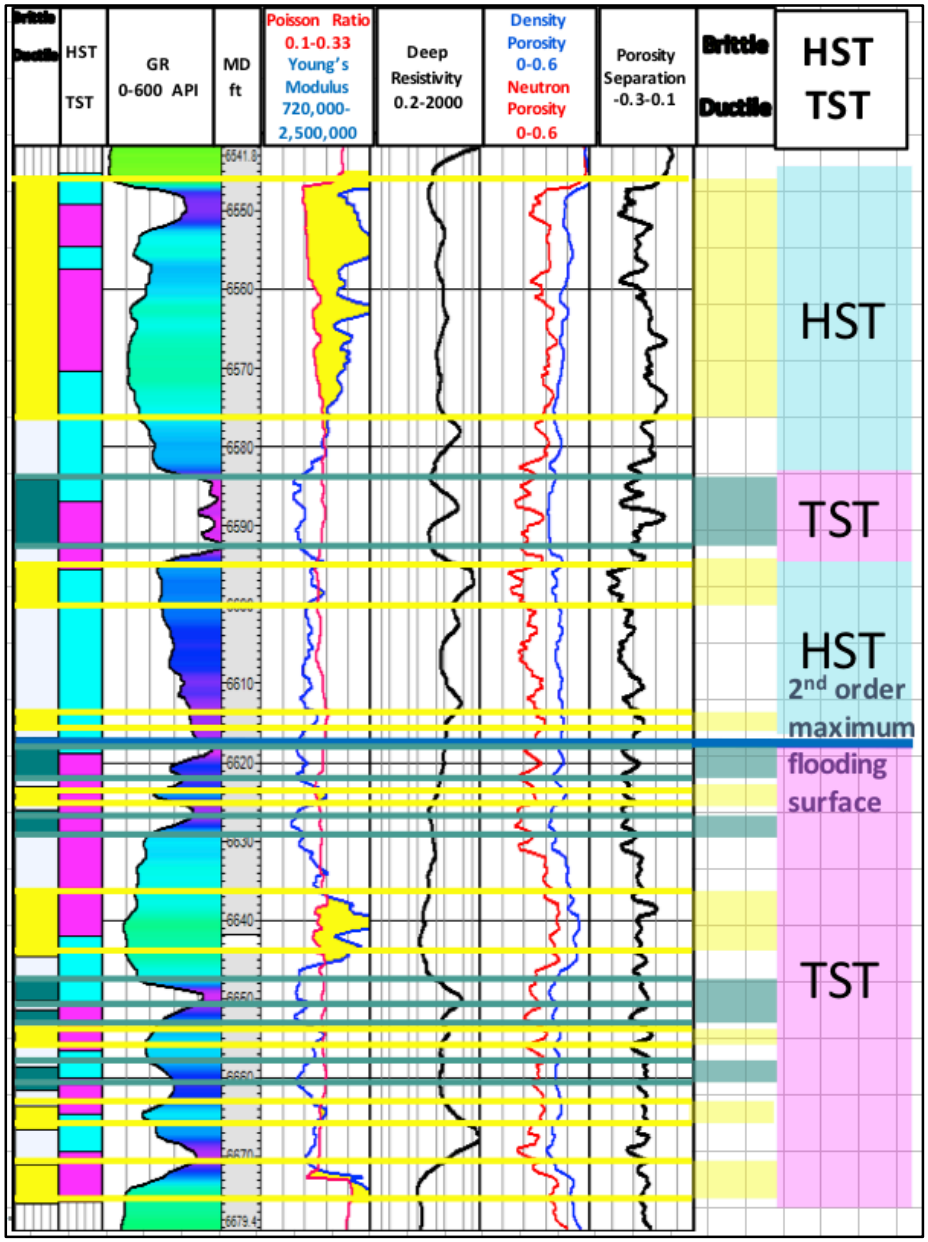

Figure 7.6: H1 well brittle and ductile surfaces identified by Young's modulus and Poisson's ratio crossover plot. Yellow zones stand for the brittle zones and green zones stand for the ductile zones.

There are some gaps between the brittle zones and the ductile zones which indicate that these are neither brittle nor ductile zones (Figure 7.7). From the Figure 7.6, most of the brittle zones are located within the highstand system tract, and most of the ductile zones are located within the transgressive system tract. This is mainly because the highstand system tract contains more quartz than the transgressive system tract, which is clay rich. However, at the beginning of deposition of the highstand system tract, when the shoreline just starts to regress, the sediments are still clay-dominated which makes the lowermost section less brittle. The same situation occurs at the initial stage of the transgressive system tract, when the sea level is not high enough and the sediments are still detrital-dominant. This interpretation explains why the brittle and ductile zones are separated and located within certain parts of the system tracts.

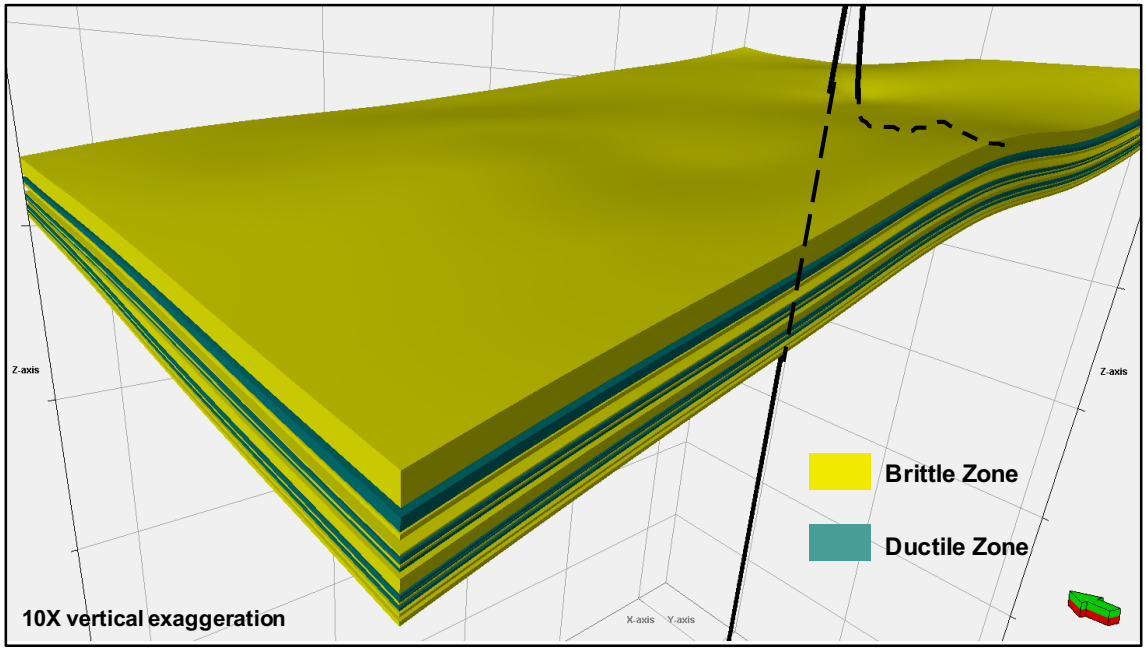

Figure 7.7: Brittle and ductile couplets model identified by Young's Modulus and Poisson's Ratio crossover plot (Figure 7.6).

After both models were established, the microseismic data points and the magnitude were upscaled as the point attributes into both models. The grid size is one

cubic foot to maintain the original event location and not bond with other nearby points (Figure 7.8). The upscaled properties distribution in each zone was analyzed and compared.

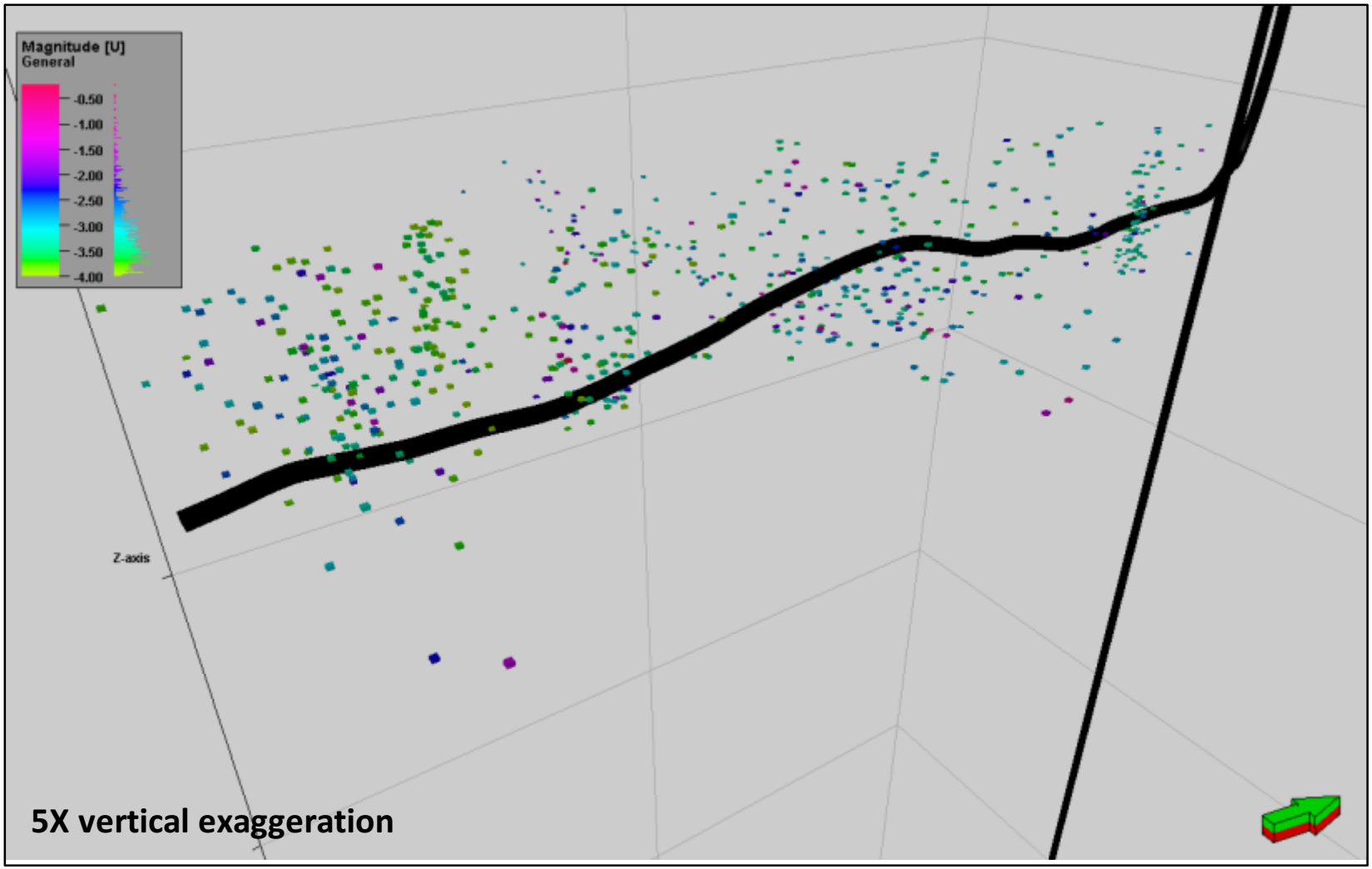

Figure 7.8: Upscaled microseismic events in the sequence stratigraphic framework model. Purple color stands for the smaller negative magnitude; yellow color represents the bigger negative magnitude.

For both models, magnitude and microseismic events were accumulated in each zone; the overall distributions were calculated in the brittle zone, ductile zone, highstand system tract and transgressive system tract, respectively. The calculation results led to the conclusion that there are more events and accumulated magnitude locations in the highstand system tract, and for the brittle and ductile couplet model there are higher percentages of events and accumulated magnitude located within the brittle highstand zones (Figure 7.9). This is mainly because of the different lithology distributions between the highstand systems tract and the transgressive systems tract, which ultimately leads to different brittleness in different zones. Microseismic events are more prone to occur within the brittle highstand system tract due to the greater quartz content.

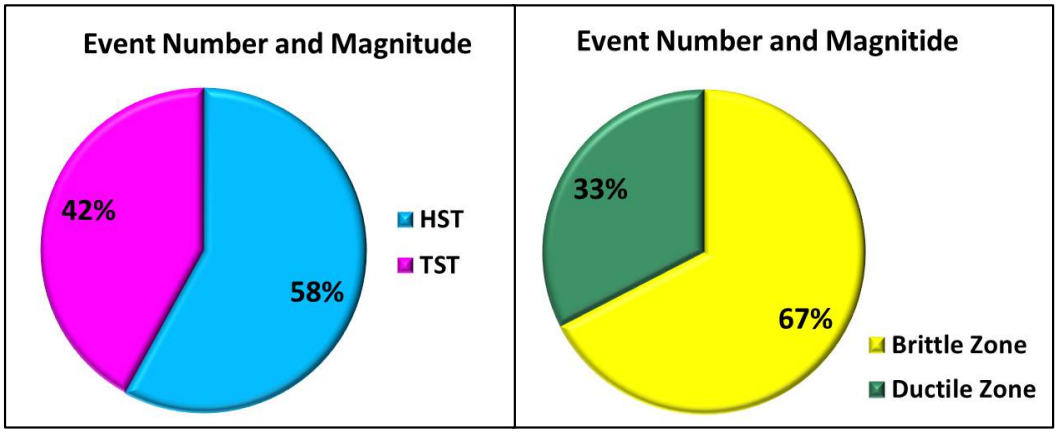

Figure 7.9: Microseismic event and accumulated magnitude distribution in both models. In the sequence stratigraphic framework model there are more events and accumulated magnitude locations in the highstand system tract. The contrast is more obvious for the brittle and ductile couplets model.

7.2 Microseismic Stage Analysis

To evaluate the fracturing job behavior, it is necessary not only to conduct the overall analysis, but also individual stage analyses. Observing the microseimic event location distribution pattern for each stage with the models is an efficient way to

estimate the fracturing job efficiency. It also includes the XRF interpretation discussed in Chapter 5.

Throughout all 12 stages, there are generally three types of fracturing job scenarios with various effects. The first one uses Stage 5 as an example. Stage 5 perforation shots locate within the higher gamma ray, high Al, K and low Si/Al which is interpreted as indicating higher clay content with more ductility (Figure 7.10). In the 3D view, observing from the south, the microseismic events mainly occur vertically and penetrate up towards the Mississippian Lime and down towards the Sylvan Shale (Figure 7.11). This distribution pattern is mainly caused by two factors: firstly, when the perforation shot location is at a ductile zone, fracturing energy is absorbed and the events will mainly grow vertically, following the maximum stress direction and becoming constrained horizontally. The second scenario is when there are natural fractures at the formation boundary. For instance, Stage 5 seems to have natural fractures at the formation boundary, as the limestone no longer acts as a fracture barrier of the shale reservoir and the hydraulic fracturing fluid flows through the natural fractures and grows further vertically (Figure 7.12).

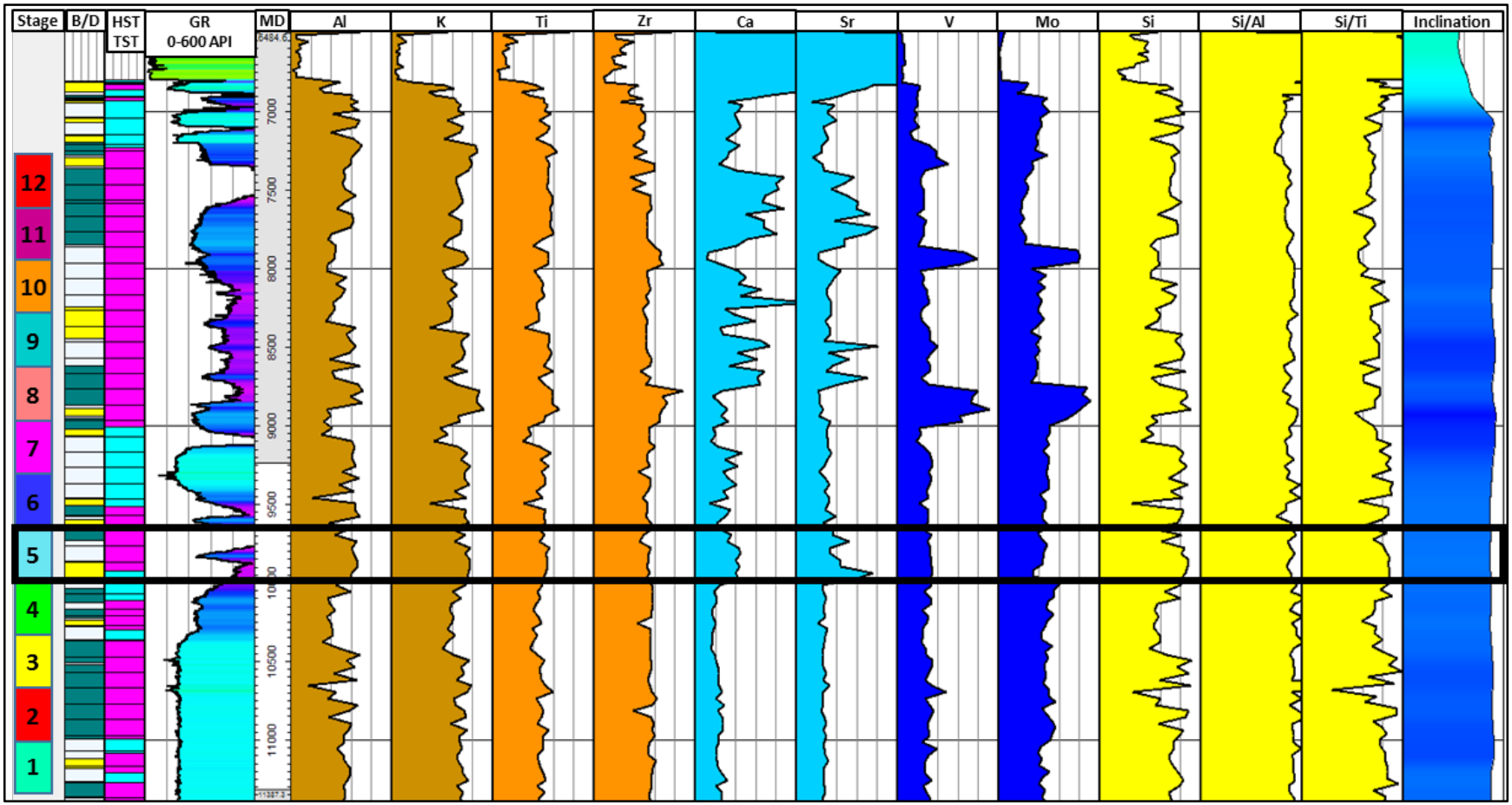

Figure 7.10: XRF profile of the H2 well. During stage five, the high gamma ray, high K and Al and low Si/Al indicates there is high clay content at this stage location.

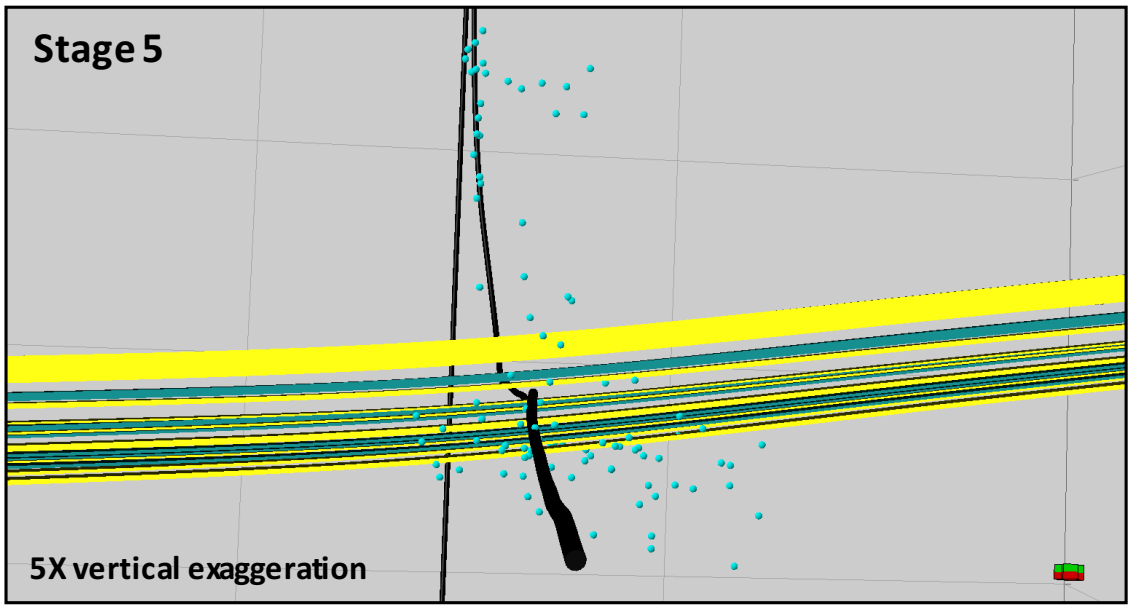

Figure 7.11: Stage 5 in the 3D view with the brittle and ductile couplets model outlining the Woodford Shale formation boundary. Note that the microseismic event mainly grew vertically outside of the Woodford Shale and lateral growth is constrained.

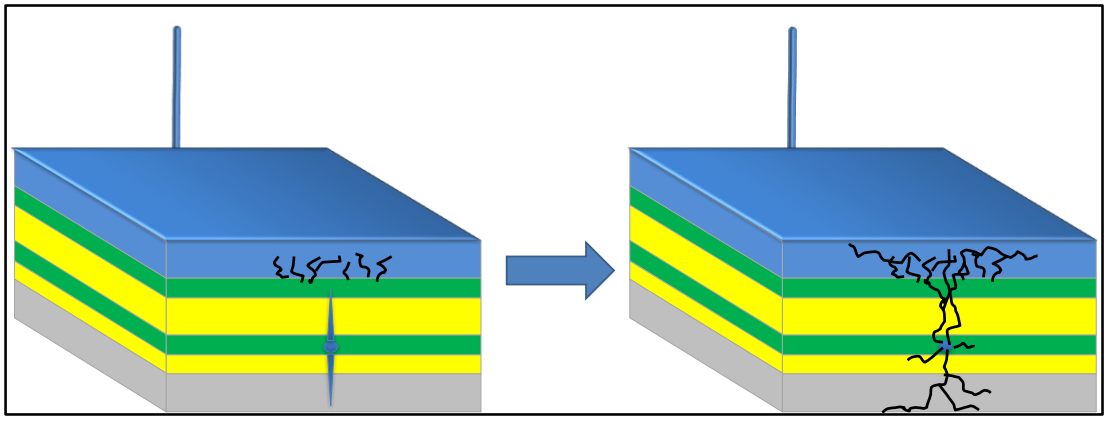

Figure 7.12: Hydraulic fracturing scenario 1, when there are natural fractures existing at the formation boundary, the fracture fluid will take advantage of the weak point and grow further up (blue section represents the Mississippian Lime, yellow section represents the brittle bed within the Woodford Shale, green section represents the ductile bed within the Woodford Shale, and gray section represents the Sylvan Shale formation beneath the Woodford Shale).

The second scenario uses Stage 6 and Stage 7 as an example, where the perforation shots are located within the brittle zone. Both stages are located where there is low gamma ray, high Si/Ti ratio which means the section is rich in biogenic quartz (Figure 7.13). From the 3D view, more microseismic events are located within the

Woodford and extend horizontally. When screening out the outside event, the microseismic data points show a distribution pattern that follows the beds dipping direction, which indicates the hydraulic fractures grow along the brittle bed laterally (Figure 7.14; 7.15).

The second fracturing scenario is demonstrated in Figure 7.16, which represents when the perforation shots locate within the brittle zone. Since the perforation initiates within the zone easiest to break, the energy is released not only to penetrate the brittle zone vertically but also to create hydraulic fractures laterally within the brittle zone. Thus the hydraulic fractures are more prone to stay within the target formation and extend horizontally along the bed which leads to higher fracturing efficiency (Figure 7.16).

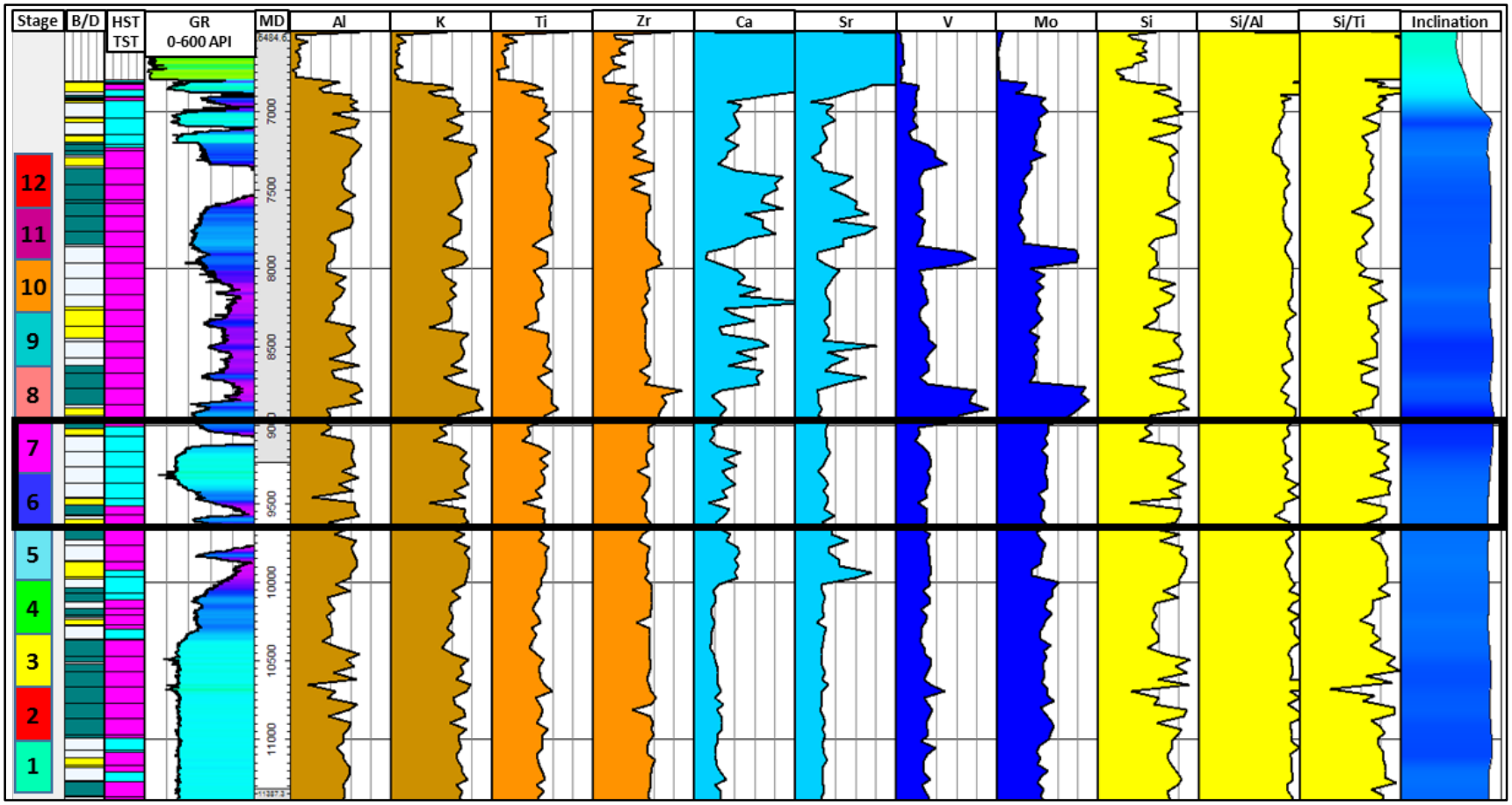

Figure 7.13: XRF profile of the H2 well with stage 6 and stage 7 highlighted. Both stages have a low gamma ray and high Si/Ti ratio, interpreted as a biogenic quartz rich zone and higher brittleness.

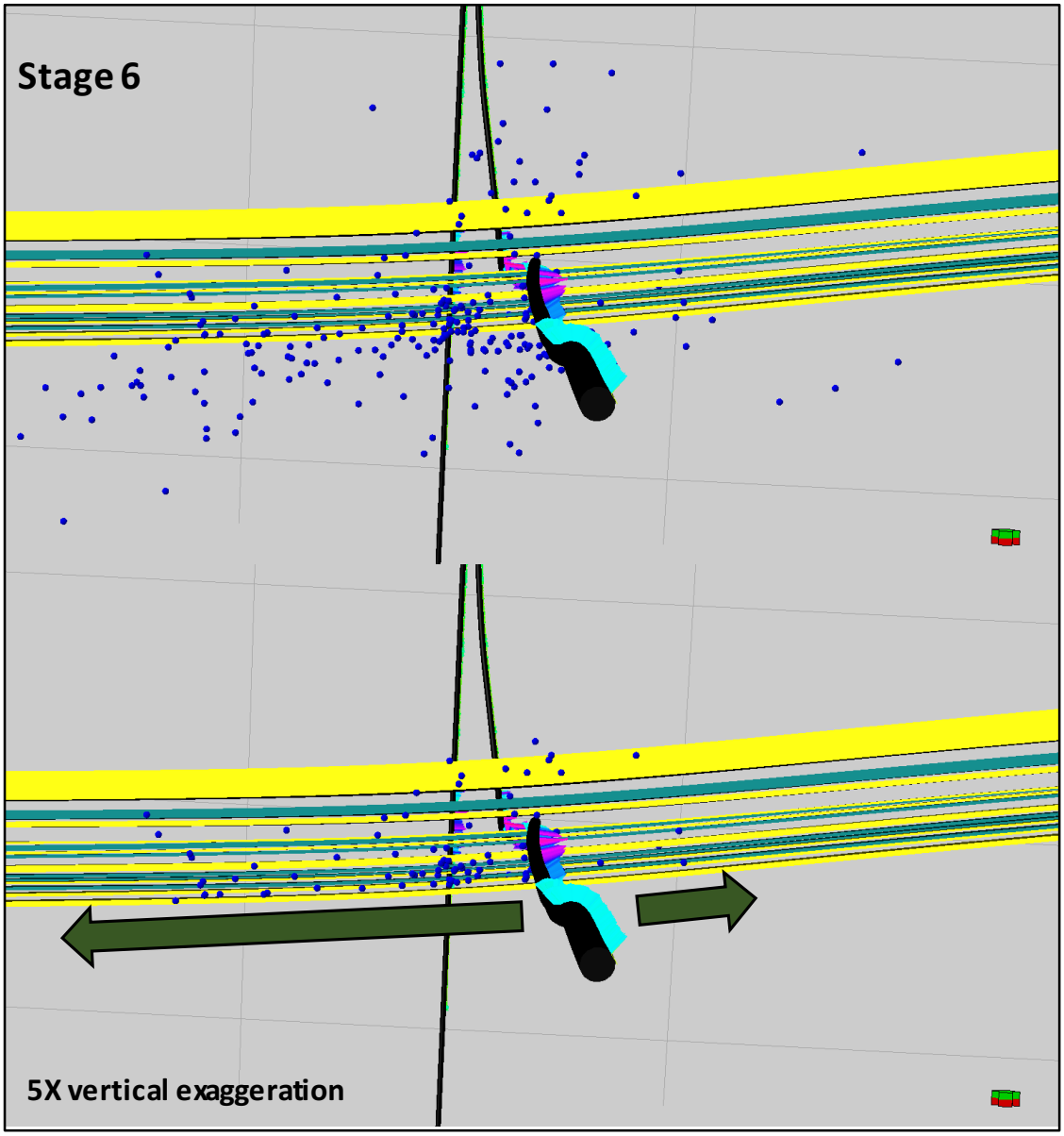

Figure 7.14: Stage 6 in 3D view with brittle and ductile couplets model intersection as a background outline of the Woodford Shale. For this stage, there are more microseismic events located within the target formation which grow horizontally, thus enhancing the fracturing efficiency.

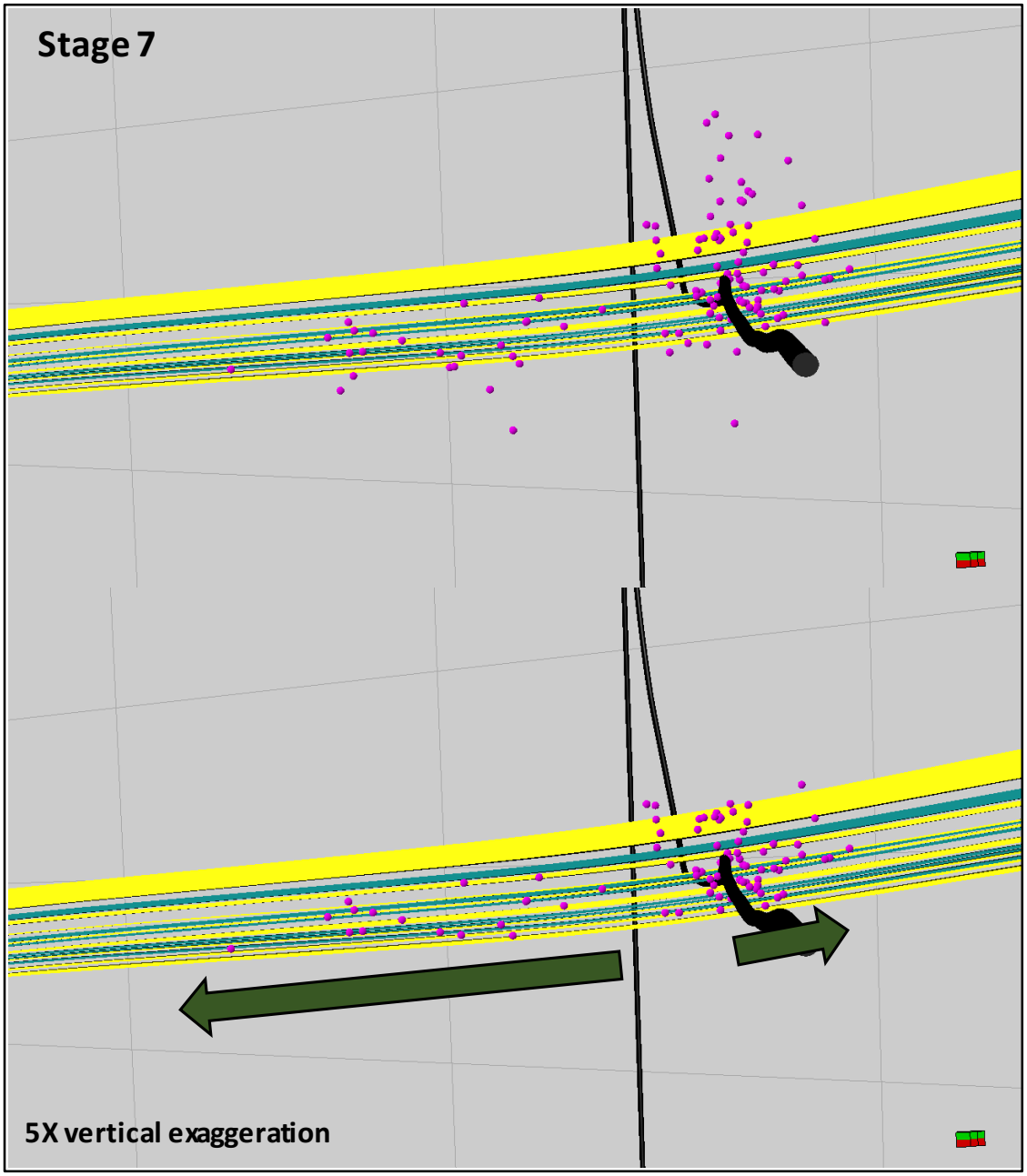

Figure 7.15: Stage 7 in the 3D view, similar to the Stage 6 when stimulation occurs in the brittle zone, it is more likely that the fractures will grow laterally and stay within the target formation. When screening out points that are outside of the formation, the microseismic data points show the trend of growing along the bedding plane.

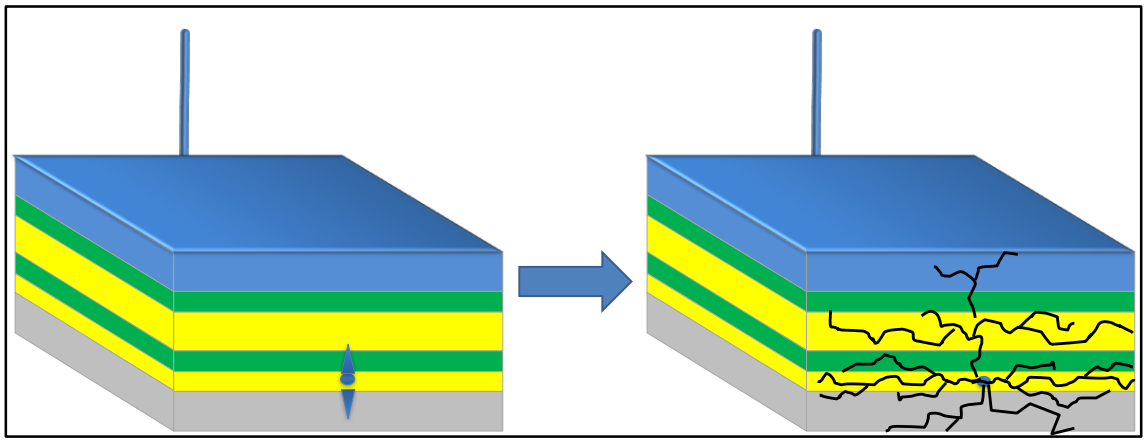

Figure 7.16: Hydraulic fracturing scenario 2, when the perforation shots are located within the brittle zone, the fractures will be more prone to stay within the target formation and extend laterally. (Blue section represents the Mississippian Limestone, yellow section represents the brittle beds within the Woodford Shale, green section represents the ductile bed within the Woodford Shale, and gray section represents the Sylvan Shale formation beneath the Woodford Shale).

The third scenario uses Stage 8 as an example. From the XRF profile and well log. Stage 8 is located within a high gamma ray zone; Al, K and Si are also very high which indicates the section is composed of high clay content (Figure 7.17). Mo and V, the paleo-anoxic environment proxies, are abnormally high, which indicates the water circulation was poor during deposition, thus preserving organic matter. Chapter 6 showed that there is a high correlation between TOC, Mo and V, thus verifying the high TOC content at the Stage 8 section. High organic matter and clay content made this section very ductile.

There is another abnormally high Mo and V section near Stage 10. Projected Mo and V profiles along the horizontal well track show the discontinuity of these two sections. Considering the deposition surface is flat along the well strike direction, the interpretation of these two abnormal high sections are pinched out horizontal beds within the formation (Figure 7.18).

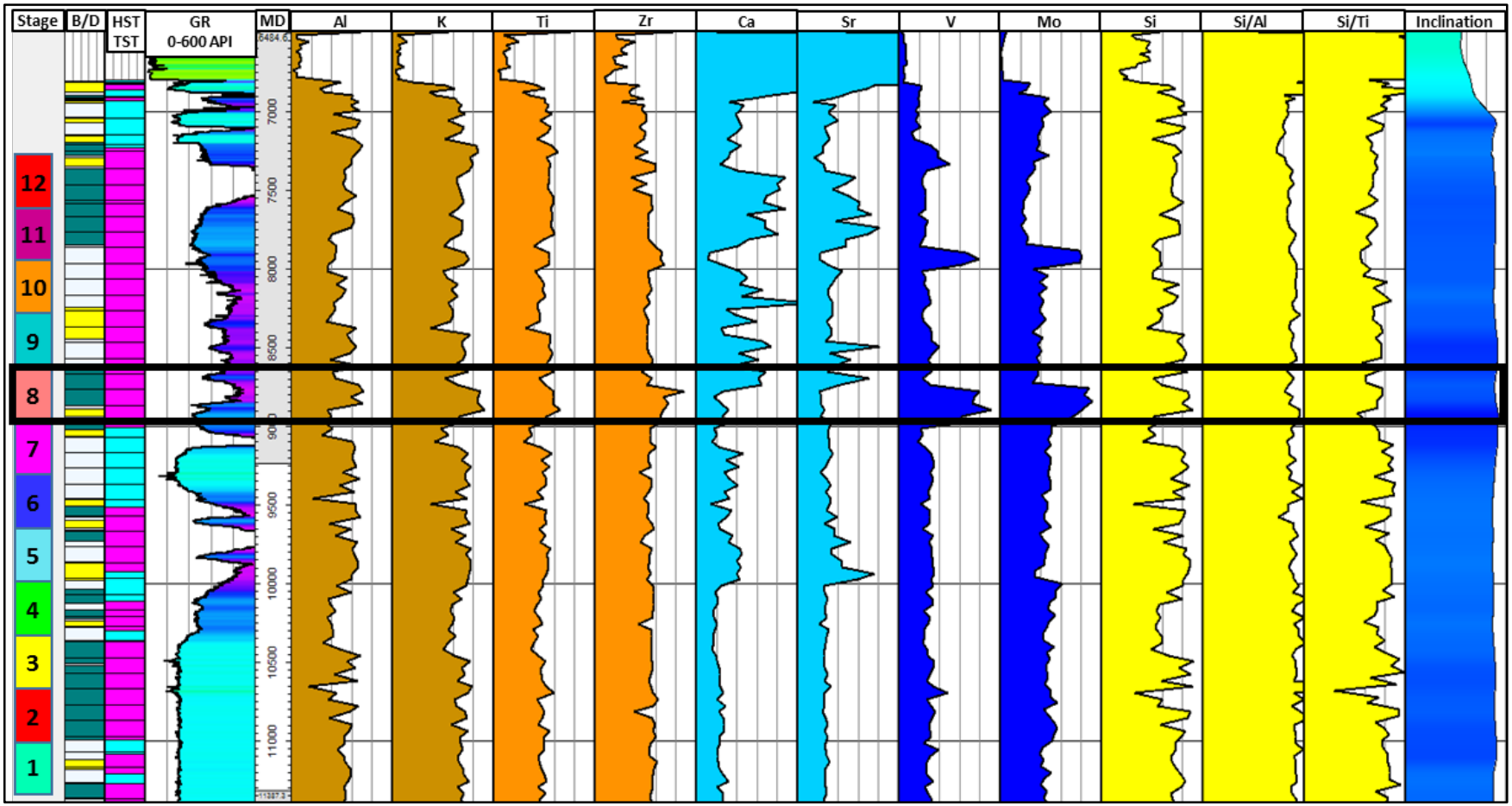

Figure 7.17: XRF profile of the H2 well with Stage 8 highlighted. Stage 8 has characteristics of high clay content and high TOC due to high Al, K, Mo and V.

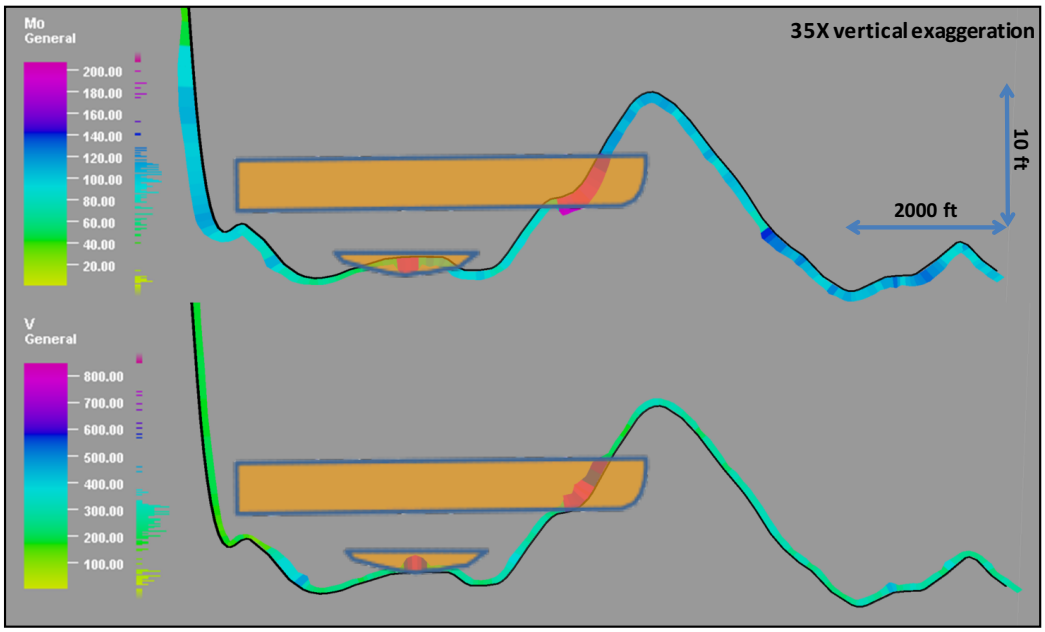

Figure 7.18: Mo and V profile projected along the horizontal wellbore, the two abnormal high sections are independent and interpreted as the pinched out organic rich beds.

From the 3D view, Stage 8 microseimic events are constrained close to the wellbore due to the formation ductility. Fewer events occur during Stage 8 represent a lower hydraulic fracturing efficiency (Figure 7.19). For fracturing scenario 3, when the perforation shots are located in the ductile zone, the energy is mainly absorbed by the formation and the hydraulic fractures cannot grow either vertically, or penetrate the formation, or extend horizontally within the formation (Figure 7.20).

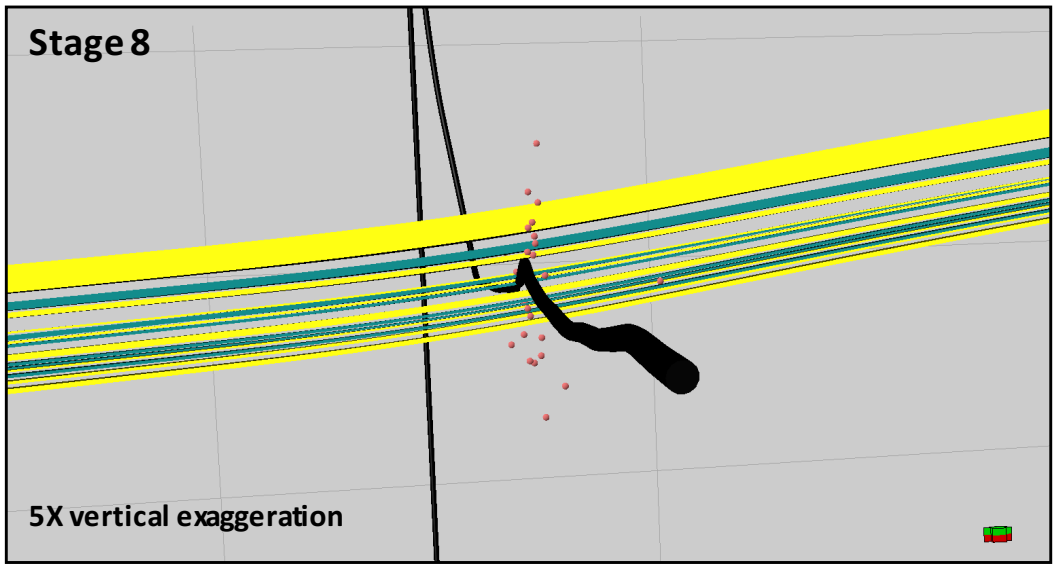

Figure 7.19: Stage 8 in the 3D view. When the stimulation occurs within the ductile zone, it is more likely that the fractures will grow close to the wellbore and energy will be absorbed by the ductile formation.

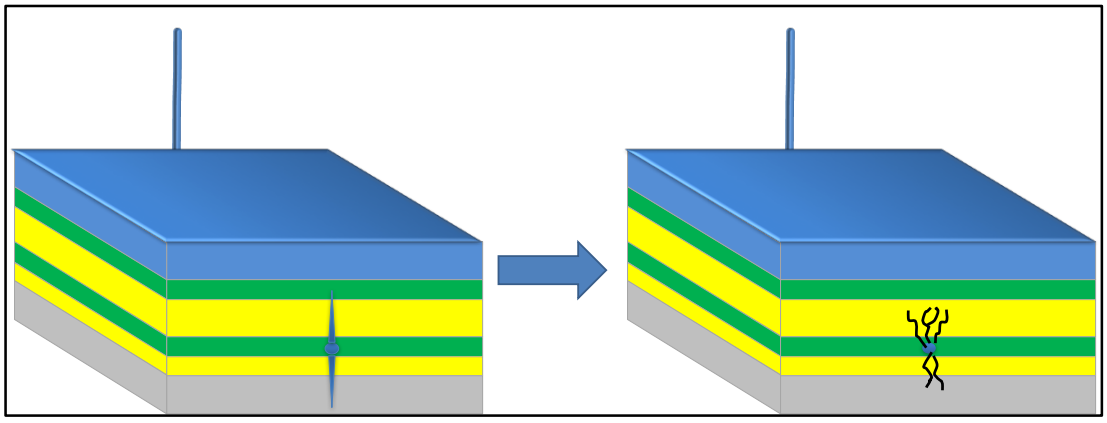

Figure 7.20: Hydraulic fracturing scenario 3. When the perforation shots are located within the ductile zone, the fracture will be constrained close to the wellbore and merely penetrate the formation. (blue section represents the Mississippian Lime, yellow section represents the brittle bed within the Woodford Shale, green section represents the ductile bed within the Woodford Shale, and gray section represents the Sylvan Shale formation beneath the Woodford Shale).

7.3 Fracture Efficiency

After analyzing all the distribution pattern of the stages, the overall evaluation of fracturing efficiency of each stage is possible. The factors considered for evaluation reference the methods proposed by Maxwell (2014) and optimized, which include: the

width of the microseimic event cloud, the width of the microseimic event cloud within the Woodford, the height, percentage of events within the target formation, accumulated magnitude within the target formation, and number of events within the target formation. After considering all the factors comprehensively, an overall efficiency evaluation is shown as Table 7.1. The Stage 1 is not included because it only has three events as a test shot. Stages 2, 6 and 7 are considered as high efficiency fracturing jobs. On the contrary, Stages 3, 5 and 11 are not considered as high efficiency fracturing jobs due to the low accumulated magnitude, low percentage of events within the Woodford and low width extension within the Woodford, respectively.

Stage	Width	Width in WDFD	Height	In WDFD	Accumulated Magnitude (in Woodford)	Number of Event (in Woodford)
2	1572	1365.84	914	49.8%	-537.44	160
3	1359.2	680	460	37.5%	-72.62	24
4	745	551	788	23.6%	-247.82	78
5	1785.5	1386	509	27.3%	-83.35	27
6	4345.99	2884	725	35.4%	-266.86	93
7	3064.31	2548	316	75.9%	-242.59	85
8	710	710	249	61.5%	-55.43	16
9	515	377	390	60%	-64.73	21
10	230	230	294	53.8%	-40.78	14
11	2022	126	481	35.7%	-251.71	65
12	158	106	325	27%	-26.86	9

Table 7.1: Fracturing job efficiency analysis of the H2 well. Stages 2, 6 and 7 are considered as high efficiency jobs due to the good performance on all the factors.

7.4 Stress Field Analysis

Due to the limitation of data, a general local stress direction can be estimated from the map view of the microseismic distribution and the H1 well image log. Larger scale stress field mapping requires additional microseismic data and image log data.

From the map view of the H2 well microseimic activities, most of the stages have the same strike direction of N80E, which represents the maximum horizontal stress direction (Maxwell, 2014). Stage 6 and 7 have an obvious asymmetric bi-wing structure; according to Maxwell (2014), this is mainly due to the pressure depletion caused by the Nemaha Faults. In Figure 7.21 there are two Nemaha Faults, the southern fault strikes north to south and has more impact on Stages 6 and 7. The northern fault strikes northeast to southwest and has impact on Stage 12 that contains more events on the east side. There are several events in Stage 12 that are away from the wellbore. This phenomenon is interpreted as the reaction of the subsurface fault or natural fractures along the fault strike direction. The maximum horizontal stress is also confirmed by the H1 well image log, the borehole breakouts are counted with orientation and the rose diagram shows the minimum horizontal stress direction of N10W, which is perpendicular to the maximum horizontal stress direction (Figure 7.22). For future well placement in the area, it is recommended to drill perpendicular to the maximum horizontal stress direction for the best well stimulation performance.

The conclusion from analyzing fracturing job efficiency is that for better stimulation performance, to locate the landing zone within the brittle zones. The brittle sections along the horizontal well bore can be identified by local sequence stratigraphic and brittle ductile couplets models. XRF profiles can also help identify the brittle zone

along the well bore. Considering the stage cloud width and height has bias for evaluation, the actions within the target formation should also be considered as important factors.

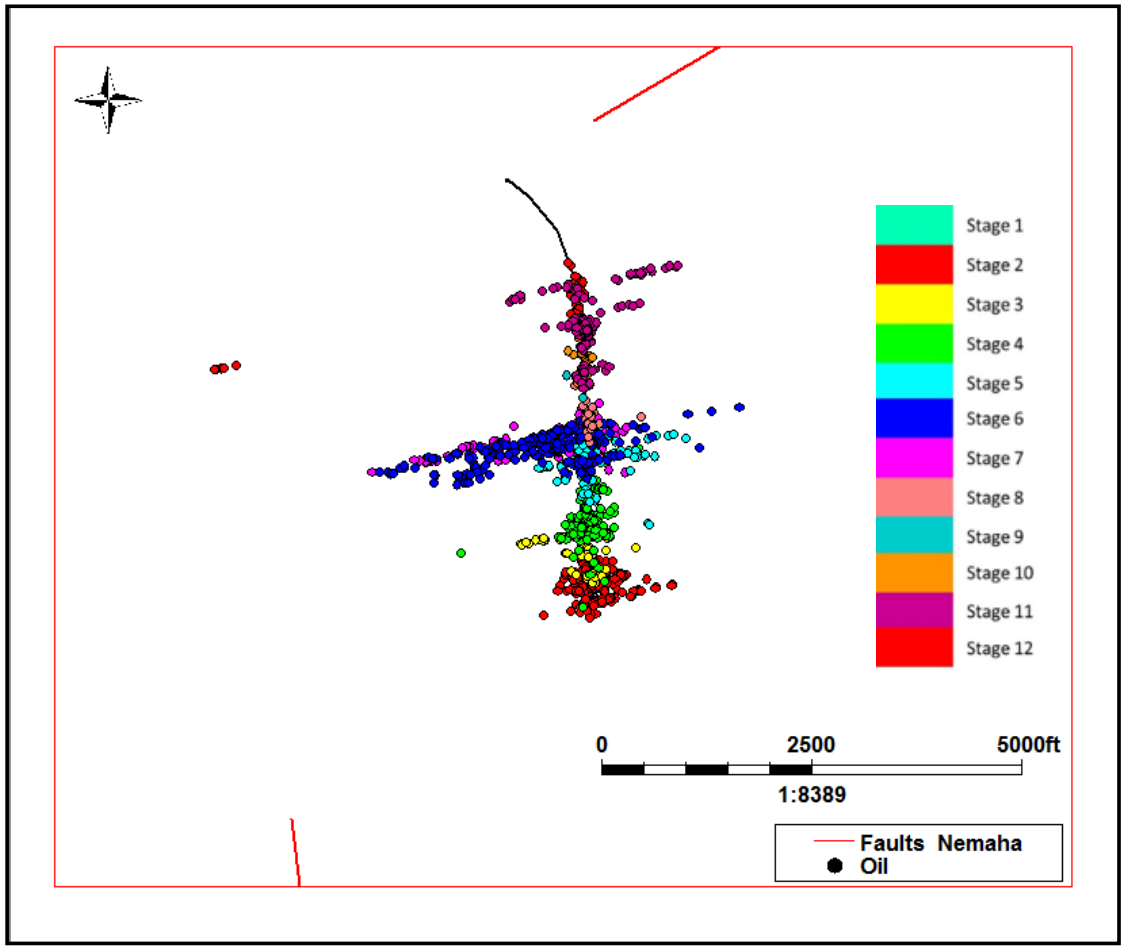

Figure 7.21: Map view of the H2 well and the microseismic events by the stages. The strike direction of the cloud reveals the maximum horizontal stress direction. Red lines at the southwest corner and north edge represent the Nemaha Fault.

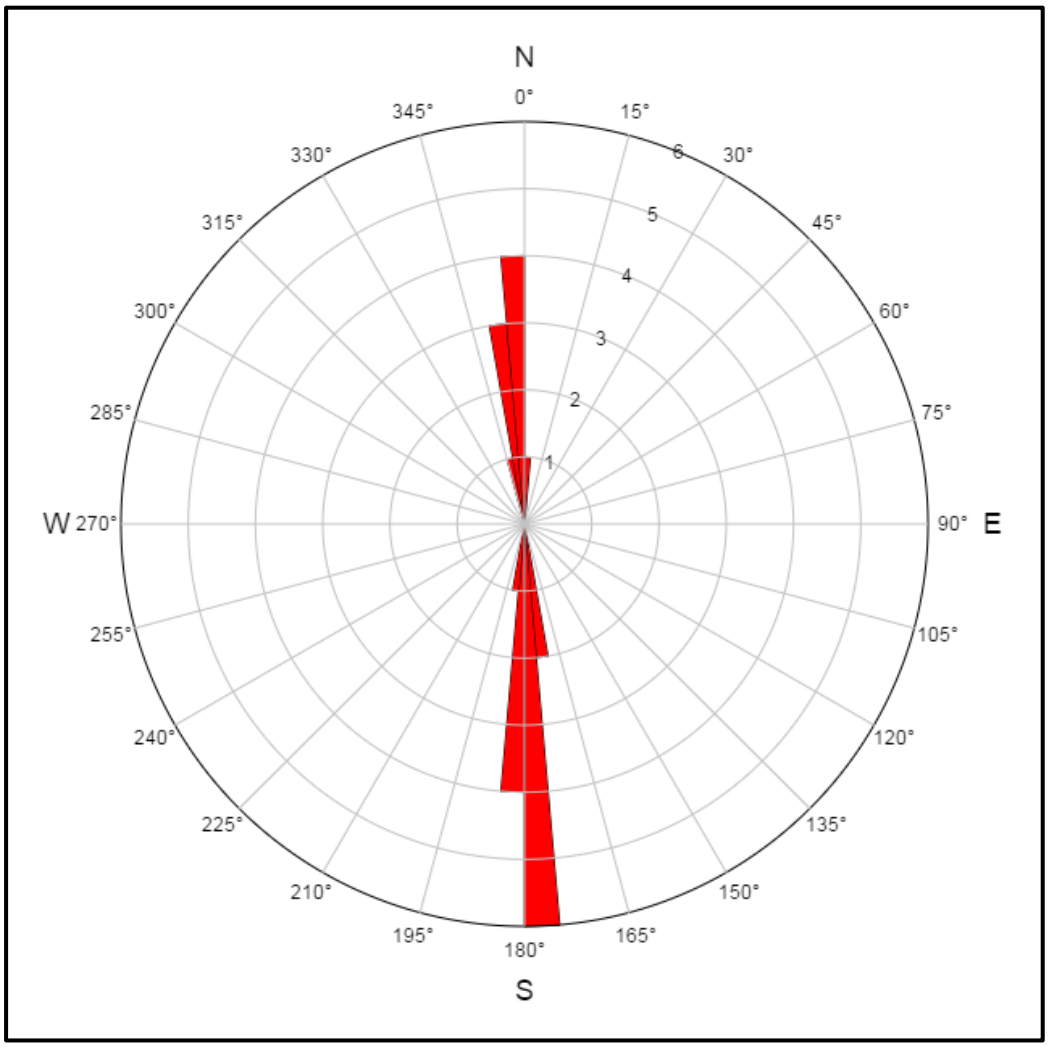

Figure 7.22: Rose diagram of the H1 well borehole breakout reveals the minimum horizontal stress direction.

Chapter 8: Discussion

For this research the datasets are mainly composed of well logs and cutting samples. Since the cutting sample is obtained as a mixture of certain depth interval, it has limitation to represent the lithology, and chemical composition at a specific depth, which causes some errors for the data analysis. This issue is especially obvious at the formation top section where the cuttings from the Woodford Shale are blended with the upper Mississippian Lime. Blending affects the Rock-Eval and XRD and XRF analysis results when too much overlying calcite is mixed with clay cuttings. If there is core available within or close to the study area in the future, it can be used as a calibration for both well logs and lab results to obtain a more confident interpretation. Even though the cuttings from the vertical well provide limited details of the formation, the cuttings from the horizontal wells contains fewer overlying cuttings because the well track is located within a smaller vertical range and has more data points in the horizontal direction. The horizontal well cuttings can help characterize the horizontal heterogeneity introduced by sediments within the reservoir. In order to get a bigger vertical range of data, more than one horizontal well cuttings in the area needs to be taken for analysis.

Chapter 9: Results and Conclusions

Based on all the interpretations, analysis and research methods discussed in the former chapters, various aspects of the Woodford Shale in the study area are characterized and now understood.

In sequence stratigraphy terms, the Woodford was deposited during two second order transgression and regression cycle. Based on the well logs it can be further subdivided into seven third order parasequences that represent smaller scale sea level fluctuations. The thickness of the Woodford Shale is inversely related with that of the Sylvan Shale, especially in the central part of the study area. The Woodford Shale is gently dipping towards the southwest into the Anadarko Basin. For each parasequence, the thickness distribution varies and is not as consistent with the overall formation thickness distribution. Thus for better well design results, the thickness variability and characteristics of each parasequence need to be considered before placing the well.

From the drill cutting thin sections and XRD results, the general mineralogy of the formation is characterized. The Woodford Shale has a high clay and moderate quartz content in the middle-lower section (from the H2 well XRD analysis result). There are mainly five types of Woodford cuttings that represent different depositional environments and water conditions: (1) quartz rich massive mudstone, (2) quartz rich laminae mudstone, (3) black massive organic-rich mudstone, (4) dolomitic mudstone and (5) radiolarian-rich cherty mudstone. The percentage of each type of cuttings varies by depth and also corresponds with the gamma ray reading which is affected by potassium in clays.

Chemostratigraphic analysis characterized the inorganic chemical variability of the Woodford Shale cuttings and the datasets are grouped as chemofacies. There are 12 chemofacies defined for the H2 well cuttings that can be correlated within a sequence stratigraphic framework. The chemofacies distribution can help characterize the horizontal heterogeneity within the reservoir and was used for the reservoir modeling process. The XRF derived geochemical data can also be correlated with the XRD derived mineral data for mineral percentage estimation and brittleness calculation. The method of mineral percentage regression and brittleness calculation can be used for the other wells cutting and core XRF data.

From the organic geochemistry analysis results, the Woodford Shale in the study area has very good source rock potential indicated by the high S2 peak and high TOC percentage. The Woodford Shale is in the oil window which benefits the future production and exploration activity. The TOC value is highly correlated with Mo and V from the XRF dataset. Since Mo and V are proxies of a paleo-anoxic environment that favors preserving organic matter from oxidization and degradation. Thus for organic-rich shale, Mo and V can be used as a screening tool to pick out the organic-rich section either from a vertical or horizontal profile.

The microseismic interpretation of the H2 well reveals the relationship between sequence stratigraphic framework and microseismic distribution and how the sequence stratigraphy can affect the hydraulic fracturing job efficiency, the highstand system tract or brittle zone is more prone to have higher fracture efficiency since the fracture is more likely to stay within the formation and fractures grow horizontally along the formation bedding.

From all the above aspects, this research provides a comprehensive characterization of the Woodford Shale in the study area based upon well logs and cuttings. Future study should include core characterization for data calibration, lithofacies description, and higher resolution XRF profile interpretation. The production data can also be interpreted to compare the differences on both sides of the Nemaha Uplift.

References

Ali, E. E., 2015, Integrated characterization of the Woodford Shale in southwest Cherokee Platform, Oklahoma, Master's thesis, University of Oklahoma, Norman, Oklahoma, 104 p.

Algeo, T. J., and H. Rowe, 2012, Paleoceanographic applications of trace-metal concentration data: Chemical Geology, v. 324-325, p. 6–18.

Al-Shaieb, Z., J. Puckette, and P. Blubaugh, 2000, The Hunton Group: Sequence Stratigraphy, Facies, Dolomitization, and Karstification, in C. J. Mankin ed., Oklahoma Geological Survey Special Publication 2000-2: Hunton Play in Oklahoma (Including Northeast texas Panhandle): Norman, Oklahoma Geological Survey, p. 39-50.

Althoff, C. D., 2012, Characterization of Depositional Megacycles in the Woodford Through of Central Oklahoma, Master's thesis, University of Oklahoma, Norman, Oklahoma, 107 p.

Amorocho, J. D., 2012, Sequence stratigraphy and seismic interpretation of the Upper Devonian - Lower Mississippian Woodford Shale in the Cherokee Platform : a characterization approach for unconventional resources, Master's thesis, University of Oklahoma, Norman, Oklahoma, 109 p.

Amsden, T. W., 1975, Hunton Group (Late ordovician, Silurian, and Early Devonian) in the Anadarko basin of Oklahoma, Oklahoma Geological Survey Bulltin 121: Norman, Oklahoma Geological Survey, 214 p.

Amsden, T. W., 1980, Hunton Group (Late Ordovician, Silurian and Early Devonian) in Arkoma basin of Oklahoma, Oklahoma Geological Survey Bulletin 129: Norman, Oklahoma Geological Survey, 136 p.

Andrews, R., 2014, unpublished Formation Evaluation 2014 course document.

Badra, H., 2011, Field characterization and analog modeling of natural fractures in the Woodford Shale, southeast Oklahoma, Master's thesis, University of Oklahoma, Norman, Oklahoma, 78 p.

Banner, J. L., 1995, Application of the trace element and isotope geochemistry of strontium to studies of carbonate diagenesis: Sedimentology, v. 42 (5), p. 805-824.

Barker, C. E., and M. J. Pawlewicz, 1986, The correlation of vitrinite reflectance with maximum temperature in humic organic matter: In Stehena, G., and L. Buntebarth, ed., Paleogeothermics, New York, Springer Berlin Heidelberg, p. 79-93.

Baskin, D. K., 1997, Atomic H/C ratio of kerogen as an es- timate of thermal maturity and organic matter conver- sion: AAPG Bulletin, v. 81, p. 1437-1450.

Beebe, B.W, 1959, Characteristics Of Mississippian Production In The Northwestern Anadarko Basin: Tulsa Geological Society Digest 27, p. 190-205.

Behar, F., V. Beaumont, and H. L. D. B. Penteado, 2001, Rock-Eval 6 Technology: Performances and Developments: Oil & Gas Science and Technology - Rev. IFP Oil & Gas Science and Technology, v. 56, no. 2, p. 111–134.

Bernal, A., 2013, Geological characterization of the Woodford Shale, McAlister Cemetery Quarry, Criner Hills, Ardmore Basin, Oklahoma, Master's thesis, University of Oklahoma, Norman, Oklahoma, 141 p.

Blakey, R. C., 2012, Paleogeography and Geologic Evolution of North America, http://cpgeosystems.com/nam.html.

Bontempi, C. P., 2015, High resolution stratigraphy of thin bedded shales/radiolarites, Woodford Shale, Arbuckle Wilderness area, Murray County, Oklahoma: a new correlation tool, Master's thesis, University of Oklahoma, Norman, Oklahoma, 81 p.

Brady, J. B., R. M. Newton, and S. J. Boardman, 1995, New Uses for Powder X-ray Diffraction Experiments in the Undergraduate Curriculum: Geol. Education, v. 43, p. 466-470.

Butt, A. S., 2012, Shale Characterization Using X-Ray Diffractionn, Master's thesis, Universitas Dalhousie, Halifax, Nova Scotia, 55 p.

Cardona, L. F., 2014, Integrated characterization of the Woodford Shale in the southern Cherokee Platform, Oklahoma, Master's thesis, University of Oklahoma, Norman, Oklahoma, 98 p.

Chain, A. R., 2012, Stratigraphy and composition of the Woodford Shale in depositionally updip and downdip wells, Anadarko Basin, Oklahoma, Master' thesis, University of Oklahoma, Norman, Oklahoma, 118 p.

Chalmers, G. R., R. M. Bustin, and I. M. Power, 2012, Characterization of gas shale pore systems by porosimetry, pycnometry, surface area, and field emission scanning electron microscopy/transmission electron microscopy image analyses: Examples from the Barnett, Woodford, Haynesville, Marcellus, and Doig units: AAPG Bulletin, v. 96, no. 6, p. 1099–1119.

Clair, J. R., 1948, Preliminary Notes on Lithologic Criteria for Identification and Subdivision of the Mississippian Rocks in Western Kansas: Kansas Geological Society, 14 p.

Comer, J. B., 1991, Stratigraohic Analysis of the Uper Devonian Woodford Formation, Permian Basin, West Texas and Southern New Mexico: Report of Investigation, University of Texas at Austin, Austin Texas, 61 p.

Comer, J. B., 1992, Organic Geochemistry and Paleogeography of Upper Devonian Formation in Oklahoma and Northern Arkansas: Oklahoma Geological Survey Circular 93, p. 70-93.

Dembicki, H., B. Horsfield, and T. T. Y. Ho., 1983, Source rock evaluation by pyrolysis-gas chromatography: AAPG Bulletin, v. 67, p. 1094-1103.

Dembicki, H., 2009, Three common source rock evaluation errors made by geologists during prospect or play appraisals: AAPG Bulletin, v. 93, no. 3, p. 341-356.

Espitalié, J., 1986, Use of Tmax as a maturation index for different types of organic matter. Comparison with vitrinite reflectance, in J. Burrus, ed., Thermal modelling in sedimentary basins: Paris, Editions Technip, p. 475-496.

Espitalié, J., and M. L. Bordenave, 1992, Tools for source-rock routine analyses: Rock-Eval pyrolysis, in M. L. Bordenave, ed., Applied Petroleum Geochemistry: Paris, Editions Technip, p. 237-261.

Espitalié, J., G. Deroo, and F. Marquis, 1985, La pyrolyse Rock-Eval et ses applications. Deuxième partie: Revue de l'Institut français du Pétrole, v. 40, no. 6, p. 755-784.

Espitalie, J., J. L. Laporte, M. Madec, F. Marquis, P. LePlat, J. Paulet, and A. Boutefeu, 1977, Methode rapide de caracterisation des roches meres de leur potentiel petrolier et de leur degre d'evolution: Revue l'Institute Franc ¸ais du Pe´trole, v. 32, p. 23-42.

Espitalie, J., M. Madec, and B. Tissot, 1980, Role of mineral matrix in kerogen pyrolysis: Influence on petroleum gen- eration and migration: AAPG Bulletin, v. 64, p. 59-66.

Finlow-Bates, Y., and E. F. Stumpfl, 1981, The behaviour of so-called immobile elements in hydrothermally altered rocks associated with volcanogenic submarine-exhalative ore deposits: Mineralium Deposita, v. 16, no. 2, p. 319-328.

Fritz, R. D., and L. Gerken, 2001, Exploration potential of the lower Mississippian Sycamore Limestone, in K. S. Johnson, ed., Oklahoma Geological Survey Circular 105: Sirlurian, Devonian, and Mississippian geology and petroleum in the southern Midcontinent, 1999 symposium: Norman, Oklahoma Geological Survey, p. 174.

Giraud, A., 1970, Application of pyrolysis and gas chroma- tography to geochemical characterization of kerogen in sedimentary rocks: AAPG Bulletin, v. 54, p. 439-451.

Hanawalt, J. D., 1986, Manual Search/Match Methods for Powder Diffraction in 1986: Powder Diffraction, v. 1, no. 1, p. 7-13.

Harris, W., and G. N. White, 2008, X-ray diffraction techniques for soil mineral identification, in A. L. Ulery, and L. R. Dress, ed., Methods of soil analysis Part 5 – Mineralogical Methods: Madison, Soil Science Society of America, Inc., p. 81-115.

Hasbrook, N. T., 2015, Micro porosity of the Woodford Shale in Canadian and Washington Counties, Oklahoma, Master's thesis, University of Oklahoma, Norman, Oklahoma, 106 p.

Hasbrook, S. E., 2015, Geologic characterization of the Woodford Shale across the Arbuckle Uplift counties, south central Oklahoma, Master's thesis, University of Oklahoma, Norman, Oklahoma, 103 p.

Hester, T., H. Sahl, and J. Schnoker, 1988, Cross sections based on gamma-ray density, and resistivity log showing the stratigraphic unites of the Woodford Shale in Anadarko basin, Oklahoma: United States Geological Survey, Miscellaneous Field Studies Map 2054, 2 sheets.

Higley, D. K., 2014, Petroleum systems and assessment of undiscovered oil and gas in the Anadarko Basin Province, Colorado, Kansas, Oklahoma, and Texas-USGS Province 58 (NO. 69-EE), http://pubs.usgs.gov/dds/dds-069/dds-069-ee/.

Hunt, J. M., 1979, Petroleum geochemistry and geology: San Francisco, W. H. Freeman, 743 p.

Infante, L. E., 2015. Seismically-determined distribution of total organic carbon (TOC) in the Woodford Shale through integrated reservoir characterization, Payne County, Oklahoma, Master's thesis, University of Oklahoma, Norman, Oklahoma, 79 p.

Infante, L. E., F. Cardona, and R. Slatt, 2016, Seismic Analysis of Total Organic Carbon (TOC) Distribution in the Woodford Shale, Oklahoma: AAPG ACE Annual Conference: Calgary, AAPG.

Jarvie, D. M., 1991, Total Organic Carbon (TOC) Analysis: Chapter 11: Geochemical Methods And Exploration, in R. K. Merrill, ed., Source and Migration Processes and Evaluation Techniques: AAPG Special Volumes, p. 113-118.

Jin, X., S. N. Shah, J.-C. Roegiers, and B. Zhang, 2014, Fracability Evaluation in Shale Reservoirs - An Integrated Petrophysics and Geomechanics Approach: SPE Hydraulic Fracturing Technology Conference: Woodlands, SPE.

Johnson, K. S., and B. J. Cardott, 1992, Geologic framework and hydrocarbon source rocks of Oklahoma, in K. S. Johnson and B. Cardott, ed., Oklahoma Geological

Survey Circular 93: Source rocks in the southern Midcontinent, 1990 symposium: Norman, Oklahoma Geological Survey, p. 21-37.

Katz, B. J., 1983, Limitations of "Rock-Eval" pyrolysis for typing organic matter: Org. Geochem, v. 4, p. 195-199.

Kaufman, L., and P. J. Rousseeuw, Finding Groups in Data - An Introduction to Cluster Analysis: Hoboken, John Wiley & Sons, 349 p.

Kilian, B. J., 2012, Sequence stratigraphy of the Woodford Shale, Anadarko Basin, Oklahoma: implications on regional Woodford target correlation, Master's thesis, University of Oklahoma, Norman, Oklahoma, 102 p.

Kirkland, D. W., R. E. Denison, D. E. Summers, and J. R. Gorm, 1992, Geology and organic geochemistry of the Woodford Shale in the Criner Hills and western Arbuckle Mountains, in K. S. Johnson and B. Cardott, ed., Oklahoma Geological Survey Circular 93: Source rocks in the southern Midcontinent, 1990 symposium: Norman, Oklahoma Geological Survey, p. 38-69.

Knoll, A.H., and E. S. Barghoorn, 1974, Ambient pyrite in precambrian chert: new evidence and a theory: Proc Natl Acad Sci U S A, v. 71, no. 6, p. 2329-2331.

Krumme, G.W., 2000, Geologic Setting Provides Keys to Locating the Elusive Devonian Misener Sandstone in Central Northern Oklahoma, in K. S. Johnson, ed., Oklahoma Geological Survey Circular 105: Sirlurian, Devonian and Mississippian Geology and Petroleum in the Southern Midcontinent, 1999 Symposium: Norman, Oklahoma Geological Survey, p. 47-56.

Kuykendall, M. D., and R. D. Fritz, 1993, Misener Sandstone: Distribution and Relationship to Late/Post-Hunton Unconformities, North Shelf, Anadarko Basin, in K. S. Johnson, ed., Oklahoma Geological Survey Special Publication 93-4: Hunton Group Core Workshop and Field Trip: Norman, Oklahoma Geological Survey, p. 117-134.

Kuykendall, M. D., and R. D. Fritz, 2001, Misener sandstone of Oklahoma Phase I. Online Report #10018, AAPG Search and Discovery, http://www.searchanddiscovery.com/documents/misener/index.htm.

Lafargue, E., F. Marquis, and D. Pillot, 1998, Rock-Eval 6 applications in hydrocarbon exploration, production, and soil contamination studies: Revue de l'Institut Français du Pétrole, v. 53, p. 421-437.

Langford, F. F., and M. M. Blanc-Valleron, 1990, Interpreting rock-eval pyrolysis data using graphs of pyrolysable hydrocarbons vs. total organic carbon: AAPG Bulletin, v. 74, p. 799–804.

Larter, S. R., and A. G. Douglas, 1979, A pyrolysis-gas chro- matographic method for kerogen typing, in A. G. Douglas and J. R. Maxwell, ed., Advances in organic geochemistry: New York, Pergamon Press, p. 579-584.

Lewan, M. D., 1983, Effects of thermal maturation on stable organic carbon isotopes as determined by hydrous pyrolysis of Woodford Shale: Geochemica et Cosmochimica Acta, v. 47, p. 1471-1479.

Lior, R., and O. Maimon, 2005, Clustering methods, in R. Lior, and O. Maimon, ed., Data mining and knowledge discovery handbook: New York, Springer, p. 321-352.

Maxwell, S., 2014, Microseismic Imaging of Hydraulic Fracturing: Tulsa, Society of Exploration Geophysics, 197 p.

McCullough, B. J, 2014, Sequence-stratigraphic framework and characterization of the Woodford Shale on the southern Cherokee Platform of central Oklahoma, Master' thesis, University of Oklahoma, Norman, Oklahoma, 212 p.

McHargue, T. R., and R. C. Price, 1982, Dolomite from Clay in Argillaceous or Shale-Associated Marine Carbonates: Journal of Sedimentary Research, v. 52, no. 3, p. 873-886.

Molinares, C. E., 2013, Stratigraphy and palynomorphs composition of the Woodford Shale in the Wyche Farm Shale Pit, Pontotoc County, Oklahoma, Master's thesis, University of Oklahoma, Norman, Oklahoma, 90 p.

Newell, K. D., J. H. Doveton, and M. W. Lambert, 2000, Facies and Petrophysical Characteristics of the Chattanooga Shale and Misener Sandstone in Central Kansas, in K. S. Johnson, ed., Oklahoma Geological Survey Circular 105: Sirlurian, Devonian and Mississippian Geology and Petroleum in the Southern Midcontinent, 1999 Symposium: Norman, Oklahoma Geological Survey, p. 57-70.

Noble, P., and P. Renne, 1990, Paleoenvironmental and biostratigraphic significance of siliceous microfossils of the Permo-Triassic Redding Section, Eastern Klamath Mountains, California: Marine Micropaleontology, v.14, p. 379-391.

Northcutt, R. A., K. S. Johnson, and G. C. Hinshaw, 1999, Geology and Petroleum Reservoir in Sirlurian, Devonian and Mississippian Rocks in Oklahoma, in K. S. Johnson, ed., Oklahoma Geological Survey Circular 105: Sirlurian, Devonian and Mississippian Geology and Petroleum in the Southern Midcontinent, 1999 Symposium: Norman, Oklahoma Geological Survey, p. 1-16.

Northcutt, R.A., and J. A. Campbell, 1995, Geologic Province of Oklahoma: Oklahoma Geological Survey, Norman.

Okalhoma Geological Survey, 2016, 2016 Woodford Shale Completions Map by Year, 2004-2015: Oklahoma Geological Survey. http://ou.edu/content/ogs/research/energy/oil-gas.html.

O'Brien, N. R., and R. M. Slatt, 1990, Argillaceous Rock Atlas: New York, Springer-Verlag, 141 p.

Over, J. D., 2002, The Frasnian/Famennian boundary in central and eastern United States: Palaeogeography, Palaeoclimatology, Palaeoecology, v. 181, no. 1, p. 153-169.

Pearce, T. J., B. M. Besly, D. S. Wray, and D. K. Wright, 1999, Chemostratigraphy: a method to improve interwell correlation in barren sequences – a case study using onshore Duckmantian/Stephanian sequences (West Midlands, U.K.): Sedimentary Geology, v. 124, p. 197-220.

Pearce, T. J., and I. Jarvis, 1992, Applications of geochemical data to modelling sediment dispersal patterns in distal turbidites: Late Quaternary of the Madeira Abyssal Plain: Journal of Sedimentary Petrology, v. 62, no. 6, p. 1112-1129.

Perry, E., and J. Hower, 1970, Burial diagenesis in Gulf Coast pelitic sediments, Clays and Clay Mineralogy, v. 18, p. 165-177.

Peters, K. E., 1986, Guidelines for evaluating petroleum source rock using programmed pyrolysis: AAPG Bulletin, v. 70, p. 318-329.

Phillips, N., and G. Dong, 1994, Chert-Plus-Pyrite Pebbles in the Witwatersrand Goldfields: International Geology Review, v. 36, no. 1, p. 65-71.

Portas, R. M., 2009, Characterization and origin of fracture patterns in the Woodford Shale in southeastern Oklahoma for application to exploration and development, Master' s thesis, University of Oklahoma, Norman, Oklahoma, 110 p.

Rickman, R., M. J. Mullen, J. E. Petre, W. V. Grieser, and D. Kundert, 2008, A practical use of shale petrophysics for stimulation design optimization: All shale plays are not clones of the Barnett Shale: SPE Annual Technical Conference and Exhibition, Denver, Society of Petroleum Engineers.

Rowe, H., S. Rupple, S. Rimmer, and R Loucks, 2009, Core-based chemostratigraphy of the Barnett Shale, Permian Basin, Texas: Gulf Coast Association of Geological Societies Transactions, v. 59, p. 675-686.

Rowe, H., R. Loucks, amd C. Kerans, 2015, Core Chemostratigraphy and Elemental Geochemistry along a Dip- Section, Pearsall Formation, Lower Cretaceous, Central to South TX: Unconventional Resources Technology Conference (URTeC), San Antonio, UrTec.

Seyfarth, A., B. Kaiser, and, L. Darke, 2014, FIRST Newsletter.

https://www.bruker.com/fileadmin/user_upload/8-PDF-Docs/X-rayDiffraction_ElementalAnalysis/HH-XRF/Misc/HHXRF_Mudrock-Shale_Chemostratigraphy.pdf.

Slatt, R. M., and N. R. O'Brien, 2011, Pore types in the Barnett and Woodford gas shales: Contribution to understanding gas storage and migration pathways in finegrained rocks: AAPG Bulletin, v. 95, no. 12, p. 2017-2030.

Slatt, R. M., and Y. Abousleiman, 2011, Merging sequence stratigraphy and geomechanics for unconventional gas shales: The Leading Edge, v. 13, no. 3, p. 274-282.

Slatt, R. M., P. R. Philp, Y. Abousleiman, P. Singh, R. Perez, R. Portas, K. J. Marfurt, S. Madrid-Arroyo, N. O'Brien, E. V. Eslinger, and E. T. Baruch, 2012, Pore-to-regional-scale integrated characterization workflow for unconventional gas shales, in J. A. Breyer, ed., Shale reservoirs—Giant resources for the 21st century: AAPG Memoir 97, p. 127-150.

Slatt, R. M., 2013, Sequence Stratigraphy of the Woodford Shale and Application to Drilling and Production, oral presentation given at AAPG the Woodford Shale Forum, Oklahoma City, Oklahoma, in April, 11, 2013. AAPG Search and Discovery Article #50792.

Taff, J. A., 1902, Atoka folio, Indian Territory: U.S. Geological Survey, Geologic Atlas of the United States Folio GF-79, 4 sheets.

Tissot, B. P., D. Durand, J. Espitalie, and A. Combaz, 1974, Influence of Nature and Diagenesis of Organic Matter in Formaiton of Petroleum: AAPG, v. 58, no. 3, p. 499-506.

Tissot, B. P., and D. H. Welte, 1984, Petroleum Formation and Occurrence: New York, Springer-Verlag, 700 p.

Treanton, J. A., 2014, Outcrop-derived chemostratigraphy of the Woodford Shale, Murray County, Oklahom, Master's thesis, University of Oklahoma, Norman ,Oklahoma , 83 p.

Tribovillard, N., T. J. Algeo, T. Lyons, and A. Riboulleau, 2006, Trace metals as paleoredox and paleoproductivity proxies: An update: Chemical geology, v. 232, no. 1, p. 12-32.

Turner, B. W., C. E. Molinares, R. M. Slatt, 2015, Chemostratigraphic, palynostratigraphic, and sequence stratigraphic analysis of the Woodford Shale, Wyche Farm Quarry, Pontotoc County, Oklahoma, Interpretation, v. 3, no. 1, p. 1-9.

Turner, B., J. Tréanton, and R. M. Slatt, 2015, The Use of Chemostratigraphy to Refine Ambiguous Sequence Stratigraphic Correlations in Marine Shales: An Example

From the Woodford Shale, Oklahoma: Proceedings of the 3rd Unconventional Resources Technology Conference.

Turner, B. J., 2016, Utilization Of Chemostratigraphic Proxies For Generating And Refining Sequence Stratigraphic Frameworks In Mudrocks And Shales, Ph.D's thesis, University of Oklahoma, Norman, Oklahoma, 135 p.

Ward, J. H., 1963, Hierarchical Grouping to Optimize an Objective Function: Journal of the American Statistical Association, v. 58, no. 301, p. 236-244.

Wang, F. P., and J. F. W. Gale, 2009, Screening criteria for shale-gas systems: Gulf Coast Association of Geological, v. 59, p. 779-793.